

The Marine Geomorphology of American Samoa: Shapes and Distributions of
Deep Sea Volcanics

by
Jed T. Roberts

A THESIS

submitted to

Oregon State University

in partial fulfillment of
the requirements for the
degree of

Master of Science

Presented November 20, 2007
Commencement June 2008

AN ABSTRACT OF THE THESIS OF

Jed T. Roberts for the degree of Master of Science in Geography presented on November 20, 2007.

Title: The Marine Geomorphology of American Samoa: Shapes and Distributions of Deep Sea Volcanics

Abstract approved:

Dawn J. Wright

The geologic processes at work in American Samoa have long been a point of scientific debate. Of its numerous volcanic formations, few breach sea level, leaving an enormous proportion of their mass unavailable to traditional observation. This study aims to describe the deep sea geomorphology of American Samoa through compilation, quantitative analysis, and qualitative interpretation of multibeam bathymetry datasets in an effort to contribute a new perspective on volcanic origins. Compilation of multibeam bathymetry datasets collected by various primary sources over the last two and half decades is accomplished using the multibeam processing software package MB-System by Caress and Chayes (1996). The high-resolution product is then employed to measure shape parameters of small seamounts (height < 1,000 m). Methods of quantitative analysis established by Jordan et al. (1983) and Smith (1988) are then used to assess the geomorphologic implications of shape parameter relationships. These relationships suggest that morphologies of small seamounts in American Samoa are typical of Pacific seamounts, though infrequent departures show forms indicative of mid-ocean ridge type magmas. A distribution analysis of small seamounts follows, calculating areal density with the exponential distribution model conceived by Jordan et al. (1983) and modified by Smith and Jordan (1988). Distribution analysis yields a predicted density of 2.8 seamounts per 1,000 km² and a characteristic height of 139 m, both within expectations for seamounts in the Pacific. Finally, a qualitative interpretation of the entire study area is undertaken that includes mapping of major volcanic features, morphologic descriptions of large seamounts, and considerations of age-progression based on arrangements of volcanic lineaments.

©Copyright by Jed T. Roberts
November 20, 2007
All Rights Reserved

Master of Science thesis of Jed T. Roberts presented on November 20, 2007.
APPROVED:

Major Professor, representing Geography

Chair of the Department of Geosciences

Dean of the Graduate School

I understand that my thesis will become part of the permanent collection of Oregon State University libraries. My signature below authorizes release of my thesis to any reader upon request.

Jed T. Roberts, Author

ACKNOWLEDGMENTS

First and foremost, I express my deepest appreciation and respect for Dawn Wright, who made this work possible through her continual support and patience during my time at Oregon State University. It has been a distinct privilege to contribute as a member of the Davey Jones Locker Laboratory, an experience not soon forgotten. I would like to thank Mark Meyers, our adept lab technician, whose wisdom saved more than a few keystrokes and headaches. I am grateful for the expertise shared by Anthony Koppers with regard to his work in Samoa, for his enormous contribution toward the final compilation of bathymetry, and of course, his willingness to participate as a member of my graduate committee. In this respect, I also thank Randy Keller and Gary Klinkhammer for their membership on my graduate committee, and Emily Lundblad for her help in tracking down data.

My academic success is in no small part attributed to my colleagues and friends in the Geosciences Department and throughout Oregon State University. This includes, but is not limited to, B. J. Walker, Nate Eidem, Aaron Arthur, Morgan Salisbury, Dave Trench, Mimi Dailey, Melissa Brazeale, Nate Shaub, Wiley Thompson, Sarah Mikulak, Celeste Barthel, Kyle Hogrefe, Eleanor Hodak, Anna Pakenham, Cheney Vidrine, Tory Fitchett, Jason Kenworthy, Steven Highland, Dave Bradford, Tim Perry, Quin Ourada, Chris Somes, Kristen Splinter, Lisa Andes, Susie Genualdi, Katy Loynes, Amanda Benton, Olivia Odom, Amy McNally, Mac Barr, Katie Moriarty, and Michelle Kinzel.

Finally, I would like to thank my mother, Toni, father, Tucker, and brother, Seth for their encouragement not only during my Master's program, but throughout life. They are the best family a boy could ask for!

CONTRIBUTION OF AUTHORS

Dawn Wright is in large part responsible for the inception of this study, providing valuable data, contacts, and advice. Anthony Koppers shared his knowledge of Samoan geochronology and collection of multibeam bathymetry, both of which have significantly improved the quality of this study. Dave Naar of the University of South Florida also provided multibeam bathymetry. The remaining multibeam bathymetry used in this study was collected by scientists at the Scripps Institution of Oceanography, Oregon State University, Woods Hole Oceanographic Institution, the University of Rhode Island, the NOAA Pacific Islands Fisheries Science Center, the University of Hawaii Marine Center, and the Hawaii Undersea Research Laboratory.

TABLE OF CONTENTS

	<u>Page</u>
1. Introduction	1
1.1 Overview	1
1.2 Significance	2
1.3 Study Area	3
2. Geologic Setting	4
2.1 Historical Observations	4
2.2 Early Geochemistry	7
2.3 Tectonism and Lithospheric Flexure	8
2.4 Radiometric Dating	11
2.5 Advanced Geochemistry	12
2.6 Mantle Plumes	14
2.7 Mantle Plumes vs. Lithospheric Flexure	17
2.8 Rose Atoll	18
3. Bathymetry and Compilation	19
3.1 Early Bathymetry	19
3.2 Multibeam Bathymetry	19
3.3 Early Applications in Marine Geomorphology	23
3.4 Datasets	24
3.5 Multibeam Compilation	26
3.6 Cartography	27
4. Seamount Morphology	27
4.1 Seamount Formation and Anatomy	27
4.2 Quantitative Studies	29
4.3 Seamount Identification and Shape Parameters	30
4.4 Observed Relationships	33
5. Seamount Distribution	39
5.1 Geologic Controls on Distribution	39
5.2 The Exponential Distribution Model	40
5.3 Application of Model and Results	41

TABLE OF CONTENTS (Continued)

	<u>Page</u>
5.4 Discussion	42
6. Geomorphologic Interpretation	46
6.1 Tutuila	46
6.2 Papatua	47
6.3 Muli	47
6.4 Tulaga and Malumalu	48
6.5 The Manu'a Islands	48
6.6 Vailulu'u	49
6.7 Tama'i, Soso, and Malulu	49
6.8 Small Seamounts	50
6.9 <i>En Echelon</i> Lineaments and Age Progressions	51
7. Conclusion	51
7.1 Current Geomorphology	51
7.2 Future Work	52
8. References	59
9. Appendix A: Multibeam Compilation Technical Notes	67
9.1 The MB-System Datalist	67
9.2 The MB-System "mbinfo" Command	68
9.3 The MB-System "mbgrid" Command	69
9.4 Visualization Options	70
10. Appendix B: Seamount Shape Statistics Expanded	72
10.1 Slope Surface and Profiles	72
10.2 Secondary Shape Statistics Equations	72
10.3 Shape Statistics by Seamount	72
11. Appendix C: Seamount Distribution Analysis Expanded	75
11.1 Calculating Area	75
11.2 Calculating Characteristic Height	77

TABLE OF CONTENTS (Continued)

	<u>Page</u>
11.3 Calculating Seamount Distribution	78

LIST OF FIGURES

<u>Figure</u>	<u>Page</u>
1. Global View of Study Area	4
2. Political Map of Study Area	5
3. Volcanic Centers of Tutuila	6
4. Cutaway Diagram of Samoan Region	9
5. Illustration of Samoan Hotspot	15
6. Tomographic Image of Samoan Hotspot	16
7. Plot of $^{206}\text{Pb}/^{204}\text{Pb}$ Ratio Values	17
8. Bathymetric Map of Samoa Region	20
9. Illustration of Multibeam System in Use	21
10. Accuracy Plot for Simrad EM120	22
11. Diagram of Typical Seamount Anatomy	29
12. Schematic of Radiating Dike Injections	30
13. Illustrations of Seamount Shape Estimation	31
14. Conical Frustum	32
15. Fledermaus Profiling Tool	33
16. Shape Parameter Relationship: Basal Area vs. Height	34
17. Shape Parameter Relationship: Flatness vs. Height	35
18. Shape Parameter Relationship: Slope vs. Height	36
19. Shape Parameter Relationship: Volume vs. Height	37

LIST OF FIGURES (Continued)

<u>Figure</u>	<u>Page</u>
20. Shape Parameter Relationship: Flatness vs. Basal Depth	38
21. Rose Diagram of Major Basal Axis Azimuth	39
22. Bins and Cumulative Percentage Plot	42
23. Semi-Log Plot of Exponential Regression Fit	43
24. Locations of Seamount Distribution Studies	45
25. Potential Mechanism for Tutuila Offset	47
26. Oblique View of ESVP	71

LIST OF TABLES

<u>Table</u>	<u>Page</u>
1. List of Multibeam Datasets	25
2. Summary of Seamount Shape Statistics	32
3. Studies of Seamount Distribution	44
4. MB-System “mbgrid” Commands	70
5. Seamount Statistics (First Portion)	73
6. Seamount Statistics (Second Portion)	74
7. Calculations of Seamount Density	77
6. Calculations of Natural Log of Seamount Height	78

LIST OF FOLDOUT MAPS

<u>Map</u>	<u>Page</u>
1. Multibeam Compilation	54
2. Breakout of Multibeam Swaths	55
3. Slope Surface	56
4. Locations of Identified Seamounts	57
5. Geomorphological Interpretation	58

The Marine Geomorphology of American Samoa: Shapes and Distributions of Deep Sea Volcanics

1. Introduction

1.1 Overview

The geologic processes at work in American Samoa have long been a point of scientific debate. The origins of its islands and submarine features remain shrouded in uncertainty, though recent efforts have begun to uncover its geologic mysteries. Of its numerous volcanic formations, few breach sea level, leaving an enormous proportion of their mass unavailable to traditional observation. As a result, early investigations of geology in American Samoa were extremely limited. Advancements in submarine exploration over recent decades have made direct observation possible, though ventures in deep sea dredging and submersible deployment demand considerable time and resources. As an efficient alternative, echo-sounding technology has proven effective in surveying large swaths of the sea floor (Davis et al. 1986; Tyce 1986). Many research vessels are now equipped with advanced multibeam sonar systems and an effort to map the world's oceans at high resolutions is now underway (Vogt and Jung 2000).

Investigations of geology in American Samoa date back to the United States Exploring Expedition of 1838-1842 when geologist James Dwight Dana first noted the volcanic nature of the Samoan island chain (Dana 1849). Periodic visits to the islands throughout the first half of the 20th century produced a modest collection of scientific literature and geologic maps. With the arrival of plate tectonics (Hess 1962) and mantle plume (Wilson 1963; Morgan 1971) theories in the 1960's and 70's interest in the Samoan island chain intensified due to their anomalous volcanic characteristics. Past decades of research have focused on the geochemical signatures of both subaerial and submarine rock samples to constrain the mechanism and age of petrogenesis. Though a hot spot mantle plume is considered the most likely origin of the island chain (Hart et al. 2000; 2004), alternative hypotheses have been put forth to explain recent volcanism away from the center of mantle plume activity (Hawkins and Natland 1975; Natland 1980; Natland and Turner 1985).

This study aims to describe the deep sea geomorphology of American Samoa through compilation, quantitative analysis, and qualitative interpretation of multibeam datasets in an

effort to contribute a new perspective on volcanic origins. Compilation of multibeam datasets collected by various primary sources over the last two and half decades is accomplished using the multibeam processing software package MB-System by Caress and Chayes (1996). The high-resolution compilation is then employed to measure shape parameters of small seamounts. Methods of quantitative analysis established by Jordan et al. (1983) and Smith (1988) are then used to assess the geomorphologic implications of shape parameter relationships. A distribution analysis of small seamounts follows, calculating areal density with the exponential distribution model conceived by Jordan et al. (1983) and modified by Smith and Jordan (1988). Finally, a qualitative interpretation of the entire study area is undertaken that includes mapping of major volcanic features, morphologic descriptions of large seamounts, and considerations of age-progression based on arrangements of volcanic lineaments.

1.2 Significance

A greater understanding of marine geomorphology in American Samoa is valuable for both practical and scientific reasons. American Samoa encompasses an Exclusive Economic Zone (EEZ) that adds to a patchwork of United States territorial waters in the Pacific. Multibeam surveys are useful for producing inventories of economic resources in the EEZ, such as suitable fish habitat and viable mineral resources. An interest in fish habitat extends to conservation efforts, where charting of coral reef ecosystems in American Samoa has aided in the management of the Fagatele Bay National Marine Sanctuary (e.g. Wright et al. 2002). Mapping of the deep seafloor is also important for assessing potential geologic hazards, which include submarine mass wasting events, volcanic eruptions, and other potential tsunami triggers (Hill and Tiffin 1991). Monitoring of geologic hazards is particularly relevant in American Samoa, as the region is the site of ongoing and significant volcanic activity, particularly at the eastern end of the archipelago (Hart et al. 2000; Staudigel et al. 2006).

From a scientific viewpoint, the study of geomorphologic formations may provide new insight about the geologic enigma of volcanic origins in American Samoa. To date, only twelve marine features in American Samoa have been identified and described in terms of their morphology, most only briefly (Hart et al. 2000; Hart et al. 2004; Earthref.org 2007). This investigation provides morphological statistics for 51 newly identified seamounts and adds more detail to descriptions of previously identified features. Each new seamount will be submitted to the Seamount Catalog, the preeminent registry of marine formations, which now includes more

than 1,800 entries (Earthref.org 2007). Additionally, shape and distribution analyses may help to predict seamount morphologies and populations in similar geologic environments where high-resolution multibeam bathymetry is unavailable.

Due in large part to the importance of economic inventories and scientific investigation, seafloor mapping as a general pursuit has gained momentum in recent decades. The world's oceans, which account for more than 70% of the surface of the Earth, have not been mapped in their entirety at resolution higher than 1 km (Sandwell and Smith 1997). In fact, our ocean floors “represent one of the most poorly mapped terrestrial surfaces in the inner solar system” (Vogt and Jung 2000). The surfaces of Mars, Venus, and numerous moons have been mapped at spatial resolutions of tens and hundreds of meters. In response, a mission to map the world's oceans using high-resolution multibeam and side-scan sonar has been proposed by the United States Naval Research Laboratory. Unfortunately, the Global Ocean Mapping Project (GOMaP) is still in planning stages and, pending its approval, would require an estimated 215 ship years to survey only the deep water portions of the ocean floor (Vogt and Jung 2000). This underscores the exceptionality of a high-resolution multibeam compilation in American Samoa, with coverage of more than 28,000 km².

1.3 Study Area

American Samoa is a group of small islands and atolls in the southwest Pacific Ocean (**Figure 1**). It was ceded to the United States in 1899 by the Treaty of Berlin. The treaty divided the Samoan archipelago between the United States and Germany. The American territory consists of five islands, Tutuila, Aunu'u, Ofu, Olosega, and Ta'u, and two atolls, Rose and Swains (**Figure 2**). Their combined area is approximately 199 km². All seven islands and atolls are of volcanic origin, though their specific geologic history is not common throughout. This study is concerned only with the Eastern Samoan Volcanic Province (ESVP), as defined by Hart et al. (2004). The ESVP includes the islands of Tutuila, Aunu'u, Ofu, Olosega, and Ta'u; large seamounts and guyots Papatua, Tulaga, Malumalu, Vailulu'u, Malulu, Soso, and Tama'i; and numerous surrounding small seamounts (**Foldout Map 1**). Aunu'u is a tiny satellite island of Tutuila and is considered part of the larger Tutuila volcanic complex. Ofu, Olosega, and Ta'u as a group are often referred to as the Manu'a Islands. Swains Atoll is located approximately 320 km north of the rest of American Samoa, far beyond the extent of the ESVP. Rose Atoll is not

considered part of the ESVP on the basis of geologic characteristics described in more detail in **Chapter 2**.

While the intrigue of scientific controversy played a major role, the availability of multibeam datasets was crucial in the selection of this study area. The work of Wright (2002; 2005), Wright et al. (2002), and Lundblad et al. (2006) laid the foundation for acquisition of multibeam

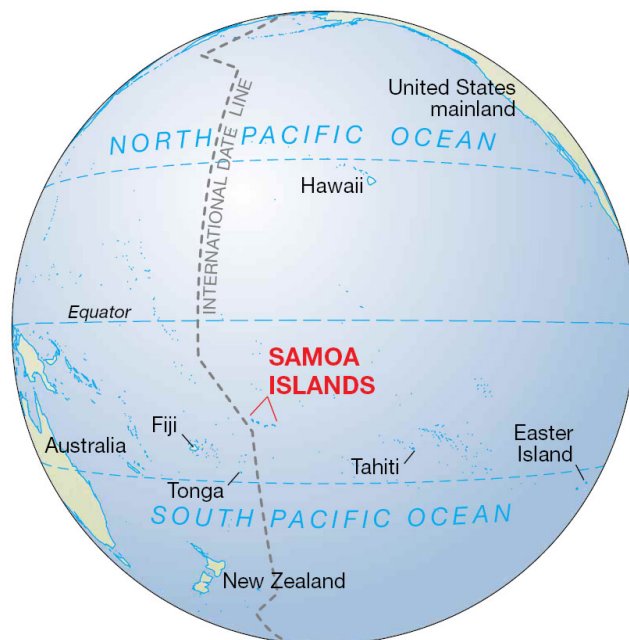


Figure 1: Global view of study area. Map produced by the National Park Service and reproduced by permission.

The ESVP shows evidence of highly complex geologic processes. These processes remain shadowed in uncertainty, though investigations of their underpinnings have garnered momentum and plentitude over the last two decades. These recent studies build upon historic geologic descriptions of the Samoan Island chain (Hawkins 1987), the first of which was published by Dana (1849) at the conclusion of the United States Exploring Expedition of 1838-1842. Though much of his work was focused on Western Samoa, he portrays the island chain as increasing in age from west to east, due to the presence of youthful volcanics on the islands of Savai'i and Upolu.

The first descriptions specific to islands in the ESVP were presented by Friedlander (1910) who cites patterns of erosion on Tutuila as evidence of the western end of the island being more

datasets used in this study. In addition to the aforementioned datasets, the collections of the Scripps Institution of Oceanography (SIO) as cataloged at Earthref.org (2007) were essential. Dataset availability in tandem with delineation of the ESVP thus restricts the study area to the bounds of $13^{\circ}20'S$, $15^{\circ}30'S$, $167^{\circ}30'W$, and $171^{\circ}W$ (Foldout Map 1).

2. Geologic Setting

2.1 Historical Observations

youthful than the eastern end. This observation was in line with Dana's claim of a west-to-east pattern of increasing island age. Friedlander was also the first geologist to visit the Manu'a Islands, noting lavas of recent age on Ta'u, and also receiving an eye-witness account of an 1866 submarine eruption that occurred between Olosega and Ta'u (Stice and McCoy 1968).

Detailed descriptions of the geology of islands in the ESVP were first published by Daly (1924). His interpretation of Tutuila was that of a single volcanic dome, implying the larger shield platform was emplaced from one source. Based on observations of erosional processes, he places the age of the island in the Pliocene epoch, a claim that would be substantiated decades later through radiometric dating of rock samples (McDougall 1985; Natland and Turner 1985). In addition, he recorded structural observations, noting a substantial disturbance due to faulting or slumping that took place as the Tutuila shield was actively building. Daly (1924) also describes a short trip to the Manu'a Islands, remarking on the relative youth of lavas on Ta'u in contrast with the deeply weathered flows on Ofu and Olosega.

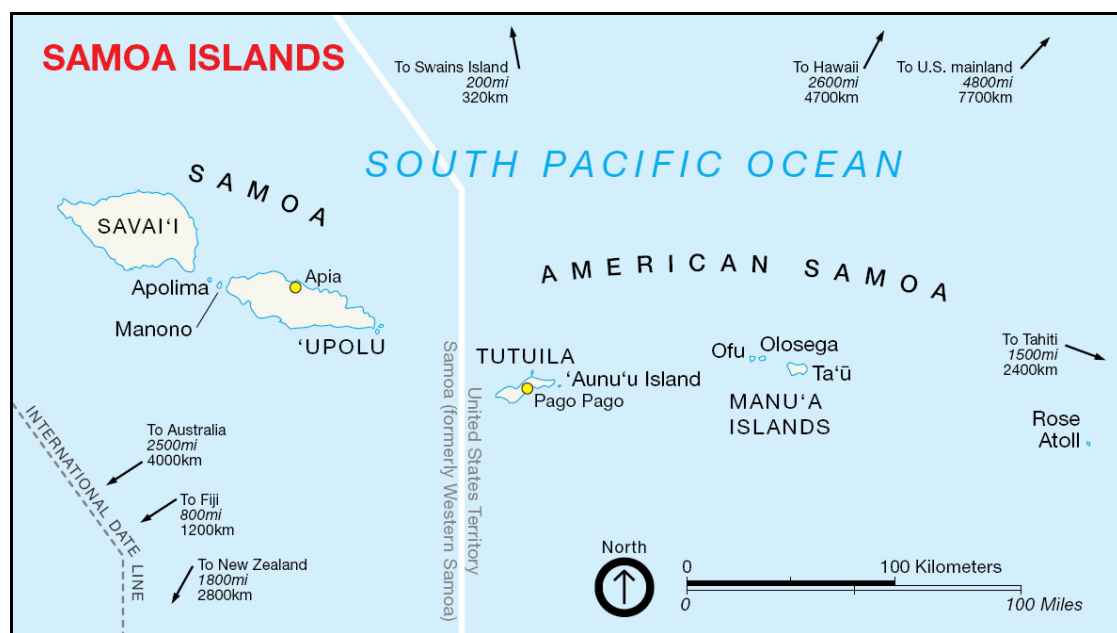


Figure 2: Political map of Samoa Islands. Map produced by the National Park Service and reproduced by permission. Swains Atoll is not included in this view.

Stearns (1944) would undertake the first major work on the islands of American Samoa, writing extensively on their geomorphology and petrology, as well as drafting reconnaissance geologic maps of the islands. His findings suggest that the subaerial portion of Tutuila was formed by

five principal volcanoes located on parallel rift zones with a directional trend slightly north of east, or N70°E (**Figure 3**). He also located numerous dykes and faults with a similar directional trend, ranging from N65-80°E. Stearns recorded shield-building stages dating back to the Tertiary (> 1.8 Ma) and driven by a major underlying fissure system, trending in same direction as subaerial volcanism (N70-75°E). Commenting on the island chain as a whole, Stearns (1944) compares their evolution to that of the Hawaiian Island chain.

Perhaps the most influential contribution of Stearns (1944) to Samoan geology was his recognition of pre- and post-erosional volcanics. In describing island chain stratigraphy, the chronology of formations is broken out in the following manner, from younger to older: (1) Likely historic volcanoes, (2) Erosional Unconformity, (3) Middle and Late Pleistocene volcanics, (4) Great Erosional Unconformity, and (5) Pliocene and Early Pleistocene volcanics. The Great Erosional Unconformity marks a significant stratigraphic division that has been used to differentiate between pre-erosional (i.e. shield volcanics) and post-erosional volcanics. While post-erosional volcanics are ubiquitous throughout the islands of Western Samoa, Stearns (1944) noted their limited presence on Tutuila and the Manu'a islands.

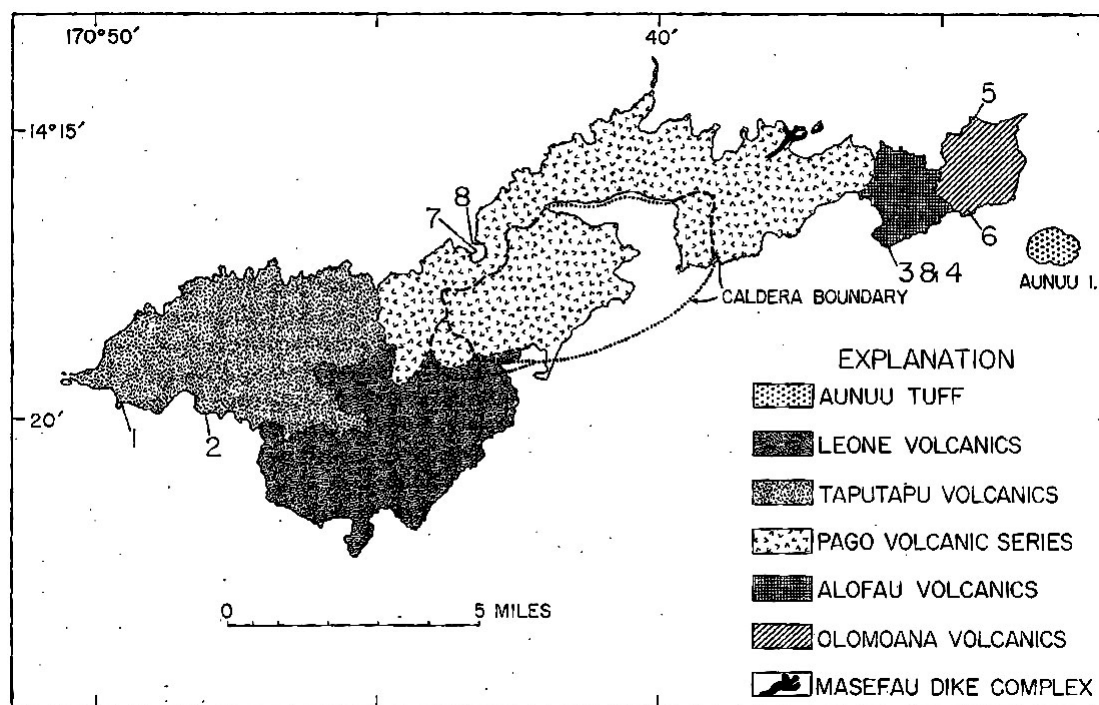


Figure 3: The five major volcanic centers of Tutuila (Stearns 1944). Numbers indicate sampling sites.

Until the work of Stice and McCoy (1968), geologic descriptions of the Manu'a Islands remained rather cursory. The duo created detailed structural maps and cross-sections of all three islands, including the identification of seven unique formations on Ta'u and an additional five on Ofu and Olosega. They describe the history of Ta'u as a single volcanic dome with initial shield-building stages dating back to the Pliocene. By the Pleistocene, the summit had collapsed and two smaller shields had developed along northeast- and northwest-trending rift zones. There is evidence of recent volcanism from three separate cones on Ta'u. Ofu and Olosega are identified as the remnants of at least five cones of similar age to the Ta'u shield. Recent volcanism observed on Ofu is in contrast with Olosega, showing no evidence of recent volcanic activity.

2.2 Early Geochemistry

Using rock samples collected during Stearns' expedition, MacDonald (1968) performed chemical analyses to characterize basalts from Tutuila. Distinctions were drawn between shield and post-erosional volcanism by characterizing the unique chemical signatures of each sample and then comparing those results to the Hawaiian chain, an intensely studied age-progressive volcanic island chain. Basalts in the Hawaiian chain have been segregated into two suites, tholeiitic and alkalic, which are equated generally to shield and post-erosional volcanism, respectively. McDonald (1968) found that all samples collected from Tutuila were alkalic in nature, implying they were erupted after the initial shield-building stage. Although only alkalic basalts were found on the subaerial portion of Tutuila, this did not rule out the presence of submarine tholeiitic basalts.

As a colleague of McDonald's at the Hawaii Institute of Geophysics also studying Samoan basalts, Stice (1968) chemically analyzed samples collected on his visit to the Manu'a Islands (Stice and McCoy 1968). His analyses yielded comparable results, placing all samples in the alkalic suite, and leading him to suggest that basalts from Tutuila and the Manu'a Islands originated from a similar magma source. Stice went on to advocate a mechanism through which alkalic basalts are produced by magma chamber differentiation, where settling of olivine crystals over time causes a chemical divergence within the vertical space of the magma chamber, a process believed to be at work in the Hawaiian chain. While samples resembling a transitional stage between tholeiitic and alkalic were observed, he found that their stratigraphic position did not correlate with their chemical composition when compared to Hawaiian configurations. Due to the paucity of tholeiites, Stice (1968) suggests that the magma source of

the Samoan chain may be deeper than that of its Hawaiian counterpart, a possibility he attributes to its “proximity to the continental borderland.”

2.3 Tectonism and Lithospheric Flexure

The advancement of the theory of plate tectonics in the 1960's (Hess 1962) coupled with the burgeoning theory of mantle plumes (Wilson 1963; Morgan 1971) allowed scientists, for the first time, to make substantial claims about the mechanisms of foundational formation of age-progressive linear island chains. Hawkins and Natland (1975) were the first to apply these theories to the Samoan chain, their work marking the start of continuing interest in the geology of the region by scientists at SIO. Their samples of basalts throughout the island chain were accompanied by the first dredges of submarine seamounts. These samples were characterized as generally alkalic, though they were further differentiated as either nephelinite or basanite. Although there were advances in sampling methods, the basalts collected still only represented the most recent volcanism, as dredging of seamounts only yielded samples from their summits.

Regardless of sampling constraints, Hawkins and Natland (1975) considered the Samoan chain to be “primarily a thick accumulation of alkalic basalts which formed shield volcanoes on a ridge of unknown composition.” This marked a departure from a comparison with the Hawaiian chain, where shield-building basalts were recognized as tholeiitic. They credited chain formation to a close proximity with the Tonga Trench, where the Pacific Plate subducts below the Australian Plate. The unique shape of the Tonga Trench -- oriented in a generally linear north-south direction but curving sharply to the west at its northern terminus -- exhibits a near uniform distance (~150km) to the axis of the Samoan Islands and seamounts. The mechanism for shield-building was thus attributed to an intense deformation of the Pacific Plate lithosphere where it is flexes downward into Tonga Trench and torques about its northern terminus, allowing subsequent upwelling of magma from shallow reservoirs in the asthenosphere (**Figure 4**). While Hawkins and Natland (1975) acknowledge directional similarities to age-progressive island chains within the Pacific intraplate, their proposed mechanism again draws contrast between the Samoan and Hawaiian chains in that only the latter had generally been accepted as the result of a deep mantle plume (Wilson 1963).

Natland (1980) expanded upon his work with Hawkins in the first scientific article published specifically on the age-progression of the Samoan chain, in which he further bolstered the case

for shield-building and post-erosional volcanism as a function of lithospheric flexure. He compares the peculiarities of the Samoan chain to the evolution of typical Pacific linear age-progressive island chains, which can be described in the following four stages: (1) a fixed thermal disruption in the mantle causes localized melting of the lithosphere and results in the extrusion of one or two shield volcanoes; (2) movement of the lithosphere over a more ductile asthenosphere causes volcanoes to shift away from the center of thermal disruption; (3) volcanism diminishes over time and eventually ceases completely; (4) volcanoes undergo a period of extensive erosion where they become reduced to sea level and ultimately submerged. Where this process occurs in a tropical climate, a fifth stage of coral reef proliferation occurs at the island fringe to create atolls that persist after submergence. In noting the differences between this model and the Samoan chain, Natland (1980) first highlights earlier observations that more youthful volcanism is evident on the western island of Savai'i and progressively more eroded surfaces are observed on Upolu and Tutuila (Dana 1849; Friedlander 1910; Stearns 1944). He then points to the presence of a submerged volcano, Rose Atoll, unexpectedly anchoring the eastern end of the island chain. Lastly, Natland (1980) refers to the apparent absence of tholeiitic basalt, which accounts for the bulk of Hawaiian shield basalts.

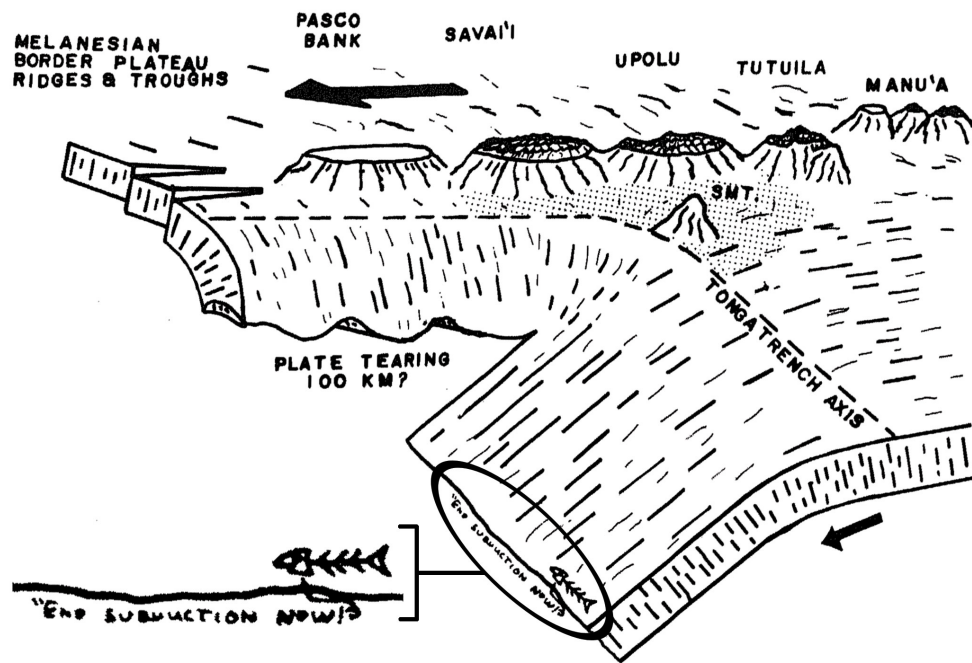


Figure 4: Cutaway diagram of the Samoan region illustrating lithospheric deformation about the “corner” of the Tonga Trench. Figure modified from Natland (1980).

Natland (1980) interprets these ostensible contradictions through the chemical analyses of both post-erosional and shield volcanics while stressing the importance of evaluating age-progression separately on the basis of their unique temporal and distributional properties. Though no decisively tholeiitic basalts are present, basalts in a transitional stage toward alkalic are sampled and considered as shield volcanics. The petrologic distinctions between these transitional and alkalic volcanics is used to adapt a relationship analogous to the tholeiitic-alkalic relationship observed in the Hawaiian chain. In the absence of radiometric ages, Natland (1980) uses paleomagnetic data provided by Tarling (1966) to estimate age ranges for Ta'u (< 0.5 Ma), Tutuila (0.7 to 1.6 Ma), and Upolu (> 1.6 Ma). Given these estimated ages and the transitional-alkalic relationship observed throughout the island chain, he determines that the age-progression of shield volcanism is in fact east-to-west, reversing previous speculation (Dana 1849; Friedlander 1910; Stearns 1944). This age-progression is in accordance with those of other Pacific linear island chains whose origins are understood as plume-driven. Yet Natland (1980) avoids categorizing the Samoan chain alongside plume-driven chains such as the French Polynesians and Hawaiian, noting its relative structural and petrologic diversity. He terms any presence of a deep mantle plume in this location as "fortuitous," instead favoring a shallow magmatic source released from the asthenosphere through intense lithospheric deformation occurring at the "corner" of the Tonga Trench.

Post-erosional volcanism is observed as nearly simultaneous by Natland (1980), spanning across a rift zone of at least 300 km, with subaerial eruptions ranging west to east from Savai'i to Tutuila. He notes the near-parallel arrangement of the Tonga Trench to this rift zone. As the Pacific Plate moves with respect to the northern terminus of the Tonga Trench there is a transition from subduction to an arc-arc transform fault where Natland proposes deformation is dominated by bending rather than a faulting system. This is based on significant seismicity on the opposite side of the Tonga Trench (Barazangi and Isacks 1971), beneath the Lau Basin, thought to be the location of plate rupture. Natland (1980) claims the lateral bending of the plate begins at Upolu, the fulcrum of which is located 100 km below the island. On the basis of plate thickness (less than 100 km) taken from the inferred source depth of post-erosional volcanism, bathymetry, and the nature of seismicity, Natland (1980) proposes that "plate bending provides the principle zone of dilatancy allowing post-erosional lavas a route to the surface."

2.4 Radiometric Dating

Attempts to constrain the complex geochronological framework of the Samoan chain are afforded additional credence with the application of radiometric dating techniques. Known isotopic decay rates of elements found in basalts allow for absolute dating of volcanic samples. The first radiometric ages for the Samoan chain were published in 1985 in three separate articles. McDougall (1985) dated 38 samples from the subaerial shield volcanoes of Tutuila using the K-Ar technique. His findings place the age of the island between 1.54 Ma and 1.00 Ma, dates that align well with paleomagnetic ages (Tarling 1966). Pago Volcano, which accounts for the largest area of Tutuila, shows ages from 1.54 Ma to 1.28 Ma, leading McDougall to assert the main subaerial shield-building occurred on the island for an interval of only 0.6 Ma. Unpublished K-Ar ages for the Manu'a Islands are mentioned (0.3 Ma for Ofu/Olosega and 0.1 Ma for Ta'u) so as to comment upon the conformity in both direction and age-progression within the ESVP to the predicted Pacific Plate movement of about 10 cm/yr (Jarrard and Clague 1977; McDougall and Duncan 1980). Unpublished K-Ar ages for Upolu are also consistent with Pacific Plate motion, persuading McDougall (1985) to endorse the Samoan chain as a mantle plume trace, while acknowledging the possibility that lithospheric deformation may account for youthful volcanism at the western end of the chain.

Natland, this time along with Turner (1985), once again attempts to construe the age-progression of the Samoan chain armed with his own K-Ar and $^{40}\text{Ar}/^{39}\text{Ar}$ ages. Duncan (1985) supplements their analyses with ages from the far western end of the island chain in his concurrent study of geochronology in the New Hebrides-Samoa region. Natland and Turner present ages in good agreement with those revealed by Tarling (1966) and McDougall (1985), deriving ages between 1.40 Ma and 1.03 Ma for eruptions on Tutuila. They also report ages ranging from 2.80 Ma to 1.51 Ma on Upolu. These data coupled with ages from Duncan (1985) also conform to a fixed magma source with respect to predicted plate motion. However, Natland and Turner (1985) decline to suggest the possibility of a mantle plume source, instead pointing to shield-building occurring at a fixed distance from the "corner" of the Tonga Trench over the last 13.5 Ma. They maintain that post-erosional volcanism remains strongly attributed to structural deformation in this location.

Though without substantial progress on an understanding of volcanic mechanisms in the region, Natland and Turner (1985) indicate advances with regard to the relationship of shield

and post-erosional volcanics. The first mineralogical evidence of genuine tholeiitic basalt in the island chain is revealed in a sample from Upolu. Tholeiitic basalt, though still not discovered in the ESVP, is thought to exist in certain remote areas of Tutuila based on stratigraphic associations similar to those observed on Upolu. This is significant for drawing comparisons to comparably well understood Hawaiian geochemical timing. Tholeiitic dominated Hawaiian shield volcanoes were built over a period of 0.5 Ma and then capped by alkalic basalts (MacDonald and Abbott 1970). By extrapolating the periods and volume of alkalic subaerial volcanism (0.7 Ma on Tutuila and 1 Ma on Upolu) in comparison to Hawaiian evolution, Natland and Turner (1985) speculate the minimum age for shield-building as 1.8 Ma for Tutuila and 2.7 Ma for Upolu. From geochemistry taken by Hubbard (1971) on Ta'u, a minimum shield age of 0.5 Ma is assumed.

2.5 Advanced Geochemistry

With the sources of shield and post-erosional volcanism little understood, studies were initiated that employed techniques in isotopic geochemistry to better distinguish their magmatic reservoirs. Wright and White (1987) produced the first comprehensive investigation of isotopic signatures in the Samoan chain, analyzing samples from Savai'i, Upolu, Tutuila, and the Manu'a Islands. Several isotopic ratios of Sr, Nd, and Pb are compared that establish characteristic data plots for both shield and post-erosional volcanics, suggesting that each have unique magmatic sources. In comparing the shield data range with that of other Pacific islands a significant overlap is observed with French Polynesian shield volcanics, conveying the possibility of a common magmatic reservoir. Post-erosional volcanics, on the other hand, diverge clearly from those of French Polynesia. Due to a negative relationship of $^{207}\text{Pb}/^{204}\text{Pb}$ and $^{206}\text{Pb}/^{204}\text{Pb}$ ratios, Wright and White (1987) propose that recent subaerial volcanics are derived from a mixing of the shield and post-erosional magmatic sources. The isotopic signature of shield volcanics is well constrained, therefore allowing an "unmixing" of sources to isolate a Samoan post-erosional end-member.

Based on the isotopic signature of their hypothetical post-erosional end-member, Wright and White (1987) theorize that its source is enriched by recycled subducted oceanic crust and sediment. Additionally, this study confirms that Samoan post-erosional volcanics are dissimilar in isotopic signature from their Hawaiian counterpart. Previous observations of Samoan post-erosional volcanism place its proportion of overall island volume very high (~ 30%) when

compared with Hawaii (< 1%) and note its virtually simultaneous eruptive state across its rift (Stearns 1944). Wright and White consequently advocate the plausibility of lithospheric flexure as the eruptive mechanism (Hawkins and Natland 1975; Natland 1980; Natland and Turner 1985). Nevertheless, the exact location of an enriched magmatic source remains unclear, though Wright and White favor a “chemically anomalous” lithospheric or asthenospheric origin.

Wright and White (1987) disagree with lithospheric flexure as the mechanism for shield volcanism, however, citing several reasons. First, they recount Abbott and Fisk (1986) who assert that stress along the Tonga Trench could not cause lithospheric fracturing beyond 200 km, thereupon unable to account for volcanism in the Manu’a Islands. Second, globally there are other locations of subduction where flexural stress would in theory be sufficient to result in volcanism, though there is none. In addition, isotopic signatures of Samoan shield volcanics match those of French Polynesia, padding other consistencies (McDougall 1985; Natland and Turner 1985) with the mantle plume hypothesis. Wright and White (1987) thus see “no compelling reason why the plume model should not be applied to Samoan shield volcanism.”

Further advancement of isotopic geochemistry provided better appreciation of the potential magmatic sources of oceanic rocks. As magma rises through the lithosphere few elemental isotopes remain uncontaminated while managing to represent a variety of mantle sources. This concept informed the previous work of Wright and White (1987). Through further geochemical analyses performed on oceanic rocks representing diverse geologic settings, isotopic ratios of Sr, Nd, and Pb have emerged as diagnostic of four primary end-member mantle sources (White 1985): depleted MORB (mid-oceanic ridge basalt) mantle (DM), two types of enriched mantle (EM₁ and EM₂), and an end-member with high U/Pb ratios (HIMU). Combinations of these four end-members are thought to describe the origin of every type of oceanic rock. While end-members exist at uncommon extrema, two other sources are theorized to exist at their center (i.e. near equal combinations of all four end-members), defined by high ratios of an additional elemental isotope lineage, $^3\text{He}/^4\text{He}$ (Craig and Lupton 1981). The high ratio of $^3\text{He}/^4\text{He}$ is thought to signify (1) a “primitive” mantle source where magma of primordial origin has somehow avoided degassing (i.e. loss of He) throughout earth’s history, and (2) a “subducted He” source where un-degassed magma reaching the crust is recycled into the mantle through subduction. The former is thought to be the manifestation of mantle plumes (Craig and Lupton 1976), while Kurz et al. (1982) suggest the latter is related to EM sources.

Farley et al. (1992) use the aforementioned isotopic framework to describe alkalic basalts collected from the Pago shield volcano of Tutuila. Their results rendered these Samoan basalts as exceptional, if not somewhat problematic. High ratios of both $^3\text{He}/^4\text{He}$ and $^{87}\text{Sr}/^{86}\text{Sr}$ suggest both primitive and relatively young recycled crust sources, respectively. $^3\text{He}/^4\text{He}$ ratios are so high that Farley et al. cannot attribute the source to recycled crust alone, ruling out a traditional subducted He source. Thus, they propose the following two possibilities: (1) primordial He was not extracted during subduction and recycling, or (2) there was so little He in the recycled material its presence was erased and replaced by a much more dominant He source. Regardless of the exact mechanism, both scenarios suggest that a primitive magma source plays a major role in the region. Farley et al. (1992) go on to suggest that these particular Samoan basalts are result of “binary mixtures between two homogenous and isotopically extreme components: a relatively young recycled crustal material, and a largely un-degassed and possibly primitive mantle,” which they find consistent in part with mantle plume upwelling.

2.6 Mantle Plumes

Much of the recent geochemical and geochronological investigations in the ESVP have been spurred on by the discovery of current volcanism on the undersea volcano of Vailulu'u, located 45 km east of Ta'u (Hart et al. 2000). Vailulu'u, first discovered in 1975 by Johnson (1984), is now widely accepted as the current location of the Samoan hotspot. Dredging of alkalic basalts and subsequent geochemical analyses by Hart et al. place Vailulu'u within the Samoan “pedigree” defined by Sr, Nd, and Pb isotopes. Though still high, ratios of $^3\text{He}/^4\text{He}$ have subsided slightly relative to basalts on Tutuila (Farley et al. 1992). $^{210}\text{Po}/^{210}\text{Pb}$, an isotopic ratio used to date very young oceanic rocks, confirms ages of less than 50 years. Reinforcing this young age and continuing volcanic activity, analysis of the water column above Vailulu'u shows strong evidence hydrothermal venting. Hart et al. (2000) go farther than to simply acknowledge Vailulu'u as additional evidence for a mantle plume source in Samoa, instead claiming that the Samoan chain perhaps represents a more “standard model” of an intraplate hotspot island chain than the Hawaiian example (**Figure 5**). The basis for this lies in the paucity of tholeiitic basalts in many other proposed hotspot chains (i.e. MacDonald-Austral chain, Teahitia-Society chain, Adams and Bounty-Pitcairn chain).

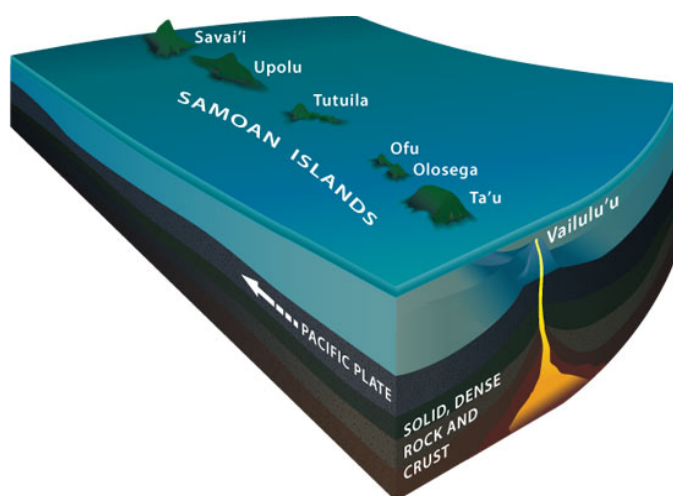


Figure 5: Illustration of the Samoan hotspot by Jayne Doucette, Woods Hole Oceanographic Institution (Oceanus 2005).

submarine dredges of basalts on Combe (11.12 Ma) and Alexa Banks (23.94 Ma), located west of Savai'i, that match well with predicted plate motion. However, while a previous age of Lalla Rookh (8.9 Ma) also matches this progression (Duncan 1985), the new date presented by Hart et al. is significantly younger (1.62 Ma). Nevertheless, all samples fall within the isotopic Sr-Nd-Pb Samoan pedigree, suggesting that the Lalla Rookh sample is of post-erosional origin. Hart et al. (2004) also cite recent seismic tomography images that illustrate a deep plume stem below the Samoan chain (**Figure 6**).

The swan song for a shield-building lithospheric flexure hypothesis is perhaps cued by the geodetic reconstruction of the Samoan region produced by Hart et al. (2004). Measurements taken at numerous geodetic stations throughout the region are used to realign the Samoan chain with respect to the Tonga Trench through recent geologic history. The reconstruction shows that the Tonga Trench would have been 1500 km away from Savai'i at 5 Ma, the location of shield volcanism at that time. The migration of the Tonga Trench eastward has been rapid though (> 190 mm/yr), allowing for sufficient proximity by perhaps 1-2 Ma to produce the large quantities of "rejuvenated" (i.e. post-erosional) volcanics observed on Savai'i. Given the existence of a mantle plume, Hart et al. also comment on its probable interaction with the Tonga Trench over time, suggesting a northeast push as the subducting slab migrates toward the east. The surface expressions of this are "en echelon lineaments" propagating to the northeast. Three disjointed rift zones are evident: (1) Savai'i to the western shield of Tutuila, (2)

Hart, along with others (2004), continued his investigation of Samoan volcanism, publishing a comprehensive study of the Western Samoan Volcanic Province. Hart et al. take this opportunity to pursue a systematic dismantling of lithospheric flexure as the source of shield volcanism along the Samoan chain. Bolstering evidence for an east-to-west age-progression, $^{40}\text{Ar}/^{39}\text{Ar}$ ages are derived from

the eastern shield of Tutuila to Malumalu, and (3) Muli to Vailulu'u. Finally, Hart et al. (2004) credit any off-axis volcanism (e.g. Papatua) to decompression melting resulting from possible vertical flow of the mantle as it responds to slab migration.

Building upon the work of Wright and White (1987) and Farley et al. (1992) to constrain the magmatic source and mechanism of emplacement in the Samoan chain, Workman et al. (2004) propose a modified version of the standard oceanic lithosphere recycling model to explain the nuances of isotopes in Samoan basalts. Farley et al. (1992) and others (Zindler and Hart 1986;

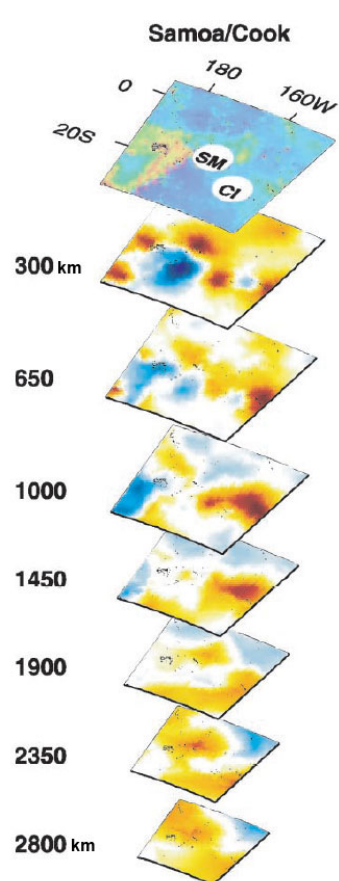


Figure 6: Tomographic imaging of mantle plume stem below the Samoan and Cook islands (Montelli et al. 2004).

Wright and White 1987; Hauri and Hart 1993) have recognized isotopic signatures of Samoan basalts as indicative of the EM2 end-member. Workman et al. maintain, however, that the standard recycling model could not have produced Samoan basalts due to their high $^3\text{He}/^4\text{He}$ ratios and low $^{187}\text{Os}/^{188}\text{Os}$ ratios. Using these two isotope signals in addition to Sr-Nd-Pb ratios, an improved Samoan EM2 end-member is defined through analysis of samples from Vailulu'u, Muli, Malumalu, Upolu, and Savai'i. Workman et al. describe the Samoan EM2 end-member as ancient oceanic lithosphere (2.5 Ga) metasomatized (i.e. hydrothermally altered) and subsequently recycled into the deep mantle via subduction where it remains stored until transport by plume action.

In addition to defining the Samoan EM2 end-member, Workman et al. (2004) note distinct geochemical trends in the two *en echelon* lineaments dominating the ESVP. The "Malu Trend," anchored in the east by Malumalu, is distinct in its $^{206}\text{Pb}/^{204}\text{Pb}$ ratios from a second "Vai Trend," anchored similarly by Vailulu'u. While these trends are

discernable as separate, they progress in the same fashion, with $^{206}\text{Pb}/^{204}\text{Pb}$ ratios increasing with volcanic youth. Though Malumalu has not been dated using argon techniques, these isotope ratios have been used as a proxy to estimate its age. Interestingly, this suggests that Malumalu is not significantly older than Vailulu'u, if not of the same age. These trends also

help to gauge the probable age of Muli, placing it slightly younger than Tutuila, yet somewhat older than Malumalu (Figure 7).

2.7 Mantle Plumes vs. Lithospheric Flexure

Though not officially published in a peer-reviewed forum, Natland (2004) revamps his theory of shield-building lithospheric flexure, claiming a shallow and heterogeneous magmatic source characterized by variable $^{87}\text{Sr}/^{86}\text{Sr}$ ratios released through structural stresses related to the Tonga Trench, despite assertions that the trench is not currently within a feasible distance to cause this stress (Abbott and Fisk 1986; Wright and White 1987). While Natland has not yet challenged this claim or the geodetic reconstruction produced by Hart et al. (2004), lithospheric flexure breathed new life with the discovery of alkalic volcanism in front of the Japan and Kuril trenches (Hirano et al. 2006). Nevertheless, until some new evidence is put forth, it appears that shield-building was not likely caused by lithospheric flexure anywhere along the Samoan chain. Therefore, based on current indications, the Samoan chain, and hence the ESVP, appears to be a geologic environment influenced primarily by a mantle plume.

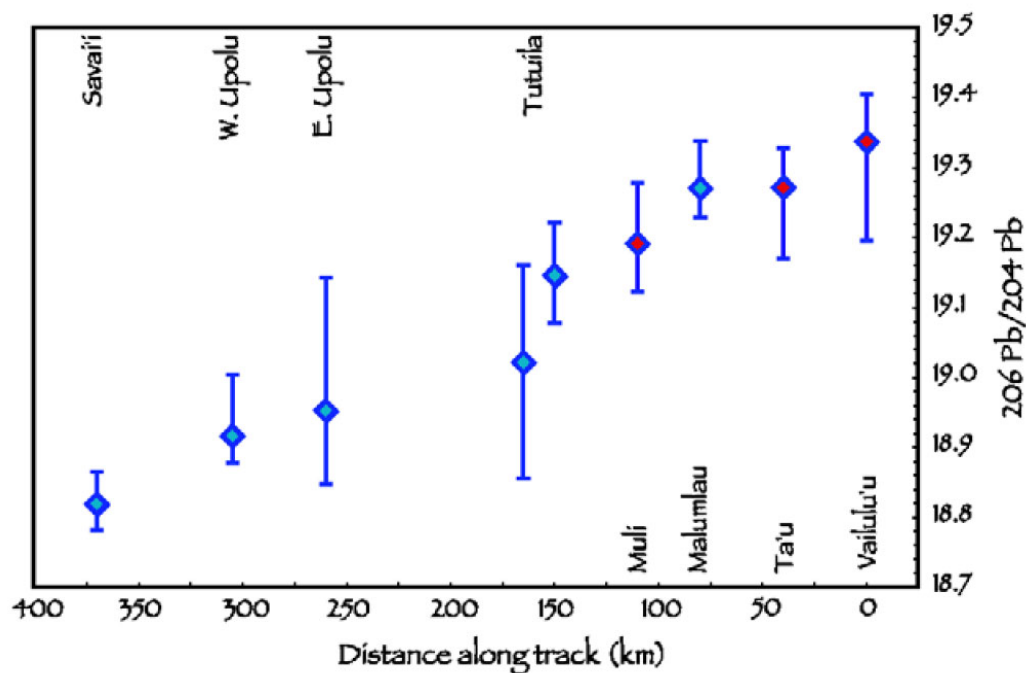


Figure 7: Plot of $^{206}\text{Pb}/^{204}\text{Pb}$ ratio values along the Samoan chain (Workman et al. 2004). These values have been used to approximate age in the absence of argon methods.

It should be noted that while a mantle plume has emerged as the most likely candidate to produce volcanism in the Samoan region, there remains both mechanistic and semantic disagreements about what constitutes a mantle plume (Anderson and Natland 2005). The physics of mantle convection are based upon laboratory experiments and computer simulations, both unable to accurately account for pressure schemes and other variables at work within the mantle. Anderson and Natland (2005) also scrutinize the apparent interchangeable use of the words *plume*, *hotspot*, and *anomaly* in the scientific literature. They claim this is problematic when, for instance, the word *anomaly* is used, implying that the composition of the upper mantle is homogenous, an assumption that has not been substantiated. Vagueness is likewise an issue, evident in the fluctuation of mantle plume counts from an initial figure of 20 (Wilson 1963; Morgan 1971) to 117 (Burke and Wilson 1976), and now hovering around 50 (Courtillet et al. 2003). Side-stepping completely the mantle plume hypothesis as currently defined (or not defined, for that matter), some would prefer a general theory of plate tectonics where the energy of subducting plates is sufficient to stir up the underlying mantle and self-perpetuate plate progression. Notwithstanding, Anderson and Natland (2005) acknowledge that the mantle plume hypothesis “will continue to be the reigning paradigm for some time to come, in spite of its shortcomings.”

2.8 Rose Atoll

Rose Atoll, the easternmost island of American Samoa, has received little attention so far in this review of Samoan geology. This is due to its geochemical dissimilarities with the rest of the Samoan chain, as observed by Rodgers et al. (2003) in their investigation of the only known basalts collected from Rose Atoll. Though no age measurements or isotopic analyses of Nd, Pb, or He were conducted, samples show low $^{87}\text{Sr}/^{86}\text{Sr}$ ratios which serve contrary to the high ratios seen as a hallmark of Samoan volcanism. Rose Atoll is located far to the east of the Tonga Trench, well outside of its potential stress field, and also to the east of Vailulu'u, considered to be the current location of hotspot volcanism in the Samoan chain. Rodgers et al. (2003) reconstruct of the Samoan chain with Rose Atoll located at “zero age” to illustrate its implausibility as the current hotspot location with regard to known ages and plate motion. Lastly, Rose Atoll shows a highly eroded edifice with stellate morphology, suggesting it is substantially older than volcanoes of the ESVP (Mitchell 2001). Rose Atoll is therefore not

considered a part of the ESVP and is perhaps the product of volcanism in the Cook-Austral region or ancient ridge-origin and plate transport.

3. Bathymetry and Compilation

3.1 *Early Bathymetry*

The first official scientific survey of the Samoan Islands came as part of the great United States Exploring Expedition of 1838-1842 (Wilkes 1843). The Exploring Expedition charted the waters along its path by dropping leadlines to infer the underlying bathymetry. This was not an efficient means of measuring depth considering leadlines could take tens of minutes to reach the seafloor, with even more time required to pull up the line. A significant improvement in sounding technology came in 1911 when Reginald Fessenden invented a sound oscillator to identify horizontal obstructions such as ice bergs. While testing the system, it was discovered that sound was returned both horizontally *and* vertically, marking the birth of modern seafloor echo-sounding (Theberge 1989). The Scripps Institution of Oceanography (SIO) performed single-beam echo-sounding of the South Pacific during its 1952 Capricorn Expedition, which first measured the 10,800 m deep Tonga Trench. Soundings from this and subsequent SIO expeditions formed the foundation of the *Bathymetry of the South Pacific* map series (Mammerickx et al. 1973) that include the first bathymetric charts of the Samoan region (**Figure 8**). This map compilation made possible early investigations of marine geomorphology around the Samoan Islands (Hawkins and Natland 1975; Natland 1980).

3.2 *Multibeam Bathymetry*

Further modification of echo-sounding technology resulted in the unveiling of SeaBeam by General Instruments Corporation, the first multibeam echo-sounding system. SeaBeam employed an array of 16 echo-sound beams to survey swaths of the seafloor at an angle of 2 and $\frac{2}{3}^\circ$ across ship track (Davis et al. 1986). SeaBeam was first installed on the French research vessel (R/V) *Jean Charcot* in 1977. By 1980 a total of ten vessels were equipped with SeaBeam (Turko and Agapova 2003), including SIO's R/V *Thomas Washington* (Theberge 1989). SeaBeam was proven to be a robust system capable of operating effectively in various environments, surveying depths as deep as 11,000 m (Davis et al. 1986). Its ability to combine echo-sounding

and computer technology to produce streaming images of the seafloor in near real-time became vital to marine exploration.

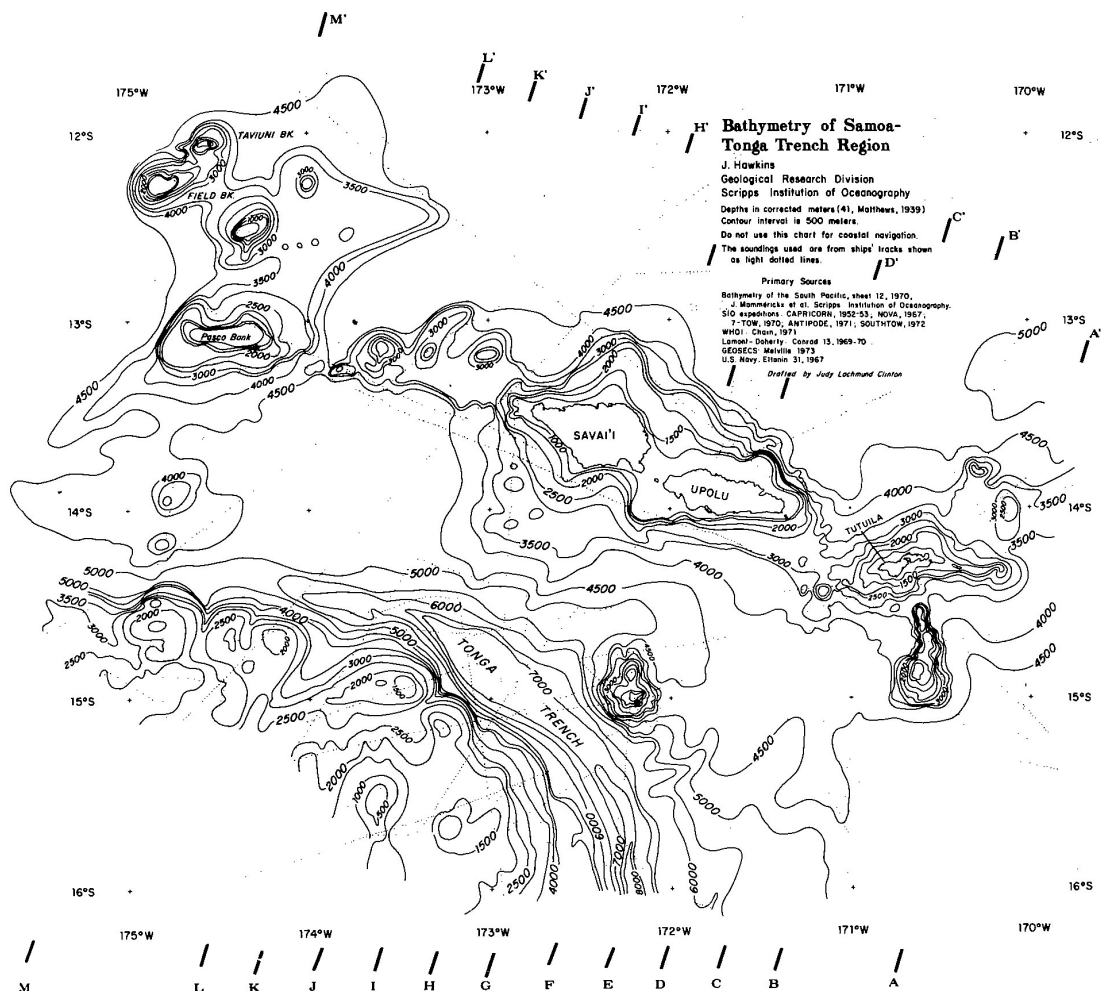


Figure 8: Bathymetric map of the Samoa Island region. Excerpt from the *Bathymetry of the South Pacific* map series produced by the Scripps Institution of Oceanography (Mammerickx et al. 1973). Appears in Hawkins and Natland (1975).

Multibeam technology has improved vastly since the original SeaBeam. Today more than 730 vessels (Turko and Agapova 2003) are now equipped with updated versions of SeaBeam (e.g. SeaBeam 2000, SeaBeam 2100) or other makes (e.g. Simrad, Reson SeaBat) (Figure 9). Multibeam arrays have increased from 16 beams to upwards of 150 beams capable of surveying swaths of up to 40° across track and to depths of 10,000 m. Modern multibeam systems are comprised four parts: (1) The transmitting antennas and subsystem, (2) the receiving antennas and subsystem, (3) the bottom detector unit, and (4) the operator unit (Turko and Agapova

2003). The transmitting subsystem forms and issues beams at frequencies of 12 kHz for most deep water systems. When the beam returns from the seafloor, the receiving subsystem amplifies and converts the analog signal into a raw digital format, which the bottom detector unit converts to depth. The operator unit then combines depth from the bottom detector, navigational information from a GPS, and a profile of sound speed throughout the water column to make final conversions of depths for each beam. Some post-processing, such as prescribed data filtering or ping-editing of outlying depths, may be necessary to correct systematic or isolated errors, respectively (Turko and Agapova 2003).

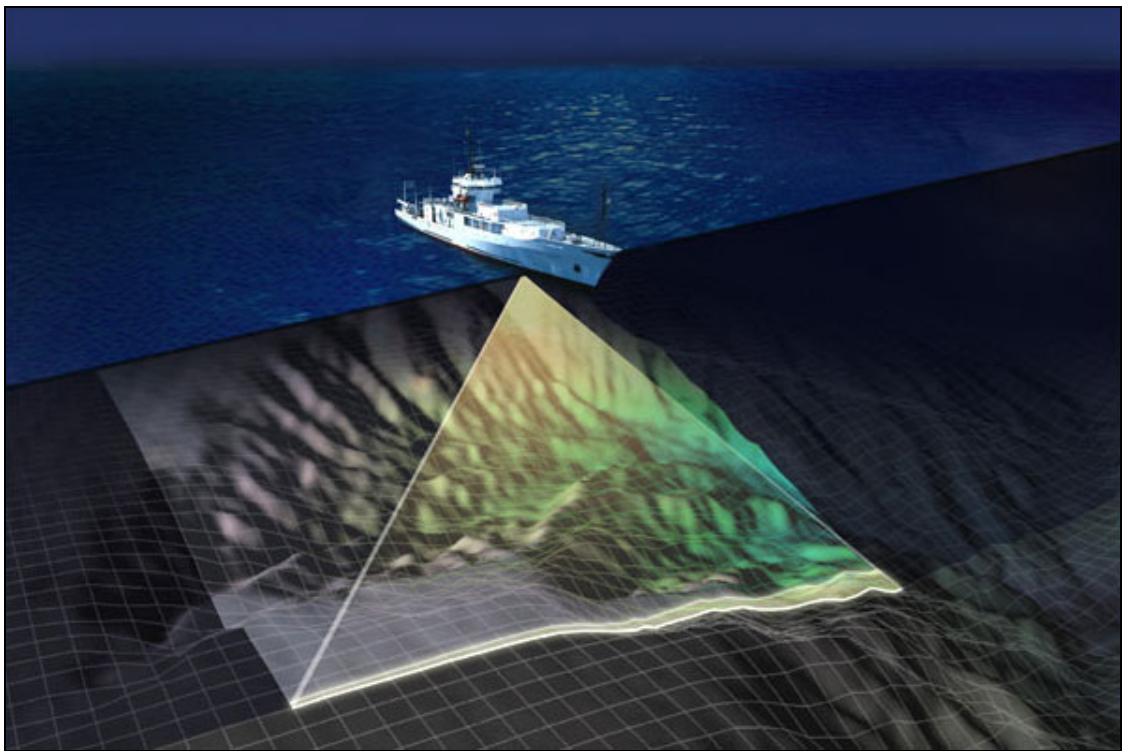


Figure 9: Illustration of multibeam system in use (Lost City Expedition 2003).

The increasing complexity of these systems is accompanied by challenges in ensuring and assessing accuracy. Accuracy is a function of both horizontal and vertical distance from the multibeam sensor, as well as physical properties of water column. Complicating matters, ships are unstable platforms prone to positional motions of pitch, roll, and yaw. To evaluate the combined effect of these factors, de Moustier (2002) made an accuracy assessment of the Simrad EM120 (191 beams) aboard the SIO R/V *Revelle*, a system capable surveying at 70° across-track for average ocean depths (~4,000 m). Dynamic GPS and shipboard motion sensors are

used to correct for positional inconsistencies. De Moustier (2002) found that after positional correction, surveys of average ocean depths demonstrated depth uncertainties below 0.2% for angles at or below 60°. From 60° to 70°, however, depth uncertainties increased considerably to 2% (Figure 10).

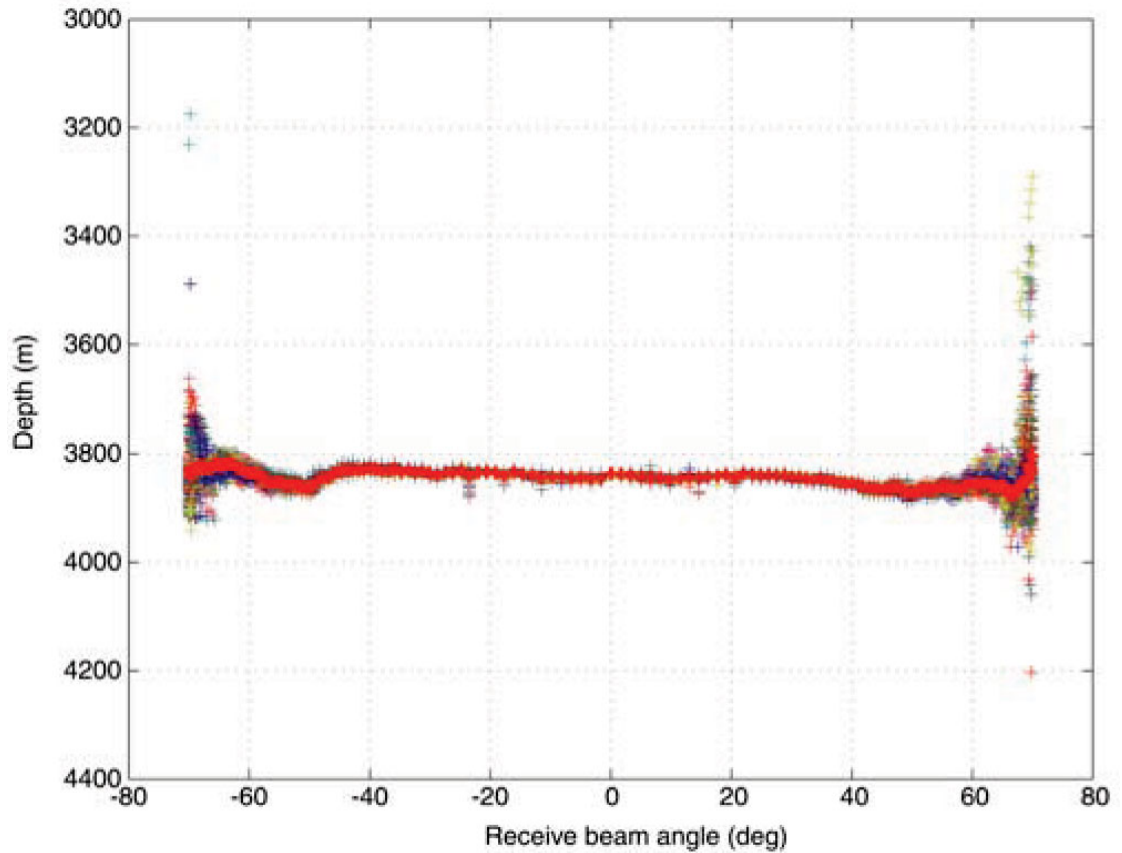


Figure 10: Data plot of depth values produced by Simrad EM120 multibeam system aboard R/V Revelle. Crosses represent observed depth readings. The red line represents the average depth value recorded at the corresponding across-track angle. This illustrates the error incurred as the across-track angle increases (de Moustier 2002).

3.3 *Early Applications in Marine Geomorphology*

High-resolution multibeam bathymetry is well suited for a variety of applications in marine geomorphology. In the same way topographic maps provide insight about terrigenous geomorphology, multibeam bathymetry is the first step in understanding the processes that form and shape marine features. In review of some early applications of multibeam bathymetry, Davis et al. (1986) summarize several approaches toward identifying and characterizing marine geologic features. On the Juan de Fuca spreading ridge in the northeast Pacific, multibeam surveys allowed scientists to identify numerous normal fault scarps perpendicular to the ridge. Over-flowing of recent volcanism and disruption of sedimentation provides clues about the relative age of these faults. Another study in the Cape Mendocino region off northern California used multibeam to map a thrust fault and evidence of mass wasting at the site of a large seismic event in 1970. This discovery of fault activity coupled with continuing seismic observation can help in estimating recurrence intervals of major events.

Throughout the early years, multibeam bathymetry was utilized almost solely for reconnaissance mapping. While exploratory mapping remains the predominant motivation for multibeam surveys, Goff and Jordan (1988; 1989) expand on this by applying statistical methods to classify and *predict* geomorphological provinces across the seafloor. They focus primarily on the lengths, shapes, and orientations of abyssal hills. Formed at spreading ridges and covering nearly 80% of the seafloor (Bell 1975), abyssal hills are the most pervasive marine features. Goff and Jordan (1989) partition the statistical characteristics of the seafloor into both large-scale (province) and small-scale (abyssal hill) behaviors. After devising an algorithm suitable at both scales, several numerical tests are run against actual SeaBeam data. While citing caveats (e.g. sonar error, potential for non-Gaussian distributions of seafloor depths) typical of statistical prediction, Goff and Jordan (1989) find good agreement between their quantitative model and real-world observations. Their research efforts mark some of the first to construct a predictive model of seafloor geomorphology using shape and distribution characteristics of marine features, a methodology that has persisted and is in part the focus of the present study.

At this time Jordan was also involved in the development of a similar predictive model to describe another prevalent seafloor feature, the seamount (Jordan et al. 1983; Smith and Jordan 1988). Produced in not only spreading ridge environments, seamounts are associated with ocean-to-ocean plate convergence and hotspot activity (and lithospheric flexure?). As in the

identification of faults and hydrothermal venting outlined by Davis et al. (1986), early multibeam surveys were also being carried out to study seamounts (Hollister et al. 1978; Smoot 1982; Fornari et al. 1983; Searle 1983; Smoot 1983a, 1983b; Mougénot et al. 1984; Vogt and Smoot 1984; Litvin et al. 1985; Smoot 1985). These descriptions formed the foundation of morphological data from which a predictive model for seamount shape and distribution would be defined. This model and its application in the ESVP will be discussed in detail in **Chapter 5**.

3.4 Datasets

The multibeam bathymetry datasets used in the present study come from various sources (**Table 1; Foldout Map 2**). These bathymetric surveys often served multifaceted objectives, though they can be separated into three principal groups: (1) geophysical surveys, (2) biological surveys, and (3) transit surveys. With the exception of several small swaths collected by NOAA Pacific Islands Fisheries Science Center (PIFSC) in 2006, these datasets account for all known multibeam surveys in the ESVP.

Two major geophysical surveys have been undertaken in the ESVP. The first, in 1999, was the AVON Expedition, launched by SIO and Woods Hole Oceanographic Institute (WHOI) to investigate recent seismic events east of the Manu'a Islands, leading to the rediscovery of Vailulu'u. This expedition collected hundreds of square kilometers of multibeam bathymetry and dredged numerous sites, from which advanced knowledge of Samoan geochemistry was gained (Hart et al. 2000; 2004; Workman et al. 2004). A follow-up to the AVON Expedition was launched in 2005. The ALIA Expedition traversed the entire Samoan chain, again collecting vast swaths of multibeam bathymetry and dredging rock samples throughout. Several more studies of geochemistry in the ESVP were published as a result of ALIA, and geochronological investigations are forthcoming (Jackson and Hart 2006; Workman et al. 2006; Jackson et al. 2007). These expeditions account for the majority of multibeam coverage in this compilation.

American Samoa is host to a diversity of marine life, largely dependent upon its coral reefs. To gauge the health of these ecosystems, several cruises were launched in the early 2000's to map the near-shore bathymetry in American Samoa. In 2004, the NOAA PIFSC surveyed the flanks of Tutuila and the Manu'a Islands for management of benthic habitats associated with coral reefs (PIBHMC 2004). The following year, Hawaii Undersea Research Lab (HURL) initiated another survey of the Tutuila near-shore, this time accompanied by submersible dives again

aimed to document characteristics of the benthic habitat (Wright 2005). HURL extended its benthic habitat surveying to Rose Atoll in 2006 (Smith et al. 2006). This multibeam dataset is the most current to be included in this compilation.

Table 1: List of multibeam datasets used to create multibeam compilation. SIO – Scripps Institution of Oceanography; OSU – Oregon State University; WHOI – Woods Hole Oceanographic Institution; URI – University of Rhode Island; USF – University of South Florida; PIFSC – NOAA Pacific Islands Fisheries Science Center; UHMC – University of Hawaii Marine Center; HURL – Hawaii Undersea Research Laboratory. These datasets are freely available from the Seamount Catalog at Earthref.org (2007).

Cruise ID	Year	System	Institution	Chief Scientist or Contact	Research Vessel
MRTN05WT	1984	SeaBeam	SIO	Peter Lonsdale	R/V <i>Thomas Washington</i>
PPTU03WT	1985	SeaBeam	SIO	Jacqueline Mammerickx	R/V <i>Thomas Washington</i>
PPTU04WT	1986	SeaBeam	SIO	James Hawkins	R/V <i>Thomas Washington</i>
RNDB15WT	1989	SeaBeam	SIO	James Hawkins	R/V <i>Thomas Washington</i>
RNDB16WT	1989	SeaBeam	SIO	Peter Guenther	R/V <i>Thomas Washington</i>
BMRG08MV	1996	SeaBeam 2000	OSU	S. Bloomer/Dawn Wright	R/V <i>Melville</i>
BMRG09MV	1996	SeaBeam 2000	SIO	Peter Lonsdale	R/V <i>Melville</i>
KIWI05RR	1997	SeaBeam 2100	SIO	Stephen Miller	R/V <i>Revelle</i>
AVON02MV	1999	SeaBeam 2000	SIO	Hubert Staudigel	R/V <i>Melville</i>
AVON03MV	1999	SeaBeam 2000	WHOI	Stanley Hart	R/V <i>Melville</i>
COOK15MV	2001	SeaBeam 2000	URI	Roger Larson	R/V <i>Melville</i>
DRFT09RR	2002	Simrad EM120	SIO	Eric Terrill	R/V <i>Revelle</i>
DRFT10RR	2002	Simrad EM120	USF	Dave Naar/Dawn Wright	R/V <i>Revelle</i>
DRFT11RR	2002	Simrad EM120	SIO	Stephen Miller	R/V <i>Revelle</i>
N/A	2004	Reson 8101ER	PIFSC	Joyce Miller	R/V <i>AHI</i>
KM0505	2005	Simrad EM120	UHMC	Transit	R/V <i>Kilo Moana</i>
KM0506	2005	Simrad EM120	WHOI	Stanley Hart	R/V <i>Kilo Moana</i>
KOK0510	2005	SeaBeam 210	HURL	Dawn Wright	R/V <i>Ka'imikai-O-Kanaloa</i>
KOK0511	2006	SeaBeam 210	HURL	John Smith	R/V <i>Ka'imikai-O-Kanaloa</i>

The primary port and capital of American Samoa, Pago Pago, often serves as a stopover for research cruises operating in the southwest Pacific. Multibeam systems remain in operation as vessels en route to nearby study areas make for port or sea. Though often only revealing slivers of the seafloor, these surveys offered the first glimpses of the underlying bathymetry in the ESVP. This was the case for the R/V *Thomas Washington* as it hosted expeditions in the mid 1980's to investigate tectonics regimes in the Lau Basin (SIOExplorer 2007). Between 1984 and

2005, a total of 14 transits aboard the R/V *Thomas Washington*, R/V *Melville*, and R/V *Revelle*, surveyed swaths of the ESVP (Wright 2002; Wright et al. 2002; Smith et al. 2006; SIOExplorer 2007).

3.5 Multibeam Compilation

Raw multibeam data from disparate sources require an assortment of post-processing procedures before a compiled bathymetric map can be produced. MB-System, written by Caress and Chayes (1996), is an open-source program designed to manipulate and compile raw multibeam files that exist in a variety of data formats. The acquired raw multibeam files were generated by systems ranging from the original SeaBeam to advanced systems like the Simrad EM120, making MB-System a crucial tool in this compilation effort. Just as data formats vary, so too do the spatial resolution capabilities of each multibeam system. This is a limiting factor when considering a regional bathymetric compilation. To achieve spatial coherence throughout the compilation, the maximum resolution is defined by the least sophisticated multibeam system. MB-System is capable of gridding raw multibeam files at user-defined resolutions, further underscoring its suitability for this task.

The process of compilation is best described in a stepwise manner, which is outlined here and explained in greater technical detail in **Appendix A**.

- Creation of a datalist containing every raw multibeam file to be included in the compilation. This datalist also includes a designation for each data format.
- Determination of the maximum regional spatial resolution. After visual experimentation with an original SeaBeam (data format 16) raw multibeam file, a grid cell size of 200 meters was selected.
- Determination of edge smoothing using spline interpolation. Again, based on visual experimentation, each raw multibeam file was extended by one grid cell to smooth edges of the compilation (Lundblad 2004).
- Definition of the spatial range. This compilation is limited to the ESVP. Rose Atoll is also included in the interest of setting it apart from the other islands of American Samoa based on its geomorphology. The compilation is bounded by 169°W, 167°30'W, 13°12'S, and 15°30'S.

3.6 Cartography

The merged product is a Generic Mapping Tools (GMT) grid, a highly flexible format which can be exported to various programs for simple plotting or advanced visualization (Wessel and Smith 1991). Aside from its native command line environment, the grid format is also compatible with the open-source program Mirone (Luis 2007) and the commercially available Fledermaus. In this study, Mirone was practical for quick previews and cursory analyses of GMT grids. Fledermaus is a high-end software package capable of advanced analyses and visualization. All maps of the ESVP were created using the hillshade and color ramp features in Fledermaus (**Foldout Maps**). For visual continuity, a grid of 1 km bathymetry derived from satellite altimetry (Sandwell and Smith 1997) was used as a backdrop. All additional adornment was added using Adobe Photoshop and Illustrator.

4. Seamount Morphology

4.1 Seamount Formation and Anatomy

Seamounts are the surface expressions of previous or current volcanic effusion from magma chambers located in the upper mantle. The submarine equivalent of subaerial volcanoes, seamounts develop upon oceanic crust in several distinct settings. Most are formed at plate boundaries, either during crustal accretion at seafloor spreading centers or along volcanic arcs at ocean-to-ocean plate convergent zones. The remaining contingent originates away from plate boundaries, in the intraplate (Hekinian et al. 2004). While in close proximity to the Tonga Trench subduction zone, the ESVP is situated on the subducting Pacific plate, opposite the Tonga volcanic arc. Vailulu'u is one of just five known active intraplate volcanic centers anchoring hotspot trails in the Pacific, along with Teahitia and Mehetia in the Society chain, MacDonald in the Austral chain, Bounty in the Pitcairn, and Hawaii (Binard et al. 2004).

Seamount morphology is controlled by the style of eruption. Eruptive style is in turn controlled by the composition of lava and physical properties such as the cooling rate, size of the eruptive conduit, and ratio of melt to crystal (Bonatti and Harrison 1988). There are two general types of eruptive styles for seamounts; quiet and explosive (Binard et al. 2004). A quiet eruption is characterized by the effusion of low viscosity (low-silica content) lavas resulting in forms such as lobate pillow lavas and expansive sheet flows. Seamounts exhibiting “quiet morphologies”

have a MORB-type geochemical signature and are usually produced at spreading centers. An explosive eruption is driven by the presence of volatile elements (e.g. H₂O, CO₂) in magmas. The building of gas pressure in magma chambers results in violent eruptions that produce corrugated and disjointed surfaces. Intraplate seamounts observed through submersible dives and deep-towed cameras in the Society, Austral, and Pitcairn hotspot chains are typified by highly vesicular basalts (indicative of past volatile enrichment) and “explosive morphologies.”

As observed in the Society, Austral, and Pitcairn chains, the formation of a typical intraplate seamount occurs in three successive stages (Binard et al. 1992) (**Figure 11**). The first is a period of high lava discharge, often effusive, which establishes the seamount base. These massive flows are sustained by large reservoirs exuding relatively hot and viscous magma. Following the initial sheet flow from a centralized conduit, eruptive venting disperses along preferential rift zones and construction of the seamount flank begins. In quiet eruptions, flanks are characterized by pillows and lava tunnels, whereas explosive eruptions give rise to pyroclastic deposits and talus. Contingent upon magma supply, flank-building may continue until the summit reaches shallow depths (< 500 m below sea level), at which point seawater reacts with lava to produce steam. Subsequent hydromagmatic explosions result in the creation of a summit crater. This energetic environment incites the dispersal of volcanic ejecta, sometimes coming to rest on flanks some 1000 m below (Binard et al. 2004).

Intraplate volcanism may produce a single seamount or a cluster of variably sized seamounts (Binard et al. 2004). Clusters are produced when rift zones are extended by dike propagation within the oceanic crust (Rubin and Pollard 1987) (**Figure 12**). Dikes branch out laterally from a primary magma reservoir as feeder channels for secondary cones that form on the flank, at the base, or up 50 km away from large seamounts (Binard et al. 2004). Dike propagation is a function of structural vulnerabilities in the oceanic crust. The cause of these structural inconsistencies is a point of debate. Hypotheses include the tectonic reactivation of ancient faults and fracture zones in the crustal fabric (Binard et al. 2004), reheating of the lithosphere by the ascending mantle plume that create weaknesses (Detrick and Crough 1978), or a combination of these factors. Once established, dikes can supply magma to secondary cones as the increasing load of the large seamount compresses the primary reservoir and pushes magma out laterally.

4.2 Quantitative Studies

Quantitative studies of seamount morphology have aimed to infer the mode of formation through analyses of shape and distribution statistics. Jordan et al. (1983) first probed this possibility in their study of seamounts in the eastern Pacific. Menard (1964) defines a seamount as “a more or less isolated elevation of the sea floor with a circular or elliptical plan, at least 1 km of relief, comparatively steep slopes, and relatively small summit area.” Jordan et al. (1983) consider the 1 km cutoff a “cartographic convention inappropriate as a generic definition” and therefore include smaller seamounts to define their model. To estimate shape, Jordan et al. (1983) approximate a seamount as a “truncated right-circular cone of constant slope” and parameterize shape using height, basal and summit radius, slope, height-to-basal-radius ratio, and flatness (summit radius/basal diameter). The integration of these parameters into a distribution model will be discussed in **Chapter 5**.

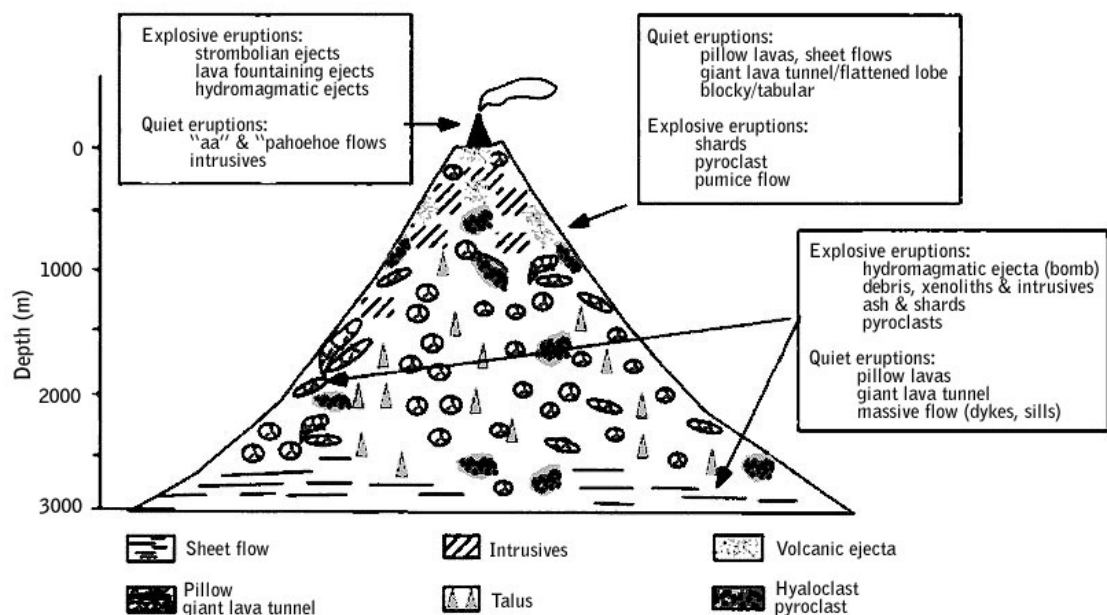


Figure 11: Diagram of typical seamount anatomy (Binard et al. 1992).

Smith (1988) applies these shape parameters to 70 seamounts located throughout the Pacific. Based on the flatness factor, she classifies seamount shape into two categories; conical (< 0.25 flatness) and truncated (> 0.25 flatness) (**Figure 13**). Conical seamounts are common in intraplate settings with heights ranging from very small (< 500 m) to large (> 1000 m). Few truncated seamounts are found in these areas, and those present are likely inherited from

seamount production at the East Pacific Rise (EPR). Quiet eruptions of MORB-type basalts at spreading centers manifest as small to medium-sized truncated seamounts. Regardless of origin, large seamounts are typically the most conical, suggesting this shape becomes preferential as edification continues. Smith (1988) also finds that summit height and basal radius are highly correlatable, whereas summit height and summit radius show little correlation. A principle components analysis reveals that of five shape parameters (summit height, basal radius, summit radius, flatness, and slope), summit height and flatness account for most of the variance in seamount shape. Subsequent studies have borne out the general relationships of shape parameters observed by Smith (1988) (Abers et al. 1988; Smith and Cann 1990, 1992; Bemis and Smith 1993; Kleinrock and Brooks 1994; Scheirer and MacDonald 1995; Shierer et al. 1996; Rappaport et al. 1997; Jaroslow et al. 2000).

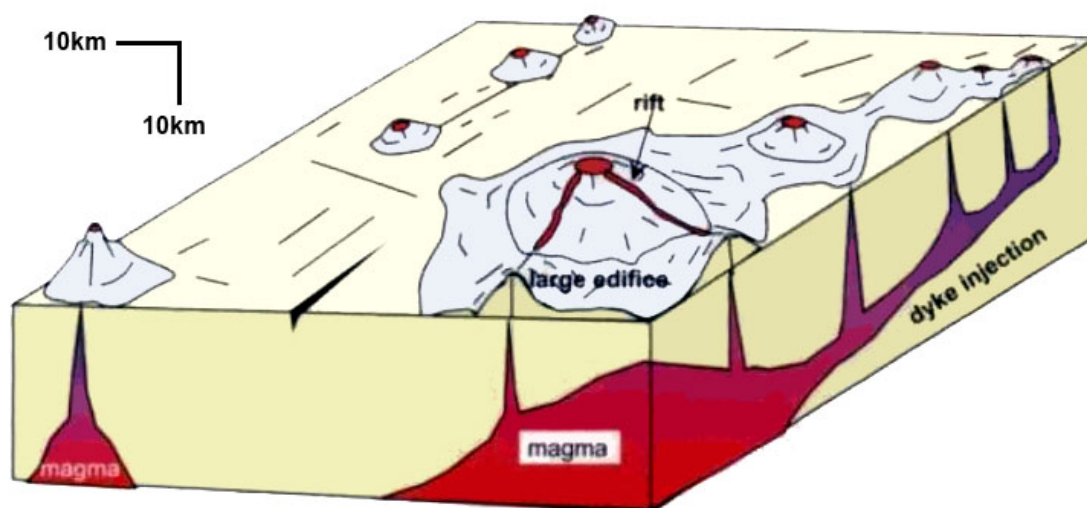


Figure 12: Schematic of primary magma reservoir and radiating dike injections (Binard et al. 2004).

4.3 Seamount Identification and Shape Parameters

Using the work of Jordan et al. (1983) and Smith (1988) as a foundation, candidate seamounts in the ESVP are indentified for shape analysis. The ESVP is the site of numerous small seamounts (< 1000 m in height) and approximately twelve large seamounts, guyots, and breaching islands. The large seamounts will not be considered in this quantitative analysis, as their morphologies are far too complex for satisfactory treatment within the framework of this methodology. Large seamounts are deconstructed qualitatively in **Chapter 6**.

Due to time expense and possible inconsistencies in the visual identification of small seamounts from a contoured bathymetric map, an alternative method was elected. After importing the ESVP multibeam compilation grid to Fledermaus, a slope surface was calculated (**Foldout Map 3**). Creation of a custom color ramp provides a visual circumscription of slope break for each seamount (see **Appendix A** for technical notes). Only seamounts with clear circumscription were included. This excludes several features that are located on the flanks of large seamounts. In all, 51 seamounts are identified (**Foldout Map 4**).

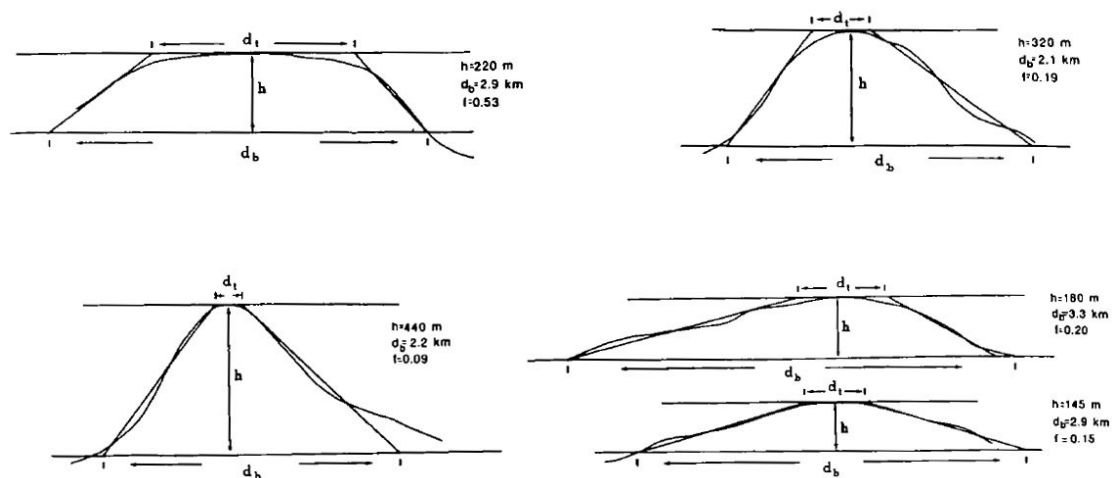


Figure 13: Hand-drawn illustrations demonstrating the method of seamount shape estimation employed by Smith (1988). h is height, d_t is summit diameter, d_b is basal diameter, and f is the factor of flatness.

Seamount shape is approximated as a conical frustum (**Figure 14**). This differs from the truncated right-circular cone used by Jordan et al. (1983) in that the base and summit areas are elliptical rather than circular. This shape also allows for the estimation of elongation, and more precise measurements of basal area and overall seamount volume (Rappaport et al. 1997). Measurement of seamount parameters is performed using the Fledermaus profiling tool (**Figure 15**). Two cross-sections are taken for each seamount to account for both the major and minor axes of the basal ellipse. From these cross-sections values for seven *primary* shape parameters are estimated: (1) basal axis diameter, (2) summit axis diameter, (3) slope of left flank, (4) slope of right flank, (5) basal depth, and (6) summit depth, and (7) azimuth (No-180°E) of the major basal axis. From these primary parameters seven *secondary* parameters are calculated: (1) basal

area, (2) summit area, (3) average height, (4) average slope, (5) flatness, (6) basal elongation, and (7) volume. Summary statistics are listed in **Table 2**. See **Appendix B** for a complete table of parameter values for each seamount and the equations used to derive secondary parameters.

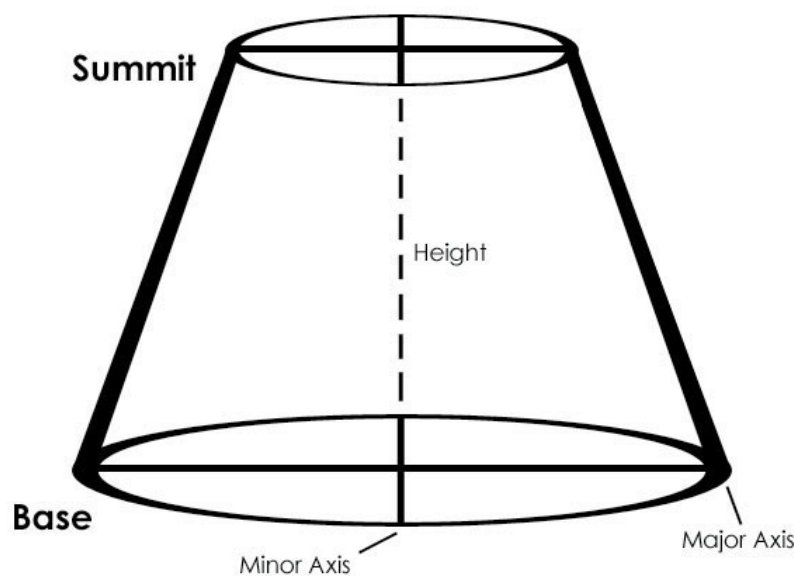


Figure 14: “Conical frustum” used to approximate seamount shape.

Table 2: Summary of shape statistics. Mean is expressed with a confidence interval of 95%.

-----	Mean	Std. Dev.	Minimum	Maximum	Total
Basal Area (km²)	6.67 ± 1.53	5.58	1.71	36.52	340.51
Summit Area (km²)	0.090 ± 0.078	0.283	0.004	2.049	4.584
Height (m)	325 ± 41	152	105	850	N/A
Slope (%)	13.4 ± 1.0	3.5	5.9	20.1	N/A
Basal Depth (mbsl)	-4208 ± 199	727	-2640	-5205	N/A
Flatness	0.012 ± 0.004	0.0161	0.0014	0.1021	N/A
Elongation	1.28 ± 0.07	0.24	1.00	2.10	N/A
Volume (km³)	1.01 ± 0.43	1.58	0.09	10.76	51.38

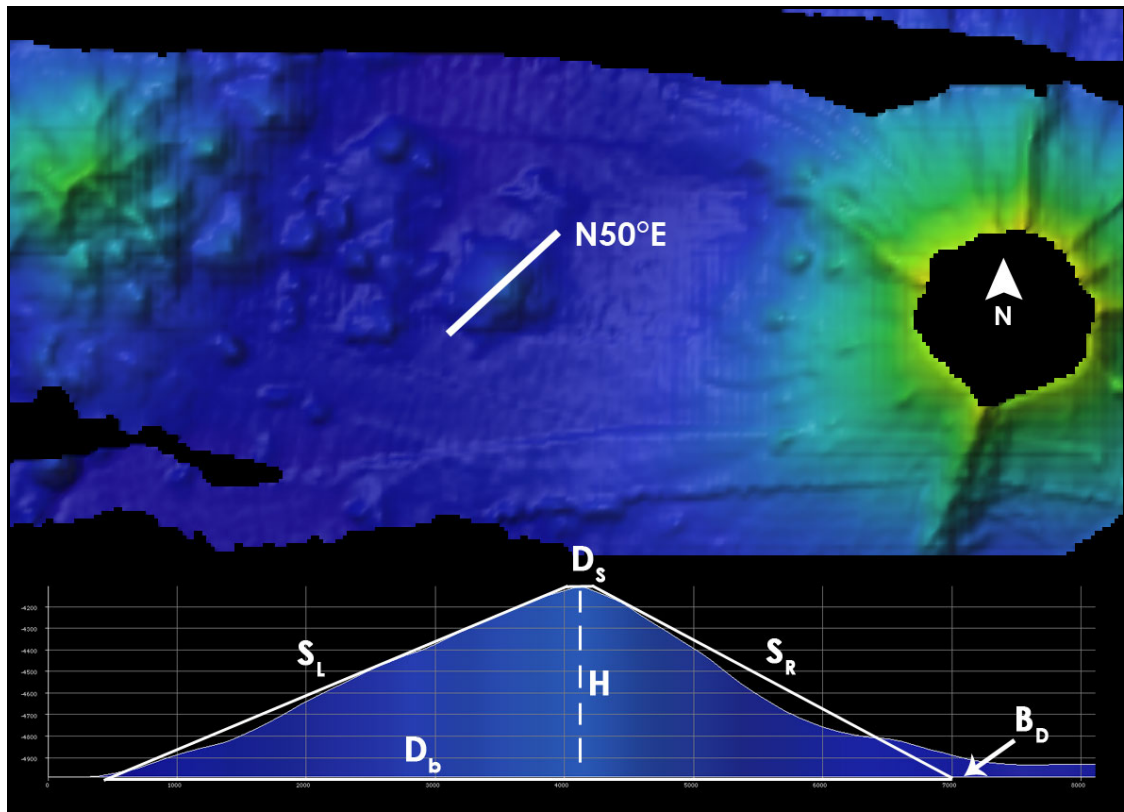


Figure 15: The Fledermaus profiling tool is used to characterize seamount shape, where D_s is summit diameter, D_b is basal diameter, S_L is slope of the left flank, S_R is slope of the right flank, B_D is basal depth, H is height, and $N50^\circ E$ is the azimuth.

4.4 Observed Relationships

Smith (1988) has established several hypotheses regarding the relationship of shape parameters. Shape parameters measured in the present study are tested against these hypotheses. Several additional relationships are observed based on shape parameters not calculated in the Smith study. These parameters include basal depth, elongation, azimuth of the major basal axis, and volume. The relationships illustrated in **Figures 16-21** are considered the most significant, but are not exhaustive.

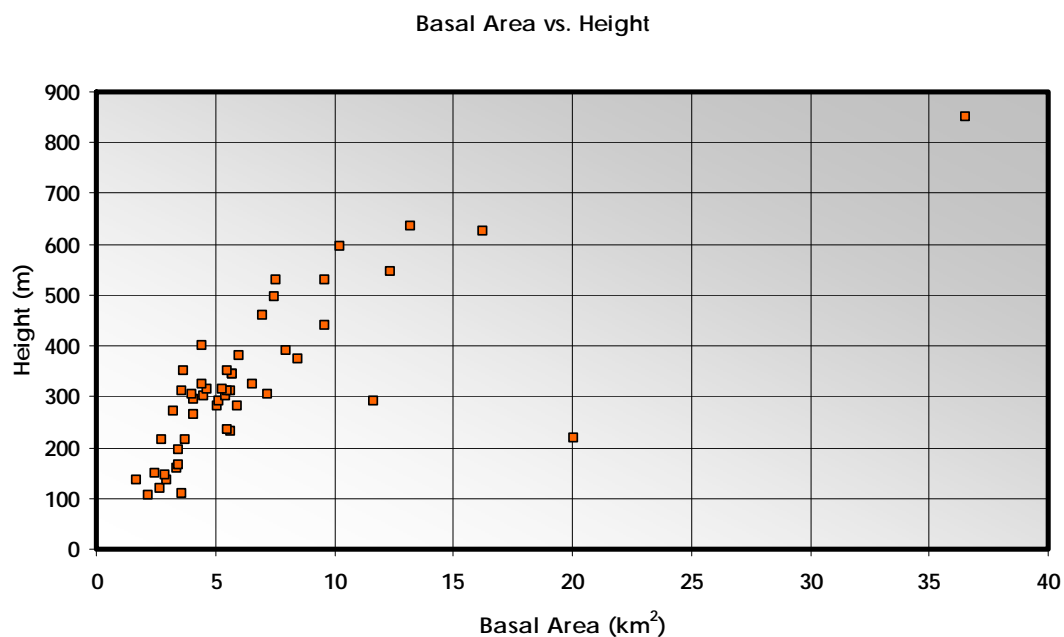


Figure 16: Shape Parameter Relationship: Basal Area vs. Height. As observed by Smith (1988), basal attributes and height demonstrate a strong positive relationship. Height is represented by the secondary parameter average height in this study. Height is calculated for both major and minor cross-sections by subtracting basal depth from summit depth. Due to directional slope gradients, these depths are not always identical for both cross-sections, necessitating an average. To better represent basal characteristics, basal area is used instead of basal radius in the present study. It seems intuitive that taller seamounts would require a larger base for support. Less conspicuous is the demonstration of the paucity of truncated seamounts. There is one obvious outlier, a seamount located at 14.43°S, 169.76°W, south of Ofu, appearing to have been formed from an effusive lobate flow. There are several similarly shaped features nearby, though none of them were properly circumscribed by slope break.

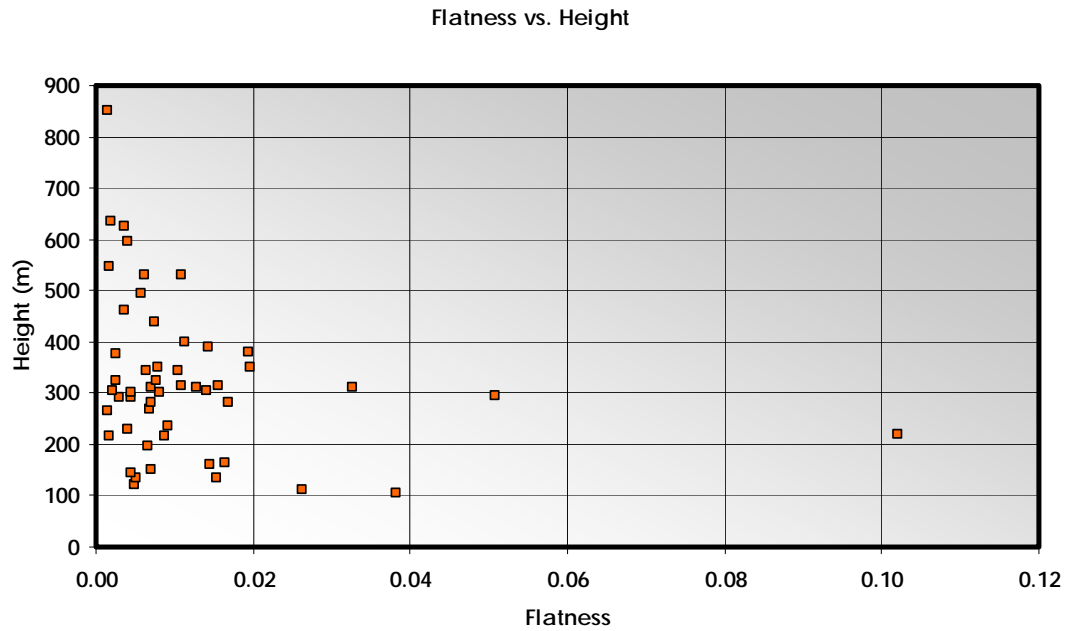


Figure 17: Shape Parameter Relationship: Flatness vs. Height. The relationship of flatness and height illustrated by Smith (1988) is supported here. Flatness has been calculated using a slightly different method in this study. Rather than the ratio of summit radius to basal radius, flatness is estimated as the ratio of summit area to basal area. This allows for inclusion of both major and minor cross-sections in the calculation of flatness. As height increases, flatness decreases. However, below heights of approximately 400 m, flatness is highly variable.

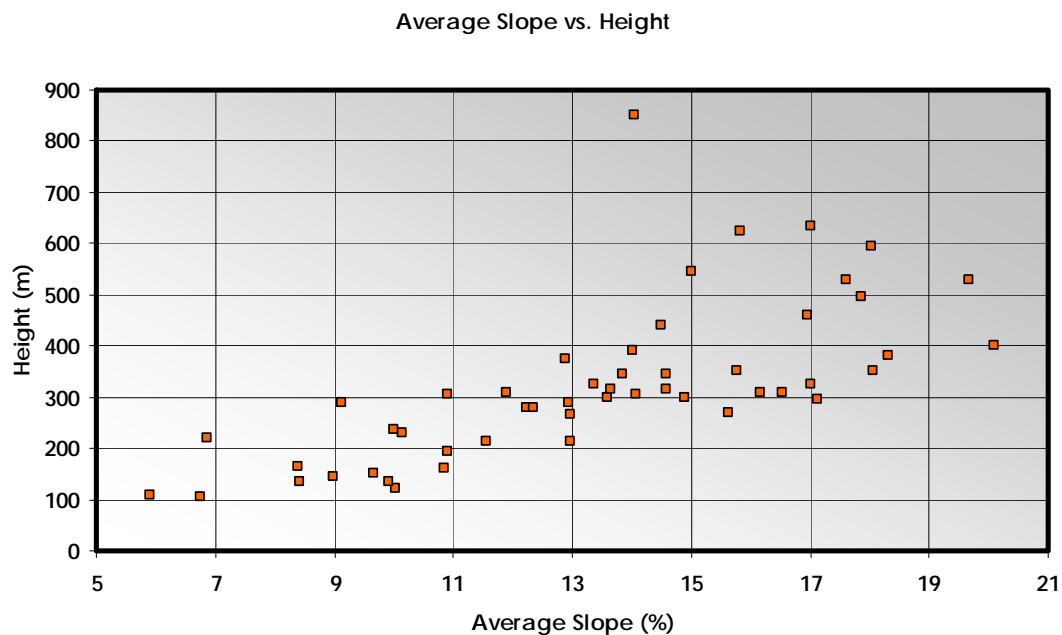


Figure 18: Shape Parameter Relationship: Slope vs. Height. Smith (1988) samples seamounts with heights ranging from 140 m to 3,800 m. Two groups arise when height is plotted against slope. First is a group of tall seamounts (> 2,600 m) that cluster near their mean slope of 15%. The second group of smaller seamounts (< 1,800 m) shows a diffuse but slightly positive relationship between slope and height. In the present study slope is an average of four values; slope of left flank and slope of right flank for both major and minor cross-sections. A relationship similar to the latter group is observed. This is expected since no seamounts sampled here are taller than 850 m.

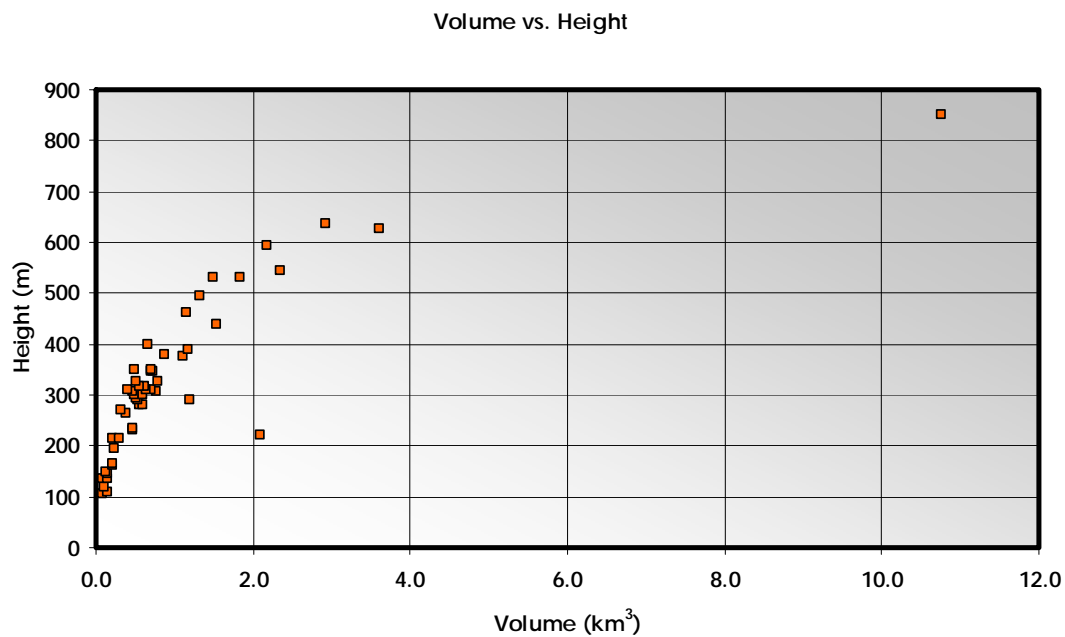


Figure 19: Shape Parameter Relationship: Volume vs. Height. Akin to the relationship between basal area and height, volume and height demonstrate a positive relationship, though not as strong. The same outlier observed in the basal area vs. height relationship reveals itself, accounting for a volume of 2.09 km³ at a height of just 220 m.

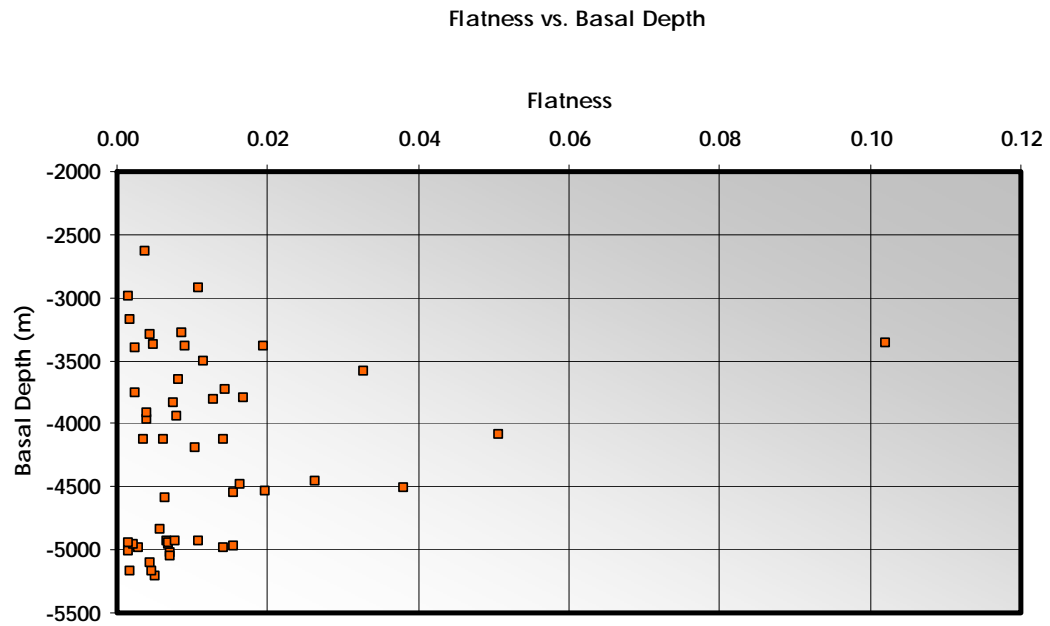


Figure 20: Shape Parameter Relationship: Flatness vs. Basal Depth. Flatness and basal depth demonstrate a potentially revealing relationship. The flattest seamounts appear to occur at intermediate basal depths. All of these flat seamounts occur near the large seamount of Papatua. It seems possible that this relationship constrains the depth range of a somewhat low-viscosity magma source on the flanks of Papatua.

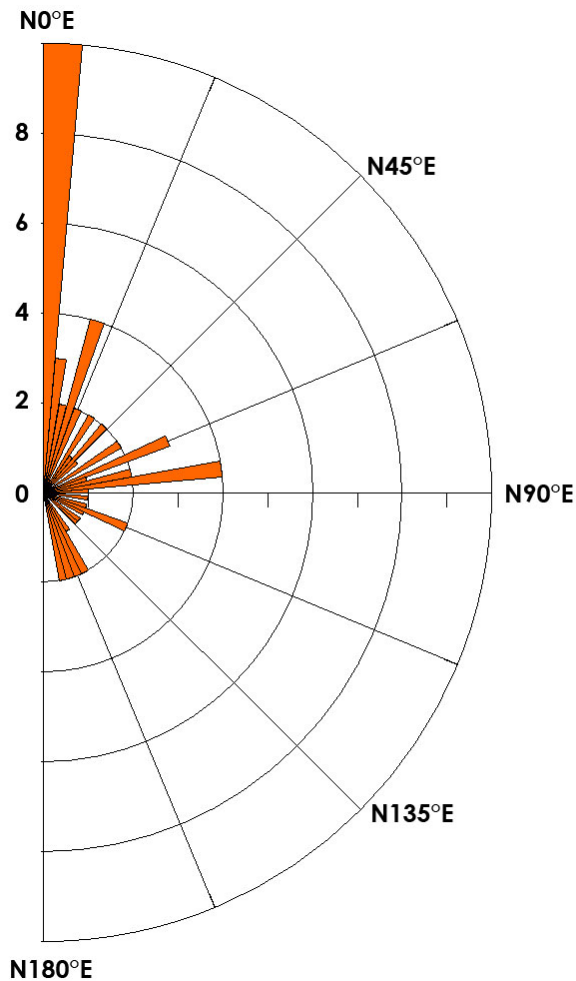


Figure 21: Rose Diagram of Major Basal Axis Azimuth. Though there is a generally diffuse distribution in the azimuth of the major basal axis, a somewhat dense cluster ranges from 0° to 20° E. This is indicative of preferential distributions along rift zones trending in a variety of directions. Rift zones are mapped in detail in **Chapter 6**.

5. Seamount Distribution

5.1 Geologic Controls on Distribution

Distribution of seamounts in intraplate hotspot settings is little understood. Processes controlling the local distribution of small satellite seamounts about a large volcanic center may differ from those giving rise to small seamounts outside of a 50 km radius. From observations of Pacific hotspots, Binard et al. (2004) suggest these more isolated seamounts are fed by magma sources deeper in the lithosphere. They expand on this by proposing these small seamounts “could be supplied from the replenished and differentiated magma reservoirs located underneath the larger edifices when the magma flows through pre-existing conduits or channels

within a fractured lithosphere.” As with more shallow, localized distributions, this framework evokes a preferential directionality along channels. However, unlike in local reactivation of the crust, deep fracture zones in the lithosphere are not necessarily inherited ancient structures, particularly in the case of the ESVP, where its western-most portions lie within a lithospheric stress field (Abbott and Fisk 1986; Wright and White 1987).

Just as structural deficiencies are inherited from ancient oceanic crust, so too are seamounts transported by plate motion. On a broad scale, the distribution of intraplate seamounts is a function of crustal age and plate velocity (Batiza 1982). In his study of seamount abundances in the Pacific, Batiza (1982) observes that the presence of small seamounts decreases with crustal age and credits this trend to sediment burial. The abundance of large seamounts, on the other hand, increases with crustal age. To explain this increase, Batiza (1982) cites the work of Vogt (1974) in which seamount height is believed to be ultimately dependent upon lithospheric thickness. Lithospheric thickness increases with age, and as thickness increases there is an isostatic response. The implications of these studies for seamount distribution in the ESVP are unclear, considering the dominance of recent volcanic activity in the region. The ESVP rests upon relatively old oceanic crust (> 100 Ma) with substantial sediment deposition. Though one may fathom the transport of ancient seamounts, there are none such candidates demonstrating an advanced state of erosion or the requisite size.

5.2 The Exponential Distribution Model

Inspired by the early work of Menard (1959) in the statistical analysis of seamounts, Jordan et al. (1983) formulate a predictive model to estimate the areal distribution seamounts across the seafloor. Based on wide-beam sounding data collected in the southeast Pacific, they find that seamount size distribution is nearly exponential over a broad range of sizes. Parameterization of this relationship constitutes the fundamental formula for an exponential distribution model of seamount size. The model is first used to predict the “characteristic radius” of the southeast Pacific seamount population. Smith and Jordan (1988) later opt to use height as the dependent shape parameter and therefore define the equation

$$v(H) = v_0 \exp(-\beta H)$$

where $\mathbf{v}(\mathbf{H})$ is the number of seamounts per unit area with a height greater than or equal to \mathbf{H} , \mathbf{v}_o is the total number of seamounts per unit area, and $\mathbf{\beta}$ is the negative of the slope of the line fitting $\ln(\mathbf{v}(\mathbf{H}))$ against \mathbf{H} . The “characteristic height” of the seamount sample is then equal to the negative reciprocal of $\mathbf{\beta}$.

5.3 Application of Model and Results

Following the procedure employed by Smith and Jordan (1988), the exponential distribution model is applied to small seamounts in the ESVP. To define an appropriate sample range, seamounts are placed into bins representing 100 m intervals of height (**Figure 22**). In this instance, height corresponds to the secondary shape parameter of average height for each seamount. Smith and Jordan (1988) include bins with as few as five seamounts in their study of nearly 4,500 Pacific seamounts. Due to a much smaller dataset and narrower range of heights, bins with as few as three seamounts have been included for the present study. Only three seamounts are excluded, leaving 48 seamounts for distribution analysis.

Small seamounts are considered separately from large seamounts in this study. Therefore, to most accurately estimate their distribution across the seafloor, the total areal extent must be limited to space not occupied by large seamounts. This is accomplished by subtracting the area of large seamounts as delineated in **Foldout Map 5**. The area of the entire compilation is 28,446 km². Excluding large seamounts, the area is reduced to 21,158 km².

A series of values are calculated using the average height parameter for each seamount in relation to the areal extent of 21,158 km². This yields two significant values

$$\mathbf{v}_o = 2.8 \pm 0.2$$

$$\mathbf{\beta}^{-1} = 139 \text{ m}$$

where \mathbf{v}_o is the total number of predicted seamounts per 1,000 km² in the ESVP and $\mathbf{\beta}$ is the characteristic height of seamounts in the EVSP (**Figure 23**). Standard error for \mathbf{v}_o is expressed at the upper and lower 95% confidence limits. See **Appendix C** for a complete table of calculations and other technical notes on the application of this distribution model.

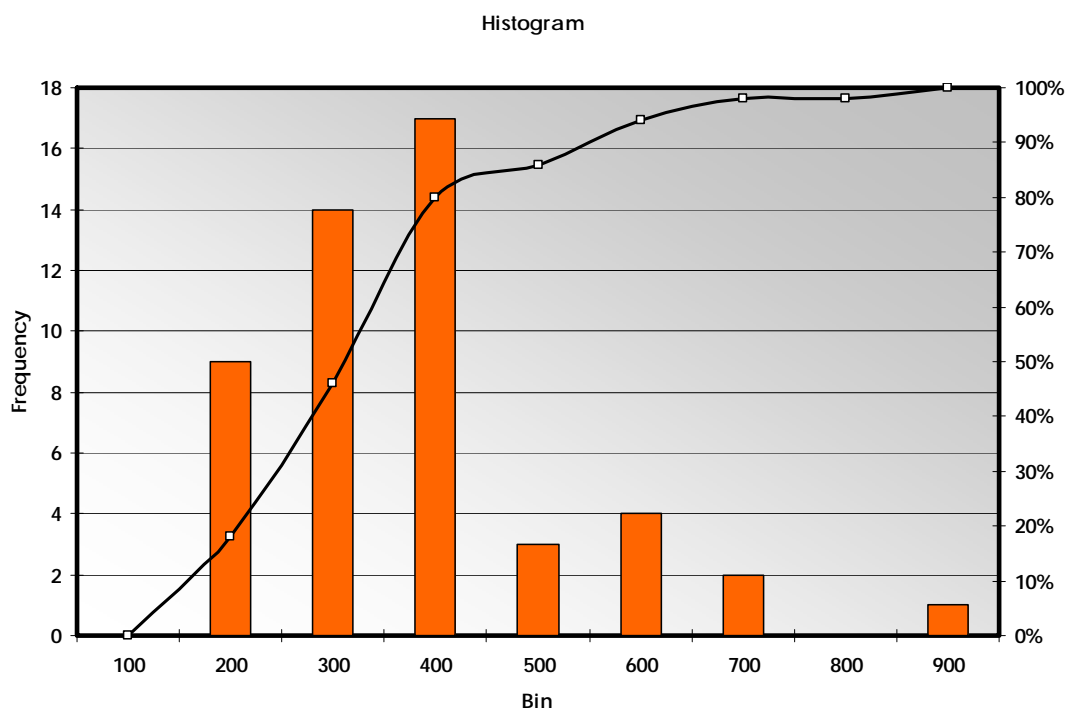


Figure 22: Bins and Cumulative Percentage Plot. A skewed distribution of heights illustrates the suitability of an exponential model.

5.4 Discussion

In addition to the original work of Smith and Jordan (1988), nine studies of seamount size distribution have been undertaken (**Table 3; Figure 24**). However, such an analysis has never before been performed for seamounts located in a region of mantle plume activity. Provided the possibility of preferential distribution of small seamounts along reactivated faults and deep fracture zones, the assumption of a random distribution may not be met. This comes as a caution when comparing distribution and characteristic height values across studies. Nevertheless, some valuable insight can be gleaned about the variety of environments in which seamounts are formed and persist.

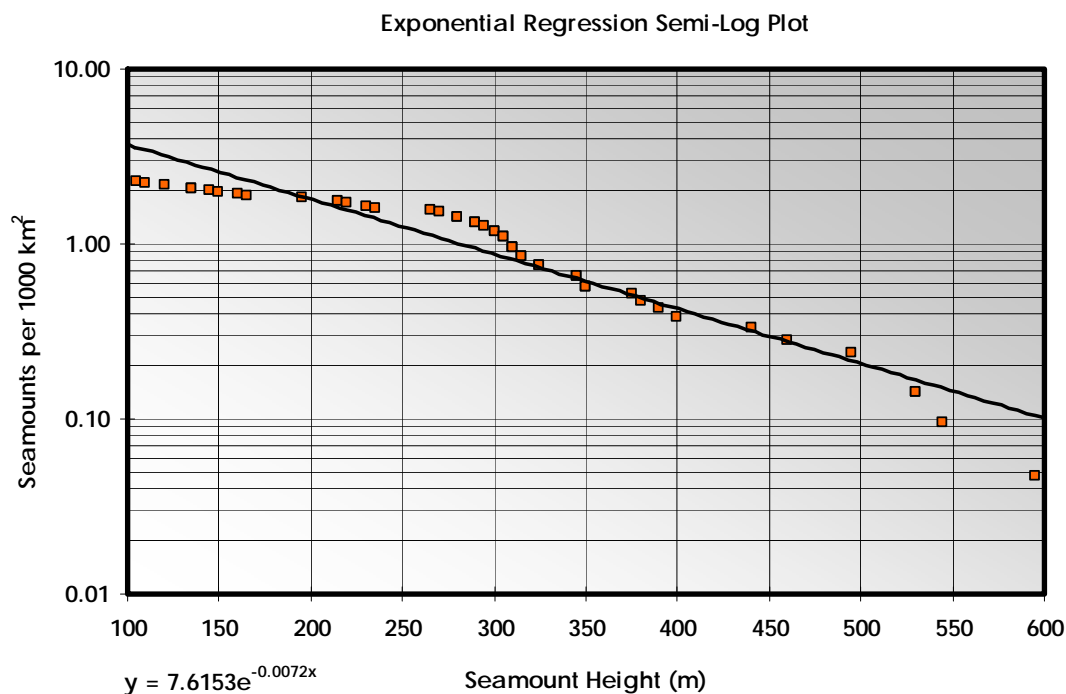


Figure 23: Semi-Log Plot of Exponential Regression Fit. Curve of exponential fit transposed over cumulative observed height values.

The work of Smith and Jordan (1988) is vast in comparison to subsequent studies of seamount distribution. 157,000 km of wide-beam profiling is complemented by 38,000 km² of multibeam coverage to sample heights for approximately 4,500 seamounts throughout the Pacific. Seamounts are grouped into eight regions for which areal distribution and characteristic height are calculated separately. This study differs from other distribution analyses in that sampled seamounts are distributed throughout the Pacific and show a wide range of heights (400 to 2,500 m). Application of the exponential distribution model yields an aggregate seamount density of 5.4 per 1,000 km² and a characteristic height of 347 m.

The following nine studies operate with narrower height ranges and focused study areas, also diagnostic of the present study. All characteristic heights fall near the bottom or just below the observed range minimum, as expected with an exponential distribution. With respect to seamount density, studies in the Pacific and Atlantic oceans are clearly distinguishable. Studies along the Mid-Atlantic Ridge (MAR) reveal very high densities, ranging from 58 to 310 seamounts per 1,000 km², while studies along the EPR and in the Pacific intraplate show a range from 1.9 to 13.3 seamounts per 1,000 km². The work of Kleinrock and Brooks (1994) in the

Galapagos triple-junction region produces an anomalous density (370 seamounts in per 1,000 km²) in stark contrast with other densities in the Pacific. This incongruity is probably due to the complex structure and spreading rate (slower than at the EPR) of the Galapagos propagator system. The broader distinction between the Pacific and Atlantic oceans is not one accounted for on the basis of tectonic scheme, as the majority of studies in each ocean were focused on spreading ridges. Smith and Cann (1992) contend that these differences are the result of “low magma flux and greater depth of hydrothermal circulation” at the MAR. In essence, seamount production at mid-ocean ridges is controlled by the spreading rate, though somewhat counterintuitively, as fewer and larger seamounts are produced at fast spreading ridges.

Table 3: Studies of seamount distribution. *ID* corresponds to locations on *Figure #*. v_o is seamount density. β^1 is characteristic height.

ID	Year	Study	Region (Latitude)	H Range (m)	v_o (per 10 ³ km ²)	β^1 (m)
1	1988	Smith & Jordan	Eastern Pacific (23°-33°N)	400 – 2000	6.8 ± 2.1	389
2	1988	Smith & Jordan	Eastern Pacific (33°-40°N)	400 – 1400	1.7 ± 0.7	325
3	1988	Smith & Jordan	Northern EPR (3°-18°S)	400 – 1200	7.9 ± 2.9	453
4	1988	Smith & Jordan	Southwest Pacific (23°-38°S)	400 – 2500	5.8 ± 0.8	298
5	1988	Smith & Jordan	Southern EPR (42°-54°S)	400 – 1300	4.1 ± 1.3	324
6	1988	Smith & Jordan	Southern EPR (38°-56°S)	400 – 2000	3.3 ± 0.9	316
7	1988	Smith & Jordan	Southern Pacific (55°-64°S)	400 – 1500	13.3 ± 5.2	439
8	1988	Smith & Jordan	Southwest Pacific (45°-60°S)	400 – 1100	13.1 ± 5.6	405
9	1988	Abers et al.	Southern Pacific (7°-22°S)	100 – 1000	12.6 ± 0.8	174
10	1992	Smith & Cann	MAR (24°-30°S)	50 – 210	195 ± 9	58
11	1993	Bemis & Smith	Southern Pacific (9°-22°S)	300 – 700	13 ± 2	233
12	1994	Kleinrock & Brooks	Galapagos (1°-3°N)	50 – 350	370 ± 30	29
13	1995	Schierer & MacDonald	Northern EPR (8°-17°N)	200 – 800	1.9 ± 0.2	240
14	1995	Magde & Smith	Northern MAR (57°-62°N)	50 – 250	310 ± 20	68
15	1996	Schierer et al.	Southern EPR (15°-19°S)	200 – 1200	4.8 ± 0.2	421
16	1997	Rappaport et al.	Easter Chain (27°-29°S)	200 – 1000	2.7 ± 1.5	308
17	2000	Jaroslow et al.	MAR (25°-27°N)	70 – 350	58.3 ± 1.6	92
*	2007	This Study	EVSP (13°-15°S)	100 – 600	2.8 ± 0.2	139

In general, the results of the present study compare well with others conducted in the Pacific intraplate and along the EPR (Smith and Jordan 1988; Abers et al. 1988; Bemis and Smith 1993; Schierer and MacDonald 1995; Schierer et al. 1996; Rappaport et al. 1997). From a more nuanced perspective, a density of 2.8 seamounts per 1,000 km² in the ESVP is in best agreement with

densities along the EPR and Smith and Jordan areas 1 through 6 (1.9 to 7.9 seamounts per 1,000 km²). Densities in the southern Pacific are somewhat higher (12.6 to 13.3 seamounts per 1,000 km²). Area 4 of the Smith and Jordan study, the Southwest Pacific Basin between 23°-38°S, is in closest proximity and demonstrates a density roughly double that in the ESVP (5.8 seamounts

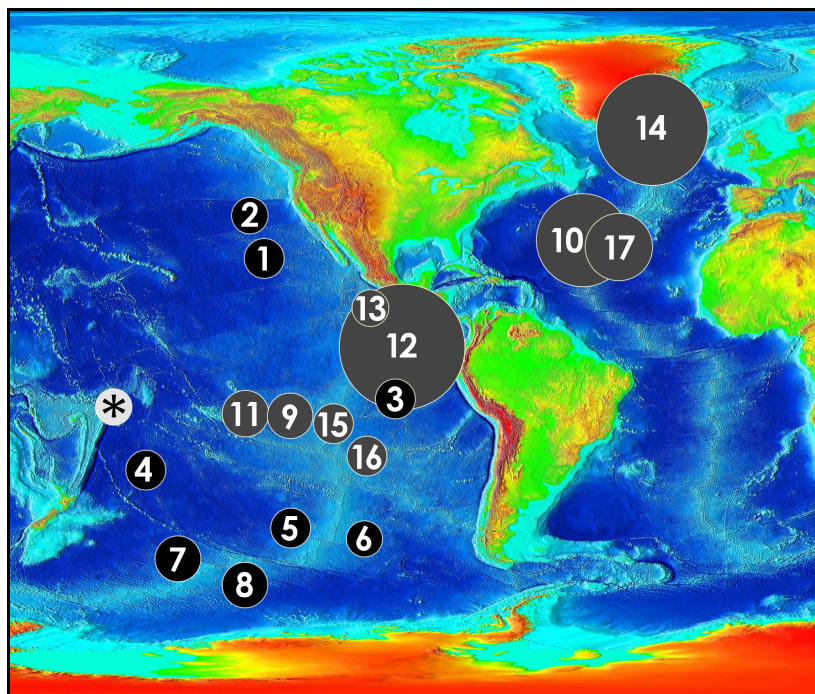


Figure 24: Locations of seamount density studies listed in **Table 3**. Numbers correspond to *ID* in **Table 3**. Circle size indicates density magnitude. Black circles represent Smith and Jordan (1988). Gray circles represent subsequent studies. Image modified from Sandwell and Smith (1997).

per 1,000 km²). This divergence should not be considered extraordinary however, as there is notable regional variation demonstrated by Smith and Jordan (1988), even between adjacent study areas. The most pronounced variation is along the Eltanin fracture zone in the south Pacific which separates areas 5 and 6 (4.1 and 3.3 seamounts per 1,000 km², respectively) from 7 and 8 (13.3 and 13.1 seamounts per 1,000 km², respectively). Smith and Jordan (1988) attribute this discrepancy to an increase in mantle temperature moving from south to north across the Eltanin fracture zone (Cochran 1986). They note a reduction in seamount abundance in this direction is “inconsistent with the notion that hotter mantle produces more seamounts.” Though the ESVP is observed as a site of mantle plume interaction, this rationality would not apply since the interaction observed in the south Pacific manifests as a mid-ocean ridge, not a hotspot. Until the exponential distribution model is applied to another area of hotspot volcanism, regional variation with the respect to seamount density remains unclear.

per 1,000 km²). This divergence should not be considered extraordinary however, as there is notable regional variation demonstrated by Smith and Jordan (1988), even between adjacent study areas. The most pronounced variation is along the Eltanin fracture zone in the south Pacific which separates areas 5 and 6 (4.1 and 3.3 seamounts per 1,000 km², respectively) from 7 and 8 (13.3 and

6. Geomorphologic Interpretation

6.1 Tutuila

The large seamounts, guyots, and breaching islands of the ESVP demonstrate complex eruptive patterns. Perhaps the most intricate is the Tutuila complex, composed of five separate volcanic centers (Stearns 1944), and representing the largest structure in the ESVP with a volume of 4,957 km³ (Earthref.org 2007). Tutuila is unique with its highly elongate primary rift zone that trends N70°E (Stearns 1944). *En echelon* lineaments both to its east and west demonstrate a primary rift zone trending N110°E. Tutuila therefore marks an interruption in the dominant rifting directions. Walker and Eyre (1995) take note of this in their study of dike systems on the island. They suggest an extension of the North Fiji fault zone across the Tonga Trench may have caused this directional departure (**Figure 25**). Movement along the fault must have occurred between 1.8 and 1.00 Ma (Natland and Turner 1985), while Tutuila was in its shield-building stage. Walker and Eyre note the presence of post-erosional volcanics trending N160°E on the island, indicating a later change in stress patterns. The geodetic reconstruction of Hart et al. (2004) does not necessarily confound this claim, as it demonstrates that stresses associated with the Tonga Trench may have been in close enough proximity to Tutuila at the time of its formation. With limited evidence the plausibility of this scenario is unclear, however, and does not explain the continuation of the submarine Malu Trend.

The morphology of Tutuila exhibits several highly incised secondary rift zones radiating away from the primary trend. Protruding slightly from the southwestern corner of the island is a rift trending N20°E. Reinstating the primary *en echelon* trend, a massive rift juts N110°E and connects to Tulaga. A third rifting system extends from the northeastern corner of the island in a N30°E trend. This particular rift system is striking due to its apparent link to the formation of Soso. The linear nature of these features implies structural guidance of volcanism by fault or fracture zone. The island flanks are in a stage of advanced erosion, exhibiting numerous slope failures and incised rifts. Sparse populations of small seamounts occupy the western flank, as well as the northern and southern flanks, which are in line with the primary rift of Papatua.

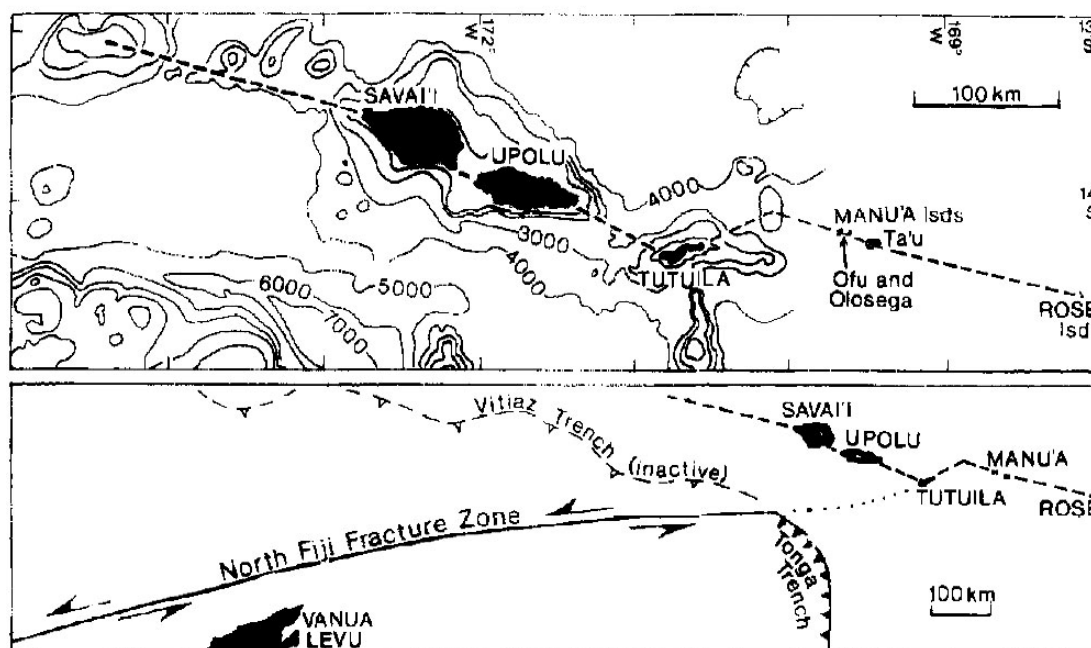


Figure 25: Diagram of potential mechanism for Tutuila offset by Walker and Eyre (1995).

6.2 Papatua

Papatua Guyot is the largest isolated edifice in the ESVP. Though it has not been radiometrically dated, it is probably at least as old as Tutuila, based on its location in the ESVP. The summit of Papatua sits very near sea level. It likely breached in the past and has since been eroded by wave action to produce a flat summit surface. Papatua has two perpendicular rifting trends nearly in line with the four cardinal directions. Though it is probably at least a million years old, its northern and southwestern flanks show relatively little evidence of slope failure and are superimposed with small seamounts. It shows an emerging stellate morphology, though it is not nearly as developed as on Tutuila or Muli. The shield-building stage for Papatua is not easily attributable to a plume source based on its divergent location and anomalous primary rift trend of No°E, though Hart et al. (2004) suggest decompressional melting due to slab-plume interactions could account for the location of Papatua.

6.3 Muli

Muli Guyot is the second largest isolated edifice in the ESVP. It is the western anchor of the Vai Trend and is partially connected to the Ofu-Olosega complex by a deep saddle. No radiometric

dates exist for Muli, though using $^{206}\text{Pb}/^{204}\text{Pb}$ ratios as a proxy places it between Tutuila and Malumalu in age (~0.8 Ma), though error bars indicate possible age overlap (**Figure 7**). Muli exhibits a near-stellate morphology, a testament to its highly eroded state and once circular shape. Its flat summit lies within 100 m of sea level and like Papatua, may have breached sometime in the past. Muli has two primary rift trends at N30°E and N120°E, the former resembling the strike of Soso and the latter constituting the direction of the Vai Trend. Its flanks are smooth and largely unimpinged by small seamounts. The exception is its eastern rift forming the saddle with the Ofu-Olosega complex, which is peppered with small seamounts.

6.4 Tulaga and Malumalu

Connected to the eastern edge of Tutuila by a 40 km rift, the Tulaga-Malumalu complex marks the termination of the Malu Trend. Neither edifice has been radiometrically dated. As with Muli, ages can be estimated using $^{206}\text{Pb}/^{204}\text{Pb}$ ratios (Workman et al. 2004). Samples were taken at Malumalu and place its age alongside Ta'u (~0.1 Ma), though error bars illustrate possible overlap with Muli and Vailulu'u (**Figure 7**). Due to the location of Tulaga “downrift” from Malumalu, its age is expected to be slightly older, perhaps similar to Ofu-Olosega. Malumalu and Tulaga share a common rift system in the Malu Trend, though the orientation along Tulaga departs slightly from the N110°E trend, hinging slightly south to N140°E. The N110°E trend resumes with Malumalu. Malumalu has a young morphology with few slope failures and a near-circular footprint. Tulaga exhibits a more erosive state. Its highly elongate form results from voluminous and continuous volcanic outpouring initiated at the southeastern flank of Tutuila. A brief lapse in shield volcanism creates a shallow saddle between Tulaga and Malumalu. Numerous small seamounts dot this coincident flank, as well as the eastern flank of Malumalu.

6.5 The Manu'a Islands

The Manu'a Island complex is denoted by voluminous and continuous shield volcanism beginning 15 km off the western coast of Ofu and terminating at Ta'u. Radiometric dates place an age range of the island complex between 0.3 Ma and 0.1 Ma, though the extended western flank of Ofu-Olosega is probably older, around 0.5 Ma based on the inferred age of Muli to the west. The Manu'a Island complex shares a common primary rift with Muli of N120°E. Numerous highly incised secondary rifts radiate from the complex. The largest and most pronounced rift juts from the southeast flank of Ta'u at a strike of N150°E. This rift is

accentuated by a massive slope failure that decimated the southern face of the island. Several other slope failures along the eastern flank of Ta'u illustrate the beginnings of a stellate morphology. A similar pattern is evident on the northern slope of Ofu-Olosega. While the shallow saddle between Ofu-Olosega and Ta'u is characterized by smooth slopes, the southern and western flanks of Ofu-Olosega are dominated by small seamounts. The small seamounts along the southern flank of Ofu-Olosega extend toward the Tulaga-Malumalu saddle and fill the inter-rift space between the two *en echelon* trends.

6.6 *Vailulu'u*

Vailulu'u has been described in great detail by Hart et al. (2000), though its general features will be revisited here. Vailulu'u is widely accepted as the current location of hotspot volcanism. It is a large edifice with a volume of approximately 1050 km³. Geochemical analysis of samples dredged from its summit yield ages of less than 50 years. It is relatively isolated from the rest of the Vai Trend, partially connected to Ta'u by a very deep saddle. The summit of Vailulu'u is distinct, as it is the only seamount in the ESVP with an active crater. Its primary rift diverges slightly from that of the Vai Trend, shifting slightly north to N90°E. A secondary rift protrudes from its southern flank at N160°E. Its northern and southern flanks mark some of the steepest slopes in the ESVP. There is evidence of slope failures on its northwestern, southwestern, and southeastern flanks that show an emerging stellate morphology, though in its very early stages. Its flanks are generally smooth with very little emplacement of small seamounts.

6.7 *Tama'i, Soso, and Malulu*

Tama'i, Soso, and Malulu are relatively small seamounts with volumes 58 km³, 232 km³, and 566 km³, respectively (Earthref.org 2007). Like Papatua, these seamounts are off-axis from the dominant *en echelon* trends. No studies of their geochemistry have been performed and little is known of their origins. All three are characterized by basal depths much deeper than those of *en echelon* seamounts (~4,800 m) and demonstrate highly undeveloped morphologies. Soso is unique in that it shows a clear structural relationship with the northeastern secondary rift extending from Tutuila. Tama'i and Malulu exhibit no such relationships with *en echelon* seamounts. While Tama'i is 30 km north of Tutuila, there are smaller seamounts in the intervening space, suggesting that it is perhaps also a satellite of the Tutuila rift system. The mechanism for this association is not clear, however. Decompressional melting due to slab-

plume interactions may explain its origin (Hart et al. 2004). Establishing a potential mode of emplacement for Malumalu is more problematic. It lies 40 km southeast of Vailulu'u, separated from it by a featureless abyss. Its morphology suggests a young age, however, it lies east of what is believed the current Samoan hotspot. Given the inconsistent distribution of large seamounts in the ESVP, characterized by unpredictable lapses in shield volcanism, it may not be reaching to suggest Malulu is an emerging manifestation of plume-driven volcanism.

6.8 Small Seamounts

The quantitative treatment of small seamount distributions in **Chapter 5** reveals that on average approximately 3 small seamounts per 1,000 km² occupy the space off-flank from large seamounts. There are, however, numerous small seamounts on-flank or otherwise unfit for inclusion in the distribution model. Fields of small-scale volcanics are prevalent throughout ESVP from Ofu-Olosega westward, especially on the northern flank of Papatua, and stretching from Ofu-Olosega across the inter-rift valley to the Tulaga-Malumalu saddle. Without radiometric ages, constraining their age and origin is a speculative exercise. Nevertheless, their superimposition on well-established shield volcanoes suggests they are manifestations of rejuvenated (i.e. post-erosional) volcanism. Their origin can be explained by three possible mechanisms: (1) lithospheric flexure due to stresses at the “corner” of the Tonga Trench allowing shallow-source volcanism (Hawkins and Natland 1975; Natland 1980; Natland and Turner 1985), (2) loading upon primary magma reservoirs by large seamounts resulting in radial dike propagation (Binard et al. 2004), or (3) decompressional melting of the lithosphere due to slab roll-back and plume response (Hart et al. 2004). While lithospheric flexure may combine with one or both of the other scenarios to produce rejuvenated volcanism, its influence seems unlikely beyond Tutuila and Papatua due to its limited stress field (Abbott and Fisk 1986). Scenarios two and three are the best suited to explain rejuvenated volcanism throughout the ESVP. In the case of the Papatua and Ofu-Olosega seamount fields, both are adjacent to massive shield volcanoes that could provide the requisite loading to squeeze out radial dikes. Additionally, diffusion of plume-driven volcanism subsequent to the passing of Tutuila is diagnostic of some plume disruption. This could account for both decompressional melting and plume-driven weakening of lithosphere, perhaps providing new conduits for release of magma from primary reservoirs.

6.9 En Echelon Lineaments and Age Progressions

The *en echelon* arrangement of lineaments in the ESVP does not fit a fixed hotspot model. At the inception of the Tutuila shield (~1.8 Ma) there is evidence of some plume disruption, first manifesting in the anomalous primary rifting direction of the Tutuila complex. The hotspot trail then resumes along a N110°E trend toward Tulaga. Prior to the formation of Tulaga, however, this plume disruption appears to cause a split, producing two simultaneously accreting and sub-parallel lineaments. Based on $^{40}\text{Ar}/^{39}\text{Ar}$, K-Ar, and ages inferred from $^{206}\text{Pb}/^{204}\text{Pb}$ ratios, this split initiated at approximately 0.8 Ma (shield volcanism may have begun slightly earlier) and continued until the recent (< 0.1 Ma) termination of Malumalu. The hotspot trail then resumes a single trace located at Vailulu'u. This arrangement is peculiar, if not perplexing, and prompts several questions. First, why is there a lapse in shield volcanism between Tutuila and Muli? Second, why does the Malu Trend terminate at Malumalu, failing to produce a counterpart to Vailulu'u? Lastly, how might Papatua and Malulu fit into this disjointed framework? The answers to these questions await further geochemical investigations and improved plume modeling.

7. Conclusion

7.1 Current Geomorphology

The ESVP is a region dominated by mantle plume volcanism. However, the behavior of this plume system does not conform to standards established by other plume-induced island chains in the Pacific. This abnormal behavior is likely due to interactions between the Samoan plume and eastward roll-back of the Pacific plate as it subducts into the Tonga Trench (Hart et al. 2004). It should be noted that lithospheric flexure (Hawkins and Natland 1975; Natland 1980; Natland and Turner 1985) cannot be discounted as a source of rejuvenated volcanism, or perhaps even a source of future shield volcanism as the Tonga Trench continues to migrate eastward at a rapid rate. The bifurcated arrangement of major volcanic lineaments in the ESVP are unusual and, based on isotopic ages, suggest that shield-building was occurring simultaneously at locations 30 km apart. The initiation of this sequence was apparently around 0.8 Ma, as Muli and the ridge connecting Tutuila and Tulaga began accreting synchronously. The amount of shield volcanism wanes from this point on, though combining the volcanic mass of both lineaments may produce a single lineament roughly the size of Tutuila.

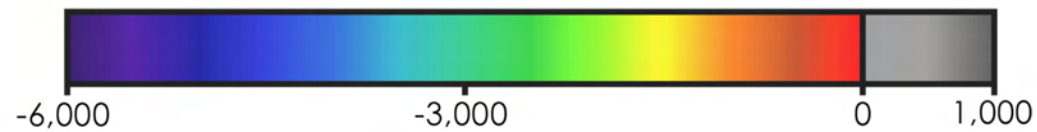
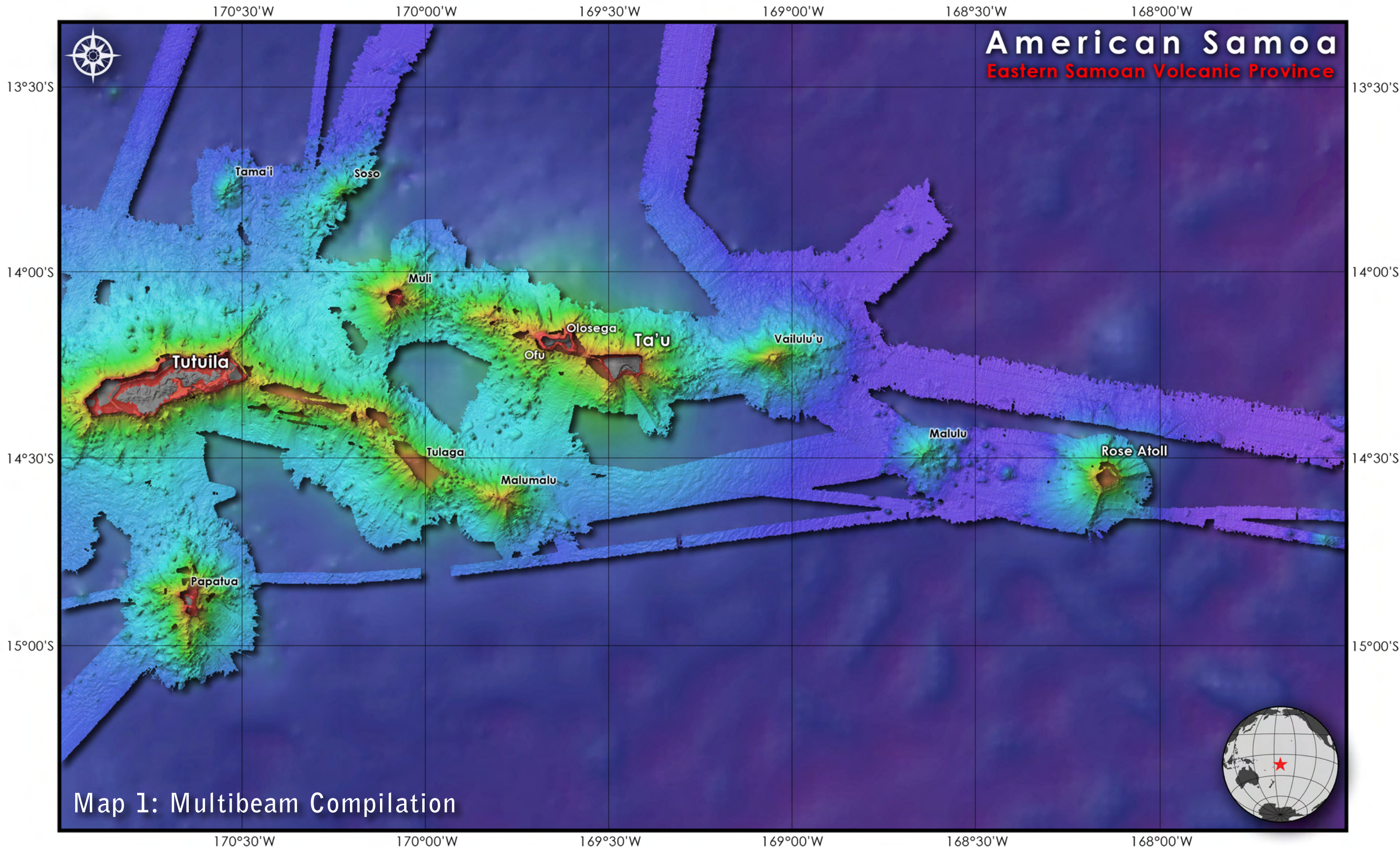
Small seamounts on the on-flank and off-flank of large seamounts, guyots, and islands may represent rejuvenated volcanism. The source of this volcanism is unclear, though several possible mechanisms have been proposed (Hawkins and Natland 1975; Natland 1980; Natland and Turner 1985; Binard et al. 2004; Hart et al. 2004). These mechanisms do not appear to be mutually exclusive and in fact may all be in play. Shape analysis of off-flank seamounts reveals that most conform to expected morphologies of seamounts in the Pacific. Those with anomalous morphologies demonstrate a low-viscosity lobate form, implying an effusive or “quiet” eruptive style. This suggests a low-silica, MORB-type magma source with minimal volatile enrichment, not expected in this type of geologic environment (Binard et al. 2004). Densities of off-flank seamounts do demonstrate values expected in the Pacific, though similar studies show that proximate regions have somewhat higher densities. Minor variation in densities throughout the Pacific has been established, though its causes presently unexplained (Smith and Jordan 1988).

The geomorphologic perspective presented in this study provides additional insight into the processes responsible for the formation of volcanic features in the ESVP. However, it is clear that studies of geomorphology alone cannot resolve all remaining uncertainties. Of available techniques, continuing geochemical investigations may yield the most telling data. Numerous dredge sites in the ESVP were visited during the ALIA Expedition of 2005 and publications from analyses of those samples are forthcoming (Koppers et al., awaiting publication). A better understanding of plume behavior may also be applied to the ESVP through advanced modeling and tomographic imaging.

7.2 Future Work

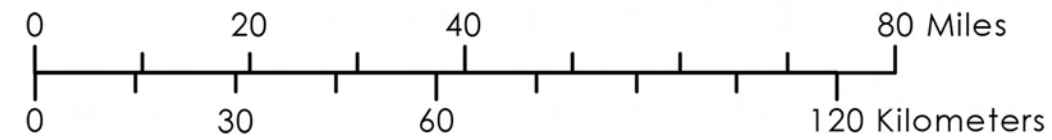
Shape analysis has produced an abundance of geomorphologic information for 51 newly identified small seamounts in the ESVP. These data will be submitted to the Seamount Catalog at Earthref.org (2007), where it will be added to a registry of submarine features already 1,800 strong, and may benefit future work in the region. In addition to geomorphologic characteristics, the Seamount Catalog is collecting high-resolution multibeam bathymetry and coverage is currently expanding in the ESVP, especially in shallow areas associated with coral reefs. Though unavailable at this time, bathymetry collected by NOAA PIFSC in 2006 will be

added to the multibeam compilation for the ESVP. An updated compilation will be showcased on a website devoted to the geovisual aspects of this study (<http://dusk.geo.orst.edu/djl/theses/roberts.html>).

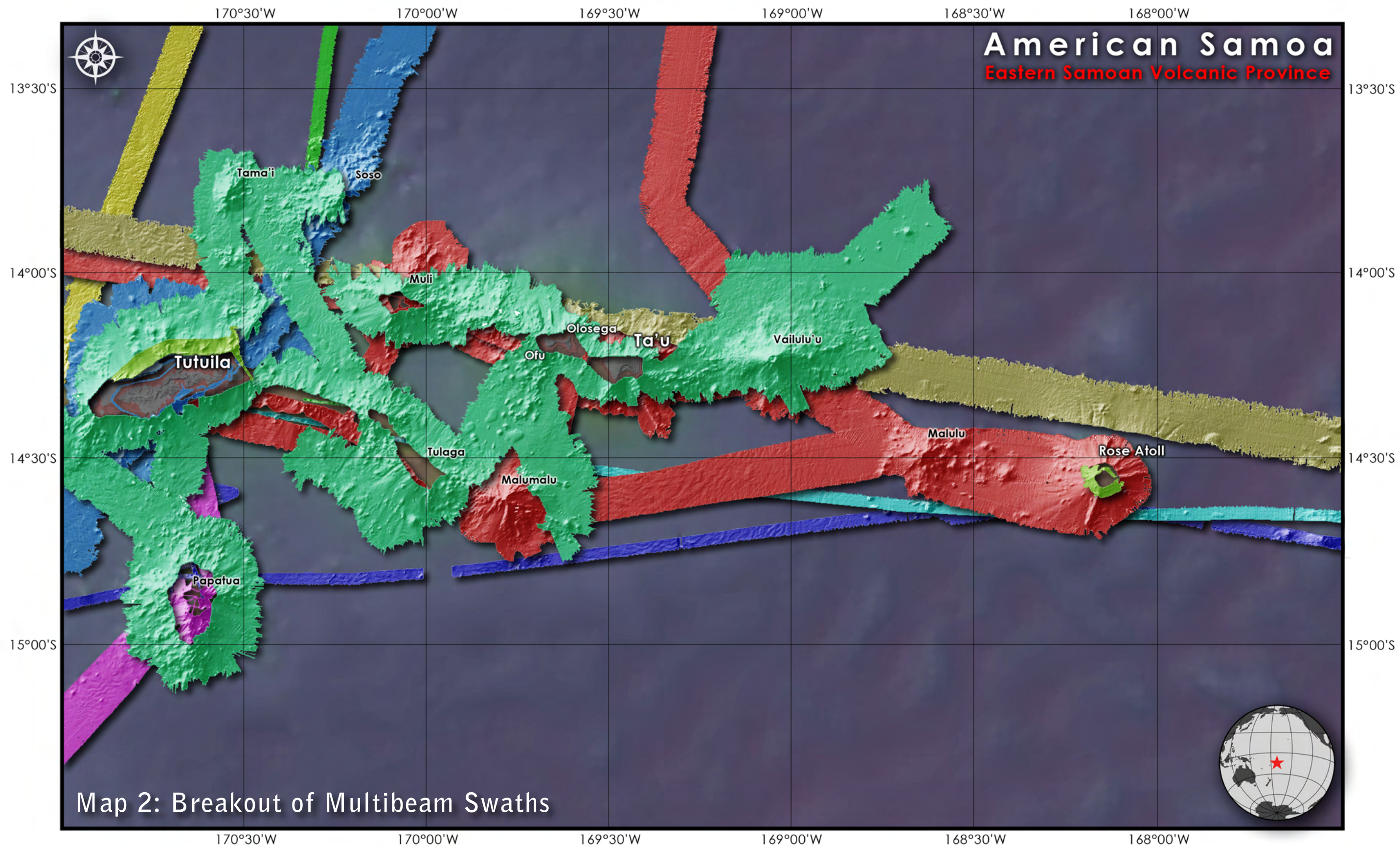


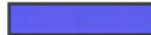
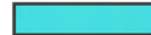
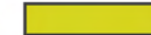
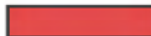
Elevation (meters) with respect to sea level

200 meter resolution bathymetric grid in foreground. Predicted bathymetric surface derived from one kilometer satellite altimetry in background.



Data Source: Seamount Catalog - EarthRef.org | Projection: Linear WGS-84
Cartography: Jed Roberts, Oregon State University | Date: October, 2007

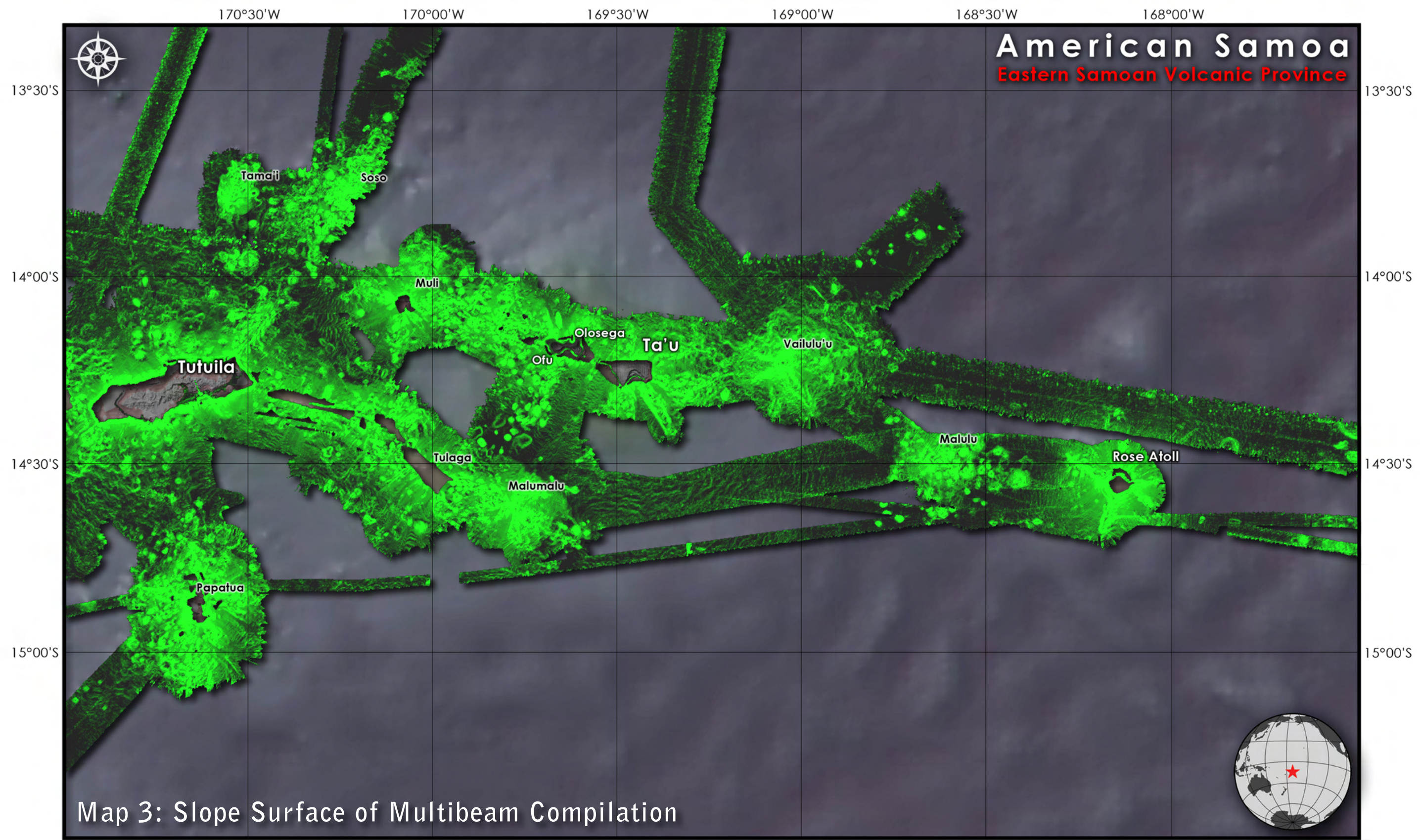


- | | | | | |
|---|---|---|---|--|
|  Marathon (1984) |  Papatua (1985-86) |  Roundabout (1989) |  Boomerang (1996) |  Kiwi (1997) |
|  AVON (1999) |  Cook (2001) |  Drift (2002) |  ALIA (2005) |  HURL (2005-06) |

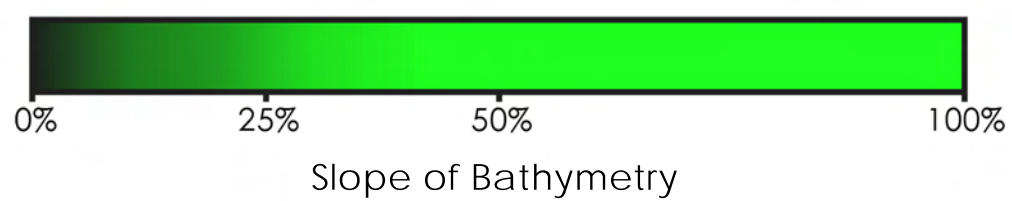
Multibeam bathymetry by research expedition. Swaths layered chronologically. Shallow swaths by PIFSC and KM0505 not included. RNDB15WT overlapped completely. 180 meter resolution.

0 20 40 80 Miles
0 30 60 120 Kilometers

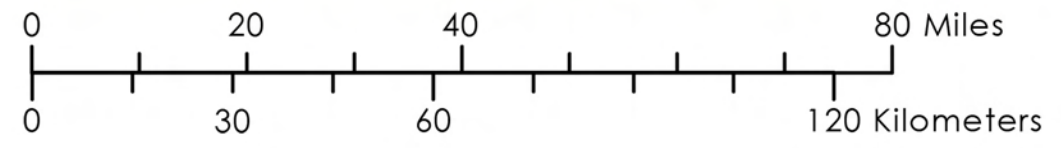
Data Source: Seamount Catalog - EarthRef.org | Projection: Linear WGS-84
Cartography: Jed Roberts, Oregon State University | Date: October, 2007



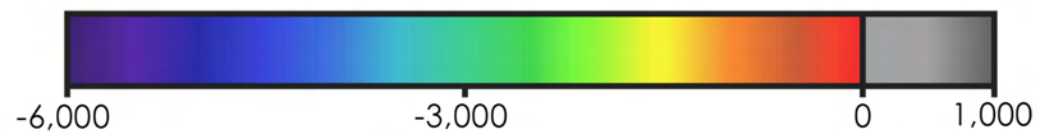
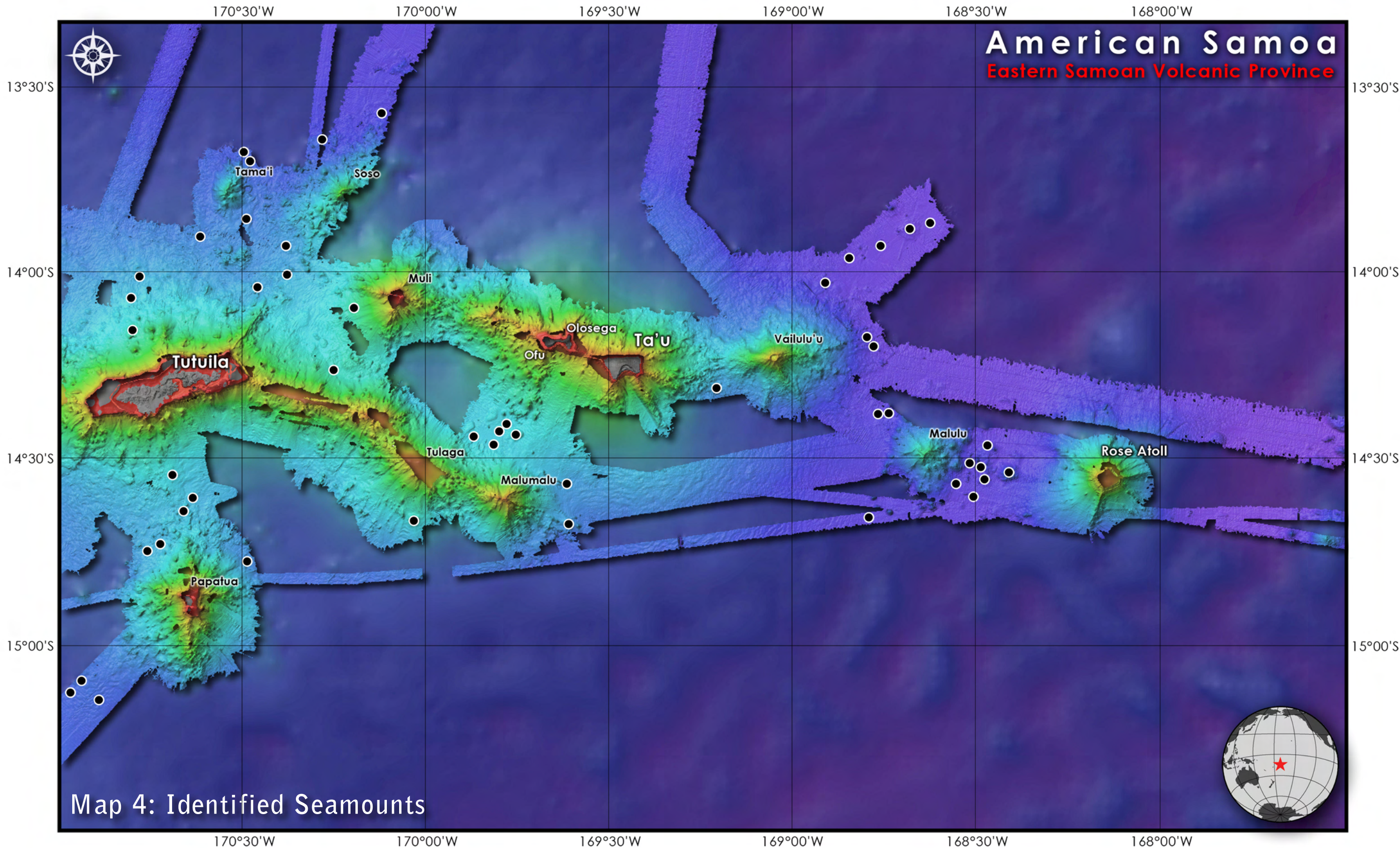
Map 3: Slope Surface of Multibeam Compilation



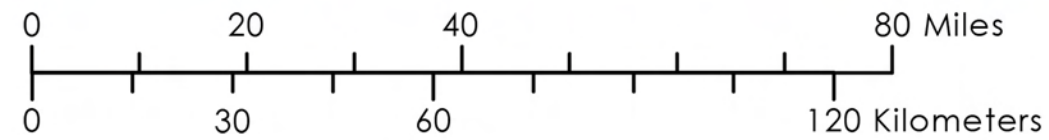
Slope calculation from 200 meter resolution bathymetric grid in foreground. Predicted bathymetric surface derived from one kilometer satellite altimetry in background.



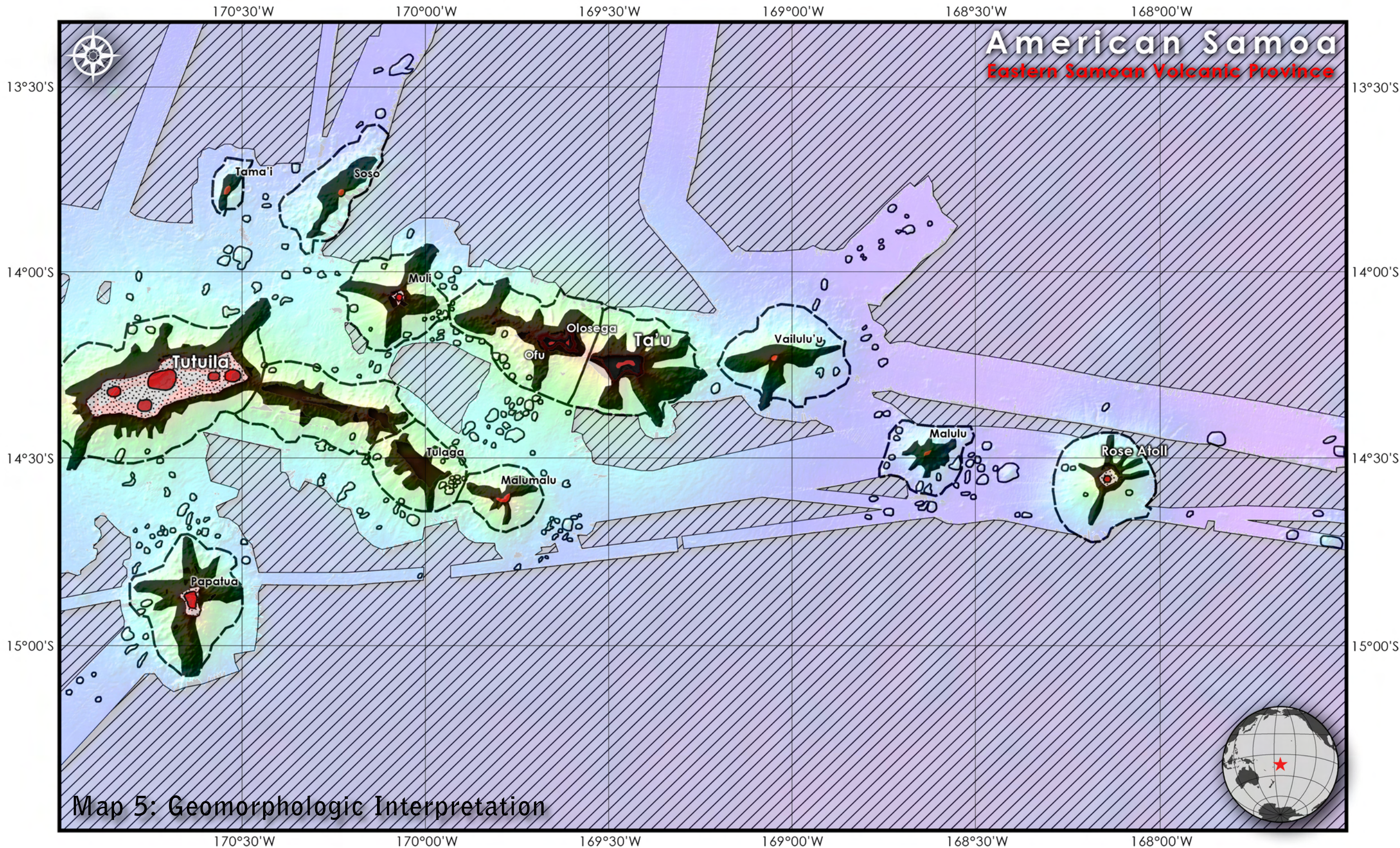
Data Source: Seamount Catalog - EarthRef.org | Projection: Linear WGS-84
 Cartography: Jed Roberts, Oregon State University | Date: October, 2007



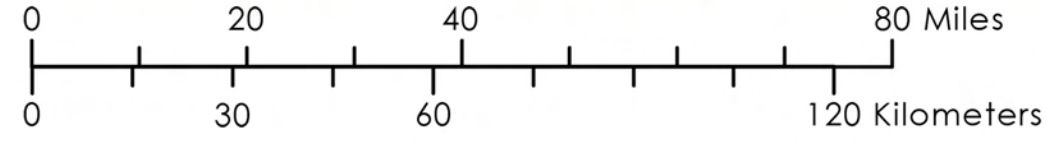
200 meter resolution bathymetric grid in foreground. Predicted bathymetric surface derived from one kilometer satellite altimetry in background.



Data Source: Seamount Catalog - EarthRef.org | Projection: Linear WGS-84
Cartography: Jed Roberts, Oregon State University | Date: October, 2007



Geomorphologic interpretation of major volcanic structures with 200 meter multibeam bathymetry in background.



Data Source: Seamount Catalog - EarthRef.org | Projection: Linear WGS-84
Cartography: Jed Roberts, Oregon State University | Date: October, 2007

8. References

- Abbott, D. H., and Fisk, M. 1986. Tectonically controlled origin of three unusual rock suites in the Woodlark Basin. *Tectonics*. 5(7): 1145-60.
- Abers, G. A., Parsons, B., and Weissen, J. K. 1988. Seamount abundances and distributions in the southeast Pacific. *Earth and Planetary Science Letters*. 87: 137-51.
- Anderson, D. L., and Natland, J. H. 2005. A brief history of the plume hypothesis and its competitors: Concept and controversy. *Geological Society of America. Special Paper*(338): 119-45.
- Barazangi, M., and Isacks, B. 1971. Lateral variation of seismic-wave attenuation in the upper mantle above the inclined earthquake zone of the Tonga Island arc: deep anomaly in the mantle. *Journal of Geophysical Research*. 76: 8493-515.
- Batiza, R. 1982. Abundances, distribution and sizes of volcanoes in the Pacific Ocean and implications for the origin of non-hotspot volcanoes. *Earth and Planetary Science Letters*. 60: 195-206.
- Bell, T. H. 1975. Statistical features of sea-floor topography. *Deep Sea Research*. 22: 883-92.
- Bemis, K. G., and Smith, D. K. 1993. Production of small volcanoes in the Superswell region of the South Pacific. *Earth and Planetary Science Letters*. 118: 251-62.
- Binard, N., Hekinian, R., Cheminée, J. L., Searle, R. C., and Stoffers, P. 1992. Style of eruptive activity on intraplate volcanoes in the Society and Austral hot spot regions: Bathymetry, petrology, and submersible observations. *Journal of Geophysical Research*. 97: 13999-4015.
- Binard, N., Hekinian, R., Stoffers, P., and Cheminée, J. L. 2004. South Pacific Intraplate Volcanism: Structure, Morphology and Style of Eruption. In *Oceanic Hotspots: Intraplate Submarine Magmatism and Tectonism*. Edited by Hekinian, R., Stoffers, P. and Cheminée, J. L. New York, NY. Springer-Verlag Press: 157-207.
- Bonatti, E., and Harrison, C. G. A. 1988. Eruption styles of basalt in oceanic spreading ridges and seamounts: Effect of magma temperature and viscosity. *Journal of Geophysical Research*. 93: 2967-80.
- Burke, K. C., and Wilson, J. T. 1976. Hot spots on the Earth's surface. *Journal of Geophysical Research*. 93: 7690-708.
- Caress, D. W., and Chayes, D. N. 1996. Improved Processing of Hydrosweep DS Multibeam Data and the R/V Maurice Ewing. *Marine Geophysical Researches*. 18: 631-50.
- Cochran, J. R. 1986. Variations in subsidence rates along intermediate and fast spreading mid-ocean ridges. *Geophysical Journal of the Royal Astronomical Society*. 87: 421-54.
- Courtillot, V., Davaille, A., Besse, J., and Stock, J. 2003. Three distinct types of hotspots in the Earth's mantle. *Earth and Planetary Science Letters*. 205: 295-308.

- Craig, H., and Lupton, J. E. 1976. Primordial neon, helium, and hydrogen in oceanic basalts. *Earth and Planetary Science Letters*. 31: 369-85.
- Craig, H., and Lupton, J. E. 1981. Helium-3 and mantle volatiles in the ocean and oceanic lithosphere. *The Sea*. Vol. 7, C. Emiliani, ed., Wiley, New York: 391-428.
- Daly, R. A. 1924. The geology of American Samoa. *Carnegie Institute, Washington Publication*. 340: 95-145.
- Dana, J. D. 1849. US Exploring expedition during the years 1838-1842 under command of Charles Wilkes, USN. *Geology*. 10: 307-36.
- Davis, E. E., Currie, R. G., Sawyer, B. S., and Kosalos, J. G. 1986. The Use of Swath Bathymetric and Acoustic Image Mapping Tools in Marine Geoscience. *Marine Technology Society Journal*. 20(4): 17-27.
- de Moustier, C. 2002. Field Evaluation of Sounding Accuracy in Deep Water. *IEEE Ocean Engineering Society Newsletter*. 37(4): 1761-5.
- Detrick, R. S., and Crough, S. T. 1978. Island subsidence, hotspots and lithospheric thinning. *Journal of Geophysical Research*. 83: 1236-44.
- Duncan, R. A. 1985. Radiometric ages from volcanic rocks along the New Hebrides-Samoa lineament. *Circum-Pacific Council for Energy and Mineral Resources Earth Science Series*. 3: 67-76.
- Earthref.org. 2007. Seamount Catalog. <http://www.earthref.org/databases/SC/main.htm>. Accessed 10/28/2007.
- Farley, K. A., Natland, J. H., and Craig, H. 1992. Binary mixing of enriched and undegassed (primitive?) mantle components (He, Sr, Nd, Pb) in Samoan lavas. *Earth and Planetary Science Letters*. 111: 183-99.
- Fornari, D. J., Ryan, W. B. F., and Fox, P. J. 1983. Sea MARC 1 and SEA BEAM sonar studies of seamounts near the East Pacific Rise at 10 degrees N; the evolution of seamount structure and morphology. *Eos Transactions. American Geophysical Union*. 64(45): 729-30.
- Friedlander, I. 1910. Beitrage zur der Samoa inseln. *Bayerische Akademie der Wissenschaften. Mathematisch-Physik Klasse*. 24: 509-41.
- Goff, J. A., and Jordan, T. H. 1988. Stochastic Modeling of Seafloor Morphology: Inversion of Sea Beam Data for Second-Order Statistics. *Journal of Geophysical Research*. 93(B11): 13,589-608.
- Goff, J. A., and Jordan, T. H. 1989. Stochastic Modeling of Seafloor Morphology: Resolution of Topographic Parameters by Sea Beam Data. *IEEE Journal of Ocean Engineering*. 14(4): 326-37.
- Hart, S. R., Staudigel, H., Koppers, A. A. P., Blusztajn, J., Baker, E. T., Workman, R., Jackson, M., Hauri, E., Kurz, M., Sims, K., Fornari, D., Saal, A., and Lyons, S. 2000. Vailulu'u undersea volcano: The New Samoa. *Geochemistry Geophysics Geosystems*. 1(12): 2000GC000108.

- Hart, S. R., Coetzee, M., Workman, R. K., Blusztajn, J., Johnson, K. T. M., Sinton, J. M., Steinberger, B., and Hawkins, J. W. 2004. Genesis of the Western Samoa seamount province: age, geochemical fingerprint and tectonics. *Earth and Planetary Science Letters*. 227: 37-56.
- Hauri, E. H., and Hart, S. R. 1994. Constraints on melt migration from mantle plumes: A trace element study of peridotite xenoliths from Savai'i, Western Samoa. *Journal of Geophysical Research*. 99(B12): 24301-21.
- Hawkins, A. B. 1987. Samoa: Significance of its Geological Setting. *Memoirs of the Geological Society of China*. 9: 159-74.
- Hawkins, J. W., and Natland, J. H. 1975. Nephelinites and Basanites of the Samoan Linear Volcanic Chain: Their Possible Tectonic Significance. *Earth and Planetary Science Letters*. 24: 427-39.
- Hekinian, R., Stoffers, P., and Cheminée, J. L. 2004. *Oceanic Hotspots: Intraplate Submarine Magmatism and Tectonism*. New York, NY. Springer-Verlag Press: p. 1.
- Hess, H. H. 1962. History of the ocean basins. In *Petrologic Studies: A Volume in Honor of A. F. Buddington*. Geological Society of America: 599-620.
- Hill, P. J., and Tiffin, D. L. 1991. Marine geology and geophysics of the Western Samoa exclusive economic zone: results of GLORIA, SeaMARC II and other shipboard studies. *SOPAC Technical Report*. 135: 1-56.
- Hirano, N., Takahashi, E., Yamamoto, J., Abe, N., Ingle, S.P., Kaneoka, I., Hirata, T., Kimura, J., Ishii, T., Ogawa, Y., Machida, S., and Suyehiro, K. 2006. Volcanism in Response to Plate Flexure. *Science*. 313: 1426-28.
- Hollister, C. D., Glenn, M. F. and Lonsdale, P. F. 1978. Morphology of Seamounts in the Western Pacific and Philippine Basin from multi-beam sonar data. *Earth and Planetary Science Letters*. 41: 405-18.
- Hubbard, N. J. 1971. Some chemical features of lavas from the Manu'a Islands, Samoa. *Pacific Science*. 25: 178-87.
- Jackson, M. G., and Hart, S. R. 2006. Strontium isotopes in melt inclusions from Samoan basalts: Implications for heterogeneity in the Samoan plume. *Earth and Planetary Science Letters*. 245: 260-77.
- Jackson, M. G., Hart, S. R., Koppers, A. A. P., Staudigel, H., Konter, J., Blusztajn, J., Kurz, M., Russell, J. A. 2007. The return of subducted continental crust in Samoan lavas. *Nature*. 448(doi: 10.1038/nature06048): 684-7.
- Jaroslow, G. E., Smith, D. K., and Tucholke, B. E. 2000. Record of seamount production and off-axis evolution in the western North Atlantic Ocean, 25°25'-27°10'N. *Journal of Geophysical Research*. 105(B2): 2721-36.
- Jarrard, R. D., and Clague, D. A. 1977. Implications of Pacific island and seamount ages for the origin of volcanic chains. *Reviews of Geophysics and Space Physics*. 15: 57-76.

- Johnson, R. H. 1984. Exploration of three submarine volcanos in the South Pacific. *National Geographic Society Research Reports*. 16: 405-20.
- Jordan, J. H., Menard, H. W. and Smith, D. K. 1983. Density and Size Distribution of Seamounts in the Eastern Pacific Inferred From Wide-Beam Sounding Data. *Journal of Geophysical Research*. 88(B12): 10508-18.
- Kleinrock, M. C., and Brooks, B. A. 1994. Construction and destruction of volcanic knobs at the Cocos-Nazca spreading system near 95°W. *Geophysical Research Letters*. 21(21): 2307-10.
- Koppers, A. A. P., Russell, J. A., Jackson, M. G., Konter, J., Staudigel, H., and Hart, S. R. Awaiting publication. Samoa Reinstated as a Primary Hotspot Trail.
- Kurz, M. D., Jenkins, W. J., and Hart, S. R. 1982. Helium, isotopic systematics of ocean islands and mantle heterogeneity. *Nature*. 267: 43-6.
- Litvin, V. M., Lomonosov, Y. I., and Blazhchishin, A. I. 1985. Investigation of Josephine Seamount. *Oceanology*. 24(4): 538-40.
- Lost City Expedition. 2003. <http://www.lostcity.washington.edu>. Accessed 11/6/2007.
- Luis, J. F. 2007. Mirone: A multi-purpose tool for exploring grid data. *Computers & Geosciences*. 33: 31-41.
- Lundblad, E., Wright, D.J., Miller, J., Larkin, E.M., Rinehart, R., Battista, T., Anderson, S.M., Naar, D.F., and Donahue, B.T. 2006. A benthic terrain classification scheme for American Samoa. *Marine Geodesy*. 26(2): 89-111.
- MacDonald, G. A. 1968. A contribution to the petrology of Tutuila, American Samoa. *Geologische Rundschau*. 57(3): 821-37.
- MacDonald, G. A., and Abbott, A. 1970. Volcanoes in the Sea. *In The Geology of Hawaii*. Honolulu, HI. University of Hawaii Press.
- Mammerickx, J., Hayes, D. E., and Conolly, J. R. 1973. Bathymetry of the South Pacific (Map). *IMR Technical Report Series*. Scripps Institution of Oceanography: TR 44A-54A.
- McDougall, I., and Duncan, R. A. 1980. Linear volcanic chains -- recording plate motions? *Tectonophysics*. 63: 275-95.
- McDougall, I. 1985. Age and Evolution of the Volcanoes of Tutuila, American Samoa. *Pacific Science*. 39(4): 311-20.
- Menard, H. W. 1959. Geology of the Pacific sea floor. *Experimentia*. 15: 205-13.
- Menard, H. W. 1964. *Marine Geology of the Pacific*. New York, NY: McGraw-Hill: p. 55.
- Mitchell, N. C. 2001. Transition from circular to stellate forms of submarine volcanoes. *Journal of Geophysical Research*. 106(B2): 1,987-2,003.

- Morgan, W. J. 1971. Convection plumes in the lower mantle. *Nature*. 230: 42.
- Mougenot, D., Kidd, R. B., Mauffret, A., Regnaud, H., Rothwell, R. G., and Vanney, J. 1984. Geological interpretation of combined SEABEAM, GLORIA and seismic data from Porto and Vigo seamounts, Iberian continental margin. *Marine Geophysical Researches*. 6(4): 329-63.
- Natland, J. H. 1980. The progression of volcanism in the Samoan linear volcanic chain. *American Journal of Science*. 280-A: 709-35.
- Natland, J. H. 2004. The Samoan Chain: A Shallow Lithospheric Fracture System. <http://www.mantleplumes.org/Samoa.html>. Accessed 10/16/2007.
- Natland, J. H., and Turner, D. L. 1985. Age progression and petrological development of Samoan shield volcanoes: evidence from K-AR ages, lava compositions, and mineral studies. *Circum-Pacific Council for Energy and Mineral Resources Earth Science Series*. 3: 139-71.
- Oceanus. 2005. Nafanua, Eel City, and the Crater of Death. *Oceanus, Woods Hole Oceanographic Institution*. <http://www.whoi.edu/oceanus/viewArticle.do?id=7142&archives=true>. Accessed 11/6/2007.
- PIBHMC. 2004. Multibeam Metadata. <http://www.soest.hawaii.edu/pibhmc>. Accessed 10/18/2007.
- Rappaport, Y., Naar, D. F., Barton, C. C., Liu, Z. J., and Hey, R. N. 1997. Mophology and distrubution of seamounts surrounding Easter Island. *Journal of Geophysical Research*. 102(B11): 24,713-28.
- Rodgers, K. A., Sutherland, F. L., and Hoskin, P. W. O. 2003. Basalts from Rose Atoll, American Samoa. *Records of the Australian Museum*. 55: 141-52.
- Rubin, A. M., and Pollard, D. D. 1987. Origin of blade-like dikes in volcanic rift zone. In *Volcanism in Hawaii*. Edited by Decker, R. D., Wright, T. L., and Stauffer, P. H. US Geological Survey Professional Papers(1350): 1449-70.
- Sandwell, D. T., and Smith W. H. F. 1997. Marine gravity anomoly from Geosat and ERS 1 satellite altimetry. *Journal of Geophysical Research*. 102(B5): 10,039-54.
- Scheirer, D. S., and Macdonald, K. C. 1995. Near-axis seamounts on the flanks of the East Pacific Rise, 8°N to 17°N. *Journal of Geophysical Research*. 100(B2): 2239-59.
- Scheirer, D. S., MacDonald, K. C., Forsyth, D. W., and Shen, Y. 1996. Abundant Seamounts of the Rano Rahi Seamount Field Near the Southern East Pacific Rise , 15° S to 19° S. *Marine Geophysical Researches*. 18: 13-52.
- Searle, R. C. 1983. Submarine central volcanoes on the Nazca Plate; high-resolution sonar observations. *Marine Geology*. 53(1-2): 77-102.
- SIOExplorer. 2007. Cruise Viewer. <http://nsdl.sdsc.edu/cruises/>. Accessed 10/14/2007.

- Smith, D. K. 1988. Shape analysis of Pacific seamounts. *Earth and Planetary Science Letters*. 90: 457-66.
- Smith, D. K., and Cann, J. R. 1990. Hundreds of small volcanoes on the median valley floor of the Mid-Atlantic Ridge at 24°-30° N. *Nature*. 348: 152-5.
- Smith, D. K., and Cann, J. R. 1992. The Role of Seamount Volcanism in Crustal Construction at the Mid-Atlantic Ridge (24°-30°N). *Journal of Geophysical Research*. 97(B2): 1645-58.
- Smith, D. K., and Jordan, T. H. 1988. Seamount Statistics in the Pacific Ocean. *Journal of Geophysical Research*. 93(B4): 2899-918.
- Smith, J. R., Dunbar, R. B., and Parrish, F. A. 2006. First Multibeam Mapping of Deep-Water Habitats in the U.S. Line Islands. *Eos Transactions. American Geophysical Union*. 86(36): Ocean Science Meeting.
- Smoot, C. N. 1982. Guyots of the Mid-Emperor Chain mapped with multibeam sonar. *Marine Geology*. 47(1-2): 153-63.
- Smoot, C. N. 1983a. Detailed bathymetry of guyot summits in the North Pacific by multi-beam sonar. *Surveying and Mapping*. 43(1): 53-60.
- Smoot, C. N. 1983b. Ninigi and Godaigo seamounts; twins of the Emperor Chain by multi-beam sonar. *Tectonophysics*. 98(3-4): T1-T5.
- Smoot, C. N. 1985. Observations of Gulf of Alaska seamount chains by multi-beam sonar. *Tectonophysics*. 115(3-4): 235-46.
- Staudigel, H., Hart, S. R., Pile, A., Bailey, B. E., Baker, E. T., Brooke, S., Connelly, D. P., Haucke, L., German, C. R., Hudson, I., Jones, D., Koppers, A. A. P., Konter, J., Lee, R., Pietsch, T. W., Tebo, B. M., Templeton, A. S., Zierenberg, R., and Young, C. M. 2006. Vailulu'u Seamount, Samoa: Life and death on an active submarine volcano. *Proceedings of the National Academy of Sciences of the United States of America*. 103(17): 6448-53.
- Stearns, H. T. 1944. Geology of the Samoan Islands. *Geological Society of America Bulletin*. 55: 1279-1332.
- Stice, G. D. 1968. Petrography of the Manu'a Islands, Samoa. *Contributions to Mineralogy and Petrology*. 19: 343-57.
- Stice, G. D., and McCoy Jr., F. W. 1968. The Geology of the Manu'a Islands, Samoa. *Pacific Science*. 22: 427-57.
- Tarling, D. H. 1966. The paleomagnetism of the Samoan and Tongan Islands. *Royal Astronomical Society Geophysical Journal*. 10: 497-513.
- Theberge, A. E. 1989. Sounding Pole to Sea Beam. *Surveying and Cartography*. 5: 334-46.
- Turko, N. N., and Agapova, G. V. 2003. Methodical Features of Mapping Underwater Topography with Multibeam Echosounders. *Oceanology*. 43(2): 285-92.

- Tyce, R. C. 1986. Deep Seafloor Mapping Systems - A Review. *Marine Technology Society Journal*. 20(4): 4-16.
- Vogt, P. R. 1974. Volcano Height and Plate Thickness. *Earth and Planetary Science Letters*. 23: 337-48.
- Vogt, P. R., and Jung, W. Y. 2000. GOMaP: A Matchless Resolution to Start the New Millennium. *Eos Transactions. American Geophysical Union*. 81(43): 254-8.
- Vogt, P. R., and Smoot, N. C. 1984. The Geisha Guyots: Multibeam Bathymetry and Morphometric Interpretation. *Journal of Geophysical Research*. 89(B13): 11,085-107.
- Walker, G. P. L., and Eyre, P. R. 1995. Dike complexes in American Samoa. *Journal of Volcanology and Geothermal Research*. 69: 241-54.
- Wessel, P., and Smith, W. H. F. 1991. Free Software Helps Map and Display Data. *Eos Transactions. American Geophysical Union*. 72(41): 441-8.
- White, W. M. 1985. Sources of oceanic basalts: radiogenic isotope evidence. *Geology*. 13: 115-8.
- Wilkes, C. 1843. United States exploring expedition. *American Journal of Science and Arts*. 44(2): 393-408.
- Wilson, J. T. 1963. A possible origin of the Hawaiian Islands. *Canadian Journal of Physics*. 41: 863.
- Workman, R. K., Hart, S. R., Jackson, M., Regelous, M., Farley, K. A., Blusztajn, J., Kurz, M., and Staudigel, H. 2004. Recycles metasomatized lithosphere as the origin of the Enriched Mantle II (EM₂) end-member: Evidence from the Samoan Volcanic Chain. *Geochemistry Geophysics Geosystems*. 5(4): 2003GC000623.
- Workman, R. K., Hauri, E., Hart, S. R., Wang, J., and Blusztajn, J. 2006. Volatile and trace elements in basaltic glasses from Samoa: Implications for water distribution in the mantle. *Earth and Planetary Science Letters*. 241: 932-51.
- Wright, D. J. 2002. Mapping the Seafloor in American Samoa. *Geospatial Solutions*. 12(7): 24-5.
- Wright, D. J., Donahue, B. T., and Naar, D. F. 2002. Seafloor Mapping and GIS Coordination at America's Remotest National Marine Sanctuary (American Samoa). In *Undersea with GIS*. Edited by Wright, D. J. Redlands, CA. ESRI Press: 33-63.
- Wright, D. J. 2005. Report of HURL Cruise KOKo510: Submersible Dives and Multibeam Mapping to Investigate Benthic Habitats of Tutuila, American Samoa. *Technical Report, NOAA's Office of Undersea Research Submersible Science Program, Hawai'i Undersea Research Lab*. http://dusk.geo.orst.edu/djl/samoa/hurl/koko510cruise_report.pdf. Accessed 10/16/2007.
- Wright, E., and White, W. M. 1987. The origin of Samoa: new evidence from Sr, Nd, and Pb isotopes. *Earth and Planetary Science Letters*. 81: 151-62.

Zindler, A. S., and Hart, S. R. 1986. Chemical Geodynamics. *Annual Review of Earth and Planetary Science Letters*. 14: 493-571.

9. Appendix A: Multibeam Compilation Technical Notes

9.1 The MB-System Datalist

The raw multibeam bathymetry datasets for this study were collected by a variety of multibeam systems aboard numerous research vessels. Acquisition of these datasets was achieved primarily through access to the multibeam collection hosted at the Seamount Catalog on Earthref.org (2007). Additional datasets are available at SIOExplorer (2007) and PIBHMC (2004). Datasets consist of raw multibeam files (eg. *.mb, *.mb16, etc.) that typically include a data format number within the filename. These data format numbers correspond to specific multibeam systems and advise MB-System (Caress and Chayes 1996) about how to process them. In order to compile a group of raw multibeam files into a single compilation, a simple text file listing each file and data format is required. The following is an abbreviated example of an MB-System datalist text file used in this study.

```
SAMOA/AVON02MV/SBunflagfix.99mar08.corr.roll.ed.mb 32
SAMOA/BMRG08MV/SBdespike.96jun08.truep.mb32.mb 32
SAMOA/COOK15MV/SBdespike.2001nov01.truep.mb32.mb 32
SAMOA/DRFT09RR/0015_20020307_095826p.mb57.mb 57
SAMOA/KIWI05RR/sb2100_vf.19971006-1200p.mb41.mb 41
SAMOA/KM0505/em1002-090-120856-0001.mb57.mb 57
SAMOA2/KOK0510/1/sb1910507111457_e.mb11 11
SAMOA2/MRTN05WT/MRTN05WT.SWSB.84aug22.truep.mb16.mb 16
SAMOA/NOAA2004-MANUA/ahmba04036.d07.mb121.mb 121
```

As made evident by the filenames, some of the raw multibeam files have been edited to account for vessel roll or data spikes (i.e. outliers) in the depth readings. This is not always the case, however, and manual ping-editing may be required to reduce the presence of artifacts in the data.

9.2 The MB-System “mbinfo” Command

Important information about a raw multibeam file is often not evident through the filename alone. To access additional information about a raw multibeam file, such as its mode of depth enumeration and coordinate system, it may be necessary to use the “mbinfo” command. The following is an example of the command.

```
mbinfo -F32 -ISBdespike.96jun08.truep.mb32.mb
```

For basic statistics about the file, it is only necessary to define the data format and filename, though additional options are available. The following is the output from the “mbinfo” command.

```
Swath Data File:      SBdespike.96jun08.truep.mb32.mb
MBIO Data Format ID:  32
Format name:         MBF_SB2000SB
Informal Description: SIO Swath-bathy SeaBeam 2000 format
Attributes:          SeaBeam 2000, bathymetry, 121 beams,
                    binary, SIO.
```

```
Metadata:
Vessel:              Melville
Institution:         SIO
Platform:            Ship
Sonar:               Seabeam_2000
Sonar Version:       Seabeam_2000_3.18
Cruise ID:          BMRG08MV
Cruise Name:        Boomerang_Expedition_leg_8
PI:                  Sherm_Bloomer
PI Institution:      Oregon_State_University
Client:              NSF/OCE94-00707
Corrected Depths:   YES
Tide Corrected:     NO
Depths Manually Edited: NO
Depths Auto-Edited: YES
Roll Bias:           0.000000 degrees
Pitch Bias:          0.000000 degrees
Heading Bias:        0.000000 degrees
Draft:               5.000000 m
```

```
Data Totals:
Number of Records:          5651
Bathymetry Data (121 beams):
  Number of Beams:          683771
  Number of Good Beams:     669894      97.97%
  Number of Zero Beams:     8485        1.24%
```

```

Number of Flagged Beams:      5392      0.79%
Amplitude Data (0 beams):
Number of Beams:              0
Number of Good Beams:        0      0.00%
Number of Zero Beams:        0      0.00%
Number of Flagged Beams:     0      0.00%
Sidescan Data (0 pixels):
Number of Pixels:            0
Number of Good Pixels:       0      0.00%
Number of Zero Pixels:       0      0.00%
Number of Flagged Pixels:    0      0.00%

```

Navigation Totals:

```

Total Time:      18.4311 hours
Total Track Length: 383.1487 km
Average Speed:   20.7881 km/hr (11.2368 knots)

```

Start of Data:

```

Time: 06 07 1996 23:53:28.500000 JD159
Lon: -174.1924      Lat: -14.3063      Depth: 5188.0000 meters
Speed: 2.0480 km/hr ( 1.1070 knots) Heading: 129.6000 degrees
Sonar Depth: 0.0000 m Sonar Altitude: 5188.0000 m

```

End of Data:

```

Time: 06 08 1996 18:19:20.500000 JD160
Lon: -170.6810      Lat: -14.3296      Depth: 0.0000 meters
Speed: 1.4319 km/hr ( 0.7740 knots) Heading: 11.1000 degrees
Sonar Depth: 0.0000 m Sonar Altitude: 85.0000 m

```

Limits:

```

Minimum Longitude: -174.2444      Maximum Longitude: -170.6617
Minimum Latitude:  -14.4954      Maximum Latitude:  -14.2407
Minimum Sonar Depth: 0.0000      Maximum Sonar Depth: 0.0000
Minimum Altitude:  85.0000      Maximum Altitude:  5310.0000
Minimum Depth:     83.0000      Maximum Depth:     6087.0000

```

9.3 The MB-System "mbgrid" Command

The "mbgrid" command in MB-System is used to compile raw multibeam files into a single GMT grid. This command can be altered via switches to accommodate characteristics of the raw multibeam files and produce customized outputs. The following is the command used in this study to produce the compiled grid, adapted from the work of Lundblad (2004).

```

mbgrid -Icompilation_datalist.txt -E200/200/m -R189/192.5/-15.5/-13.2
-Ocompilation_200 -L1 -C1 -X0.1 -A1 -N -V

```

Each switch (i.e. -I, -L, -X, etc.) controls an aspect of the output grid. **Table 4** lists each switch and its effect.

Table 4: MB-System “mbgrid” command switches and descriptions.

Switch	Description
-I	Defines the datalist filename and its location. In this instance, the “mbgrid” command is being executed from the same directory in which the datalist file is located.
-E	Defines the spatial resolution of the output grid. Each pixel represents a square 200 m by 200 m in area.
-R	Defines the rectangular bounds of the output grid. All of the raw multibeam files used in this study use a 0° to 360° longitudinal coordinate system.
-O	Defines the output filename. The file extension “.grd” is automatically appended.
-L	Defined as “1” if the longitudinal range is from 0° to 360°. This is common with Scripps Institution of Oceanography data.
-C	Defines the number of grid cells appended to edge of grid using a spline algorithm. This is used for edge-smoothing and should be experimented with to achieve the best effect.
-X	Defines the factor of grid extension to accommodate for spline interpolation. Again, experimentation is suggested.
-A	Defines the mode of depth enumeration, with “1” if depth values are positive and “2” if depth values are negative.
-N	Gives empty grid cells a value of “NaN” rather than 99999.9.
-V	Shows printout on screen of the “mbgrid” command executing.

This is not an exhaustive list of switches and additional definitions may be required depending on the nature of the raw multibeam files. A complete list of switches is available on the MB-System website (<http://www.ldeo.columbia.edu/res/pi/MB-System/>). Execution of the “mbgrid” command produces a list of the raw multibeam files and the number of data points read from each file. It is important to review screen output of the command to diagnose any problems with specific files or other failure of the command to execute properly.

9.4 Visualization Options

The product grid of the “mbgrid” command can be viewed in several software environments, of which two were employed in this study. Mirone (Luis 2007) is an open-source program based on the MATLAB framework, though MATLAB is not required to install an operational version of the program. Mirone is an excellent program for quickly viewing GMT grids and producing

simple plan-view visualizations that include hillshading, contouring, and customized color ramping. Without the need for color ramping, **Foldout Map 2** was produced using Mirone to create and capture grayscale images of individual multibeam swaths, which were later colorized using Adobe Photoshop.

All other plan-view and oblique-view visualizations were produced using the commercial software package Fledermaus. Fledermaus is a high-end software package capable of generating appealing 3D graphics using advanced smoothing and hillshading algorithms. The data management component of the larger Fledermaus suite, D-Magic, is used for importing the compilation grid and producing plan-view visualizations (**Foldout Maps 1; 3; 4**). D-Magic is also used to compile a Fledermaus object (i.e. .sd file) from the geographic reference, depth value, and shade rendering files created during the importing process. The compiled object is then loaded to the classic Fledermaus console where oblique-view visualizations are produced (**Figure 26**).

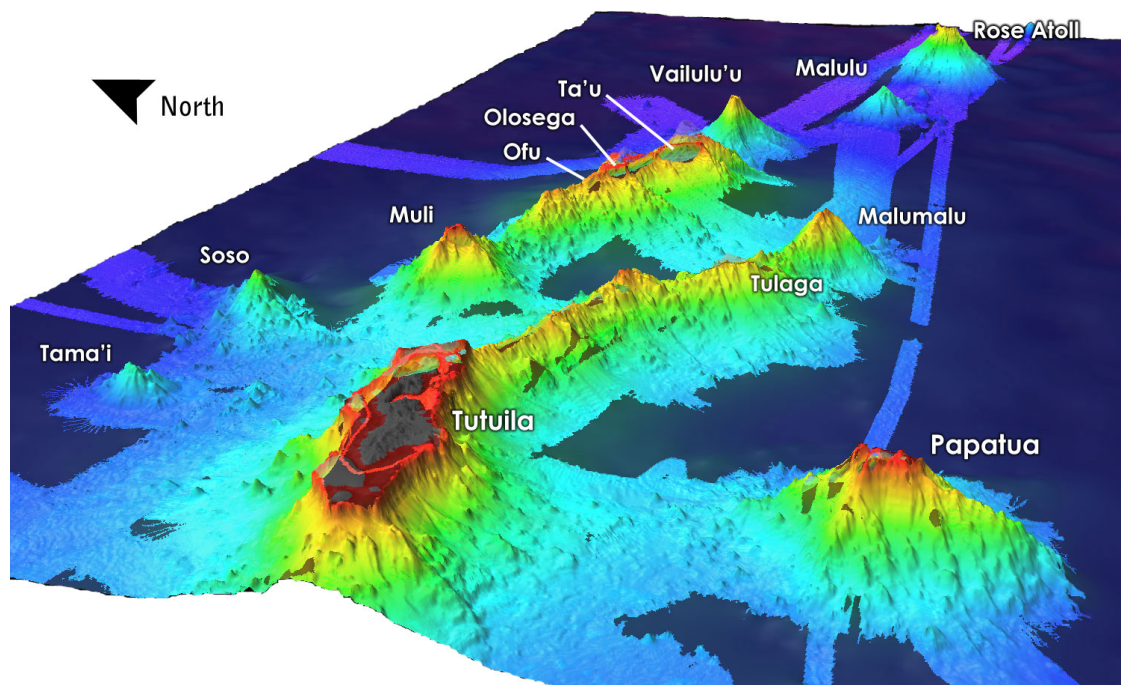


Figure 26: Oblique view of the ESVP. Scale varies at this perspective. Tutuila is approximately 160 miles from Rose Atoll. Vertical exaggeration of 3x.

10. Appendix B: Seamount Shape Statistics Expanded

10.1 Slope Surface and Profiles

The identification of small seamounts suitable for distribution analysis is contingent on the creation of a slope surface for the compilation grid (**Foldout Map 3**). In addition to data conversion and plan-view visualization, the Fledermaus component, D-Magic, is capable of some analytical functions. A scalar slope surface is created using the Compute Slope function located in the D-Magic Tools menu. A color map accenting slopes greater than ~10% is then applied to the resulting surface to aid in seamount identification. An additional analytical function of D-Magic is the profiling tool, accessed through “Analysis” in the View menu. After identification of candidate seamounts from the slope surface, shape parameters are estimated visually using the profiling tool (**Figure 15**), which calculates values for slope and length on the fly.

10.2 Secondary Shape Statistic Equations

- (1) Basal area (m²) = $\pi * (\text{basal major axis} / 2) * (\text{basal minor axis} / 2)$
- (2) Summit area (m²) = $\pi * (\text{summit major axis} / 2) * (\text{summit minor axis} / 2)$
- (3) Average height (m) = $(\text{major axis height} + \text{minor axis height}) / 2$
- (4) Average slope (%) = $(\text{major axis slope left} + \text{major axis slope right} + \text{minor axis slope} + \text{minor axis slope right}) / 4$
- (5) Flatness = $(\text{summit area} / \text{basal area})$
- (6) Basal elongation = $(\text{basal major axis} / \text{basal minor axis})$
- (7) Volume (m³) = $1/3 * \text{average height} * [\text{summit area} + \text{basal area} + \sqrt{(\text{summit area} * \text{basal area})}]$

10.3 Shape Statistics by Seamount

Tables 5 and **6** list all shape parameters measured and shape statistics calculated for 51 identified seamounts in the ESVP.

Table 5: Complete shape parameters and statistics (first portion). *ID* – seamount identifier; *Lat* – latitude (decimal degrees); *Long* – longitude (decimal degrees); B_{ma} – basal major axis (m); B_{mi} – basal minor axis (m); B_a – basal area (km²); S_{ma} – summit major axis (m); S_{mi} – summit minor axis (m); S_a – summit area (km²); H_{ma} – height major axis (m); H_{mi} – height minor axis (m); H_{av} – average height (m).

ID	Lat	Long	B_{ma}	B_{mi}	B_a	S_{ma}	S_{mi}	S_a	H_{ma}	H_{mi}	H_{av}
ESVP-01	-15.14844	-170.89170	2010	1370	2.1628	350	300	0.0825	110	100	105
ESVP-02	-15.09629	-170.93991	2600	1780	3.6348	450	270	0.0954	100	120	110
ESVP-03	-14.45616	-169.81821	2140	1580	2.6556	240	70	0.0132	120	120	120
ESVP-04	-13.66100	-170.49835	1530	1420	1.7064	240	140	0.0264	150	120	135
ESVP-05	-13.85079	-168.63422	2150	1770	2.9888	150	130	0.0153	140	130	135
ESVP-06	-13.91595	-168.76782	2060	1790	2.8961	210	80	0.0132	130	160	145
ESVP-07	-14.59628	-168.51622	1920	1650	2.4881	170	130	0.0174	150	150	150
ESVP-08	-14.72782	-170.72606	2380	1820	3.4020	250	250	0.0491	150	170	160
ESVP-09	-15.12972	-170.96895	2310	1920	3.4834	290	250	0.0569	170	160	165
ESVP-10	-14.36949	-168.74989	2100	2090	3.4471	170	170	0.0227	190	200	195
ESVP-11	-14.25079	-170.24950	1930	1800	2.7285	70	80	0.0044	210	220	215
ESVP-12	-14.53771	-170.69055	2250	2130	3.7640	220	190	0.0328	220	210	215
ESVP-13	-14.42799	-169.75640	6340	4030	20.0671	2350	1110	2.0487	210	230	220
ESVP-14	-13.91661	-170.38342	2920	2460	5.6417	210	140	0.0231	260	200	230
ESVP-15	-14.40115	-169.78530	2890	2440	5.5383	200	320	0.0503	280	190	235
ESVP-16	-14.65214	-168.79845	2480	2110	4.1098	60	130	0.0061	270	260	265
ESVP-17	-14.56384	-168.56096	2230	1840	3.2226	280	100	0.0220	270	270	270
ESVP-18	-13.99554	-170.77884	3690	1760	5.1007	420	260	0.0858	280	280	280
ESVP-19	-14.01831	-168.91832	3990	1900	5.9541	660	80	0.0415	290	270	280
ESVP-20	-14.37106	-169.79172	2720	2400	5.1271	240	120	0.0226	310	270	290
ESVP-21	-14.55249	-168.48030	4820	3080	11.6597	200	220	0.0346	310	270	290
ESVP-22	-14.77354	-170.48975	2810	1870	4.1270	920	290	0.2095	310	280	295
ESVP-23	-13.94850	-168.85074	2500	2310	4.5357	150	170	0.0200	310	290	300
ESVP-24	-14.59793	-170.63538	3240	2150	5.4711	220	260	0.0449	280	320	300
ESVP-25	-13.89409	-170.61714	2580	1990	4.0324	260	280	0.0572	340	270	305
ESVP-26	-14.37178	-168.77182	3100	2970	7.2312	180	110	0.0156	290	320	305
ESVP-27	-14.18954	-168.78363	2290	2010	3.6151	180	180	0.0254	330	290	310
ESVP-28	-14.63187	-170.66154	3160	2280	5.6586	1070	220	0.1849	270	350	310
ESVP-29	-14.74146	-170.75952	3150	2220	5.4923	300	300	0.0707	300	320	310
ESVP-30	-14.16448	-168.80365	2810	2390	5.2747	220	330	0.0570	340	290	315
ESVP-31	-14.51766	-168.49440	2520	2370	4.6907	290	320	0.0729	350	280	315
ESVP-32	-14.41868	-169.80067	2410	2350	4.4481	240	60	0.0113	330	320	325
ESVP-33	-14.45928	-168.47646	3720	2260	6.6030	180	360	0.0509	320	330	325
ESVP-34	-13.62784	-170.28395	3200	2270	5.7051	330	140	0.0363	410	280	345
ESVP-35	-13.84260	-170.48700	2860	2560	5.7504	320	240	0.0603	400	290	345
ESVP-36	-13.68659	-170.47915	2170	2160	3.6813	370	250	0.0726	330	370	350
ESVP-37	-14.55968	-169.62099	2690	2610	5.5142	200	280	0.0440	360	340	350
ESVP-38	-13.99497	-170.38104	3450	3120	8.4540	140	190	0.0209	410	340	375
ESVP-39	-14.43339	-169.87112	3170	2400	5.9753	990	150	0.1166	390	370	380
ESVP-40	-14.50618	-168.52243	3530	2890	8.0124	690	210	0.1138	410	370	390
ESVP-41	-14.05291	-170.80361	3000	1900	4.4768	310	210	0.0511	400	400	400
ESVP-42	-14.02459	-170.45889	4120	2980	9.6428	370	250	0.0726	420	460	440

Table 5: Cont'd.

ID	Lat	Long	B _{ma}	B _{mi}	B _a	S _{ma}	S _{mi}	S _a	H _{ma}	H _{mi}	H _{av}
ESVP-43	-14.08271	-170.19569	3050	2930	7.0187	220	150	0.0259	470	450	460
ESVP-44	-13.55448	-170.12479	3200	2970	7.4644	240	230	0.0434	480	510	495
ESVP-45	-13.71510	-170.27754	4120	2970	9.6104	230	330	0.0596	600	460	530
ESVP-46	-14.14285	-170.80046	3350	2870	7.5512	300	350	0.0825	530	530	530
ESVP-47	-13.87163	-168.68845	4650	3390	12.3806	230	120	0.0217	580	510	545
ESVP-48	-14.30320	-169.21414	4290	3050	10.2765	280	190	0.0418	670	520	595
ESVP-49	-14.66922	-169.61685	5330	3890	16.2842	290	260	0.0592	710	540	625
ESVP-50	-14.65959	-170.03477	4140	4070	13.2338	100	310	0.0243	640	630	635
ESVP-51	-14.53092	-168.41925	6930	6710	36.5213	210	320	0.0528	850	850	850

Table 6: Complete shape parameters and statistics (second portion). *ID* – seamount identifier; *SL_{mal}* – slope major axis left (%); *SL_{mar}* – slope major axis right (%); *SL_{mil}* – slope minor axis left (%); *SL_{mir}* – slope minor axis right (%); *SL_{av}* – average slope (%); *BM_{az}* – azimuth of basal major axis (0 – 180 degrees); *B_d* – basal depth (mbsl); *S_d* – summit depth (mbsl); *F* – flatness; *B_{el}* – basal elongation; *V* – volume (km³).

ID	SL _{mal}	SL _{mar}	SL _{mil}	SL _{mir}	SL _{av}	BM _{az}	B _d	S _d	F	B _{el}	V
ESVP-01	5.4	6.4	6.4	8.8	6.8	60	-4505	-4400	0.0381	1.47	0.09
ESVP-02	4.6	4.0	6.8	8.2	5.9	45	-4460	-4350	0.0263	1.46	0.16
ESVP-03	8.1	6.8	14.8	10.4	10.0	10	-3370	-3250	0.0050	1.35	0.11
ESVP-04	10.6	12.9	7.1	9.1	9.9	5	-4555	-4420	0.0155	1.08	0.09
ESVP-05	7.7	7.3	7.7	11.0	8.4	160	-5205	-5070	0.0051	1.21	0.14
ESVP-06	8.4	11.5	7.7	8.3	9.0	70	-5165	-5020	0.0046	1.15	0.15
ESVP-07	10.9	10.1	9.5	8.2	9.7	5	-5030	-4880	0.0070	1.16	0.14
ESVP-08	11.6	6.6	13.6	11.6	10.9	35	-3730	-3570	0.0144	1.31	0.21
ESVP-09	7.6	8.5	8.5	9.0	8.4	85	-4485	-4320	0.0163	1.20	0.22
ESVP-10	9.9	11.7	12.2	9.8	10.9	20	-4935	-4740	0.0066	1.00	0.24
ESVP-11	13.4	10.7	15.3	12.5	13.0	75	-2995	-2780	0.0016	1.07	0.20
ESVP-12	13.2	10.1	11.3	11.6	11.6	5	-3275	-3060	0.0087	1.06	0.30
ESVP-13	4.4	7.2	7.9	8.0	6.9	70	-3360	-3140	0.1021	1.57	2.09
ESVP-14	12.2	11.6	8.0	8.8	10.2	85	-3970	-3740	0.0041	1.19	0.46
ESVP-15	11.9	8.0	12.1	8.0	10.0	120	-3385	-3150	0.0091	1.18	0.48
ESVP-16	10.8	12.6	14.9	13.6	13.0	115	-5005	-4740	0.0015	1.18	0.38
ESVP-17	16.5	11.9	15.3	18.8	15.6	165	-4960	-4690	0.0068	1.21	0.32
ESVP-18	7.6	9.8	17.2	14.4	12.3	5	-3800	-3520	0.0168	2.10	0.55
ESVP-19	8.2	11.8	15.8	13.6	12.4	0	-4940	-4660	0.0070	2.10	0.61
ESVP-20	14.4	11.9	14.1	11.4	13.0	0	-3290	-3000	0.0044	1.13	0.53
ESVP-21	5.6	9.6	13.2	8.1	9.1	80	-4990	-4700	0.0030	1.56	1.19
ESVP-22	15.7	17.0	16.7	19.1	17.1	165	-4085	-3790	0.0508	1.50	0.52
ESVP-23	14.2	15.8	12.9	16.7	14.9	155	-5100	-4800	0.0044	1.08	0.49
ESVP-24	10.9	9.2	18.4	15.9	13.6	170	-3650	-3350	0.0082	1.51	0.60
ESVP-25	17.8	9.5	15.2	13.8	14.1	135	-4125	-3820	0.0142	1.30	0.46
ESVP-26	12.1	10.6	11.9	9.0	10.9	25	-4965	-4660	0.0022	1.04	0.77

Table 6: Cont'd.

ID	SL _{mal}	SL _{mar}	SL _{mil}	SL _{mir}	SL _{av}	BM _{az}	B _d	S _d	F	B _{el}	V
ESVP-27	17.0	16.8	16.0	16.3	16.5	5	-5050	-4740	0.0070	1.14	0.41
ESVP-28	11.3	16.2	19.3	17.9	16.2	20	-3580	-3270	0.0327	1.39	0.71
ESVP-29	8.7	12.4	15.1	11.4	11.9	15	-3810	-3500	0.0129	1.42	0.64
ESVP-30	12.1	13.7	13.7	15.1	13.7	130	-4935	-4620	0.0108	1.18	0.62
ESVP-31	15.2	13.9	16.7	12.5	14.6	0	-4975	-4660	0.0155	1.06	0.56
ESVP-32	19.1	15.9	16.9	16.2	17.0	5	-3395	-3070	0.0025	1.03	0.51
ESVP-33	11.1	8.9	15.7	17.8	13.4	85	-4935	-4610	0.0077	1.65	0.78
ESVP-34	14.5	12.1	13.2	15.6	13.9	160	-4595	-4250	0.0064	1.41	0.71
ESVP-35	15.9	15.4	11.0	16.0	14.6	110	-4195	-3850	0.0105	1.12	0.74
ESVP-36	16.3	19.8	18.3	17.8	18.1	85	-4530	-4180	0.0197	1.00	0.50
ESVP-37	18.3	14.1	18.5	12.2	15.8	40	-3940	-3590	0.0080	1.03	0.71
ESVP-38	12.0	14.0	13.8	11.8	12.9	35	-3755	-3380	0.0025	1.11	1.11
ESVP-39	19.9	18.3	16.1	19.0	18.3	155	-3390	-3010	0.0195	1.32	0.88
ESVP-40	16.1	12.5	11.9	15.6	14.0	15	-4980	-4590	0.0142	1.22	1.18
ESVP-41	16.5	17.7	23.5	22.7	20.1	150	-3500	-3100	0.0114	1.58	0.67
ESVP-42	7.4	18.3	14.5	17.8	14.5	20	-3840	-3400	0.0075	1.38	1.55
ESVP-43	17.3	17.7	17.8	15.0	17.0	20	-2640	-2180	0.0037	1.04	1.15
ESVP-44	18.4	17.4	18.3	17.4	17.9	10	-4835	-4340	0.0058	1.08	1.33
ESVP-45	18.7	13.2	20.6	17.9	17.6	80	-4120	-3590	0.0062	1.39	1.84
ESVP-46	19.0	18.3	23.5	17.9	19.7	90	-2920	-2390	0.0109	1.17	1.49
ESVP-47	12.4	13.6	16.4	17.6	15.0	115	-5175	-4630	0.0018	1.37	2.35
ESVP-48	20.4	13.4	18.6	19.7	18.0	25	-3915	-3320	0.0041	1.41	2.18
ESVP-49	15.3	14.3	16.4	17.3	15.8	50	-4125	-3500	0.0036	1.37	3.61
ESVP-50	18.6	14.8	20.4	14.3	17.0	10	-3175	-2540	0.0018	1.02	2.93
ESVP-51	13.6	14.8	14.7	13.1	14.1	45	-4950	-4100	0.0014	1.03	10.76

11. Appendix C: Seamount Distribution Analysis Expanded

11.1 Calculating Area

In order to calculate the total area of the multibeam compilation, a projected coordinate system must be applied to the GMT grid. The following steps are taken to achieve this:

- The compilation grid is exported from Fledermaus D-Magic to an ArcGIS 9.2 compatible ASCII grid.
- With the ArcToolbox in either ArcCatalog or ArcMap, the ASCII-to-Raster tool (Conversion Tools → To Raster) is used to convert the ASCII grid to an Arc grid.
- Again, with the ArcToolbox, the Arc grid is converted from a raster dataset to a vector dataset (i.e. feature class) using the Raster-to-Polygon tool (Conversion Tools → From Raster).

- Each depth value is represented in the new feature class. The area must be calculated for a single, homogenous feature class that represents the perimeter of compilation grid. Therefore, the feature class must be generalized using the Dissolve tool (Data Management Tools → Generalization).
- The perimeter feature class currently has no defined projection, though its units are based on a lat/long coordinate system inherited from the GMT grid. The world geographic coordinate system WGS 1984 is defined using the Define Projection tool (Data Management Tools → Projections and Transformations).
- A geographic coordinate system has no inherent linear unit from which to calculate area. Using the Project tool (Data Management → Projections and Transformations → Feature), the WGS 1984 is projected to the WGS 1984 UTM Zone 2S coordinate system, which is based on the linear meter.
- The feature class is now prepared for area calculation. While viewing its attribute table in ArcCatalog or ArcMap, use the table options to add a new field called “Area.” After starting an edit session using the Editor Toolbar in ArcMap, right-click on the column heading for the “Area” attribute and select the Field Calculator. Check the “Advanced” button and type the following code in the “Pre-Logic VBA Script Code” field

```
Dim dblArea as double
Dim pArea as IArea
Set pArea = [shape]
dblArea = pArea.area
```

and then dblArea in the “Area =” field. The area is displayed is in square meters. Conversion to square kilometers yields an area of 28,446 km².

The large seamounts omitted from the distribution analysis account for a significant proportion of the total area of the compilation grid. To more accurately estimate the distribution of small seamounts in the ESVP, the area of large seamounts must be subtracted out. To achieve this, the following steps are taken:

- A new polygon feature class is created in ArcCatalog using the same spatial reference as the perimeter feature class.
- Using the Editor Toolbar in ArcMap, the outline of each large seamount is sketched.
- After saving edits, the Union tool in the ArcToolbox (Analysis Tools → Overlay) is used to combine both the large seamount feature class and the compilation perimeter feature class.

- Using the Editor Toolbar, all coincident areas are selected and deleted from the union feature class.
- Employing the same procedure as used to calculate the total area, area is calculated for the edited union feature class. This yields an area of 21,158 km².

11.2 Calculating Characteristic Height

The first step toward defining seamount density using the exponential distribution model devised by Smith and Jordan (1988) is the calculation of a characteristic seamount height. In the exponential distribution model, characteristic height is \mathbf{B}^{-1} , the negative reciprocal of the slope of the line fitting $\ln(\mathbf{v}(\mathbf{H}))$. $\mathbf{v}(\mathbf{H})$ is described as the number of seamounts per unit area having a height greater than or equal to \mathbf{H} . $\mathbf{v}(\mathbf{H})$ is calculated for all 48 seamounts in the dataset. For instance, there are 48 seamounts with equal or greater height than the smallest seamount (105 m). Applying the area calculated in **Section 11.1**, we find that there are 48 seamounts per 21,158 km², or approximately 2.27 seamounts per 1,000 km². This same calculation is carried out successively for each seamount, though as seamount height increases, seamount density decreases (**Table 7**).

Table 7: Calculation of $\mathbf{v}(\mathbf{H})$ per 1,000 km² for seamount dataset.

H (m)	$\mathbf{v}(\mathbf{H})$ per 1,000 km ²	H (m)	$\mathbf{v}(\mathbf{H})$ per 1,000 km ²	H (m)	$\mathbf{v}(\mathbf{H})$ per 1,000 km ²
105	$(48000/21158) = 2.27$	270	$(32000/21158) = 1.51$	325	$(16000/21158) = 0.76$
110	$(47000/21158) = 2.22$	280	$(30000/21158) = 1.42$	345	$(14000/21158) = 0.66$
120	$(46000/21158) = 2.17$	280	$(30000/21158) = 1.42$	345	$(14000/21158) = 0.66$
135	$(44000/21158) = 2.08$	290	$(28000/21158) = 1.32$	350	$(12000/21158) = 0.57$
135	$(44000/21158) = 2.08$	290	$(28000/21158) = 1.32$	350	$(12000/21158) = 0.57$
145	$(43000/21158) = 2.03$	295	$(27000/21158) = 1.28$	375	$(11000/21158) = 0.52$
150	$(42000/21158) = 1.99$	300	$(25000/21158) = 1.18$	380	$(10000/21158) = 0.47$
160	$(41000/21158) = 1.94$	300	$(25000/21158) = 1.18$	390	$(9000/21158) = 0.43$
165	$(40000/21158) = 1.89$	305	$(23000/21158) = 1.09$	400	$(8000/21158) = 0.38$
195	$(39000/21158) = 1.84$	305	$(23000/21158) = 1.09$	440	$(7000/21158) = 0.33$
215	$(37000/21158) = 1.75$	310	$(20000/21158) = 0.95$	460	$(6000/21158) = 0.28$
215	$(37000/21158) = 1.75$	310	$(20000/21158) = 0.95$	495	$(5000/21158) = 0.24$
220	$(36000/21158) = 1.70$	310	$(20000/21158) = 0.95$	530	$(3000/21158) = 0.14$
230	$(35000/21158) = 1.65$	315	$(18000/21158) = 0.85$	530	$(3000/21158) = 0.14$
235	$(34000/21158) = 1.61$	315	$(18000/21158) = 0.85$	545	$(2000/21158) = 0.09$
265	$(33000/21158) = 1.56$	325	$(16000/21158) = 0.76$	595	$(1000/21158) = 0.05$

Next, the natural log of $v(H)$ is calculated for each seamount (**Table 8**).

The slope of the line fitting $\ln(v(H))$ plotted against H is then calculated.

$$\beta = \Delta \ln(v(H)) / \Delta H$$

$$\beta = -0.0072$$

Finally, the reciprocal of the slope is calculated to define the characteristic seamount height.

$$\beta^{-1} = 138.7705 \text{ m}$$

Table 8: Calculate of $\ln(v(H))$ for seamount dataset.

$\ln(v(H))$	$\ln(v(H))$	$\ln(v(H))$
$LN(2.27) = 0.8192$	$LN(1.51) = 0.4137$	$LN(0.76) = -0.2794$
$LN(2.22) = 0.7981$	$LN(1.42) = 0.3492$	$LN(0.66) = -0.4130$
$LN(2.17) = 0.7766$	$LN(1.42) = 0.3492$	$LN(0.66) = -0.4130$
$LN(2.08) = 0.7322$	$LN(1.32) = 0.2802$	$LN(0.57) = -0.5671$
$LN(2.08) = 0.7322$	$LN(1.32) = 0.2802$	$LN(0.57) = -0.5671$
$LN(2.03) = 0.7092$	$LN(1.28) = 0.2438$	$LN(0.52) = -0.6541$
$LN(1.99) = 0.6857$	$LN(1.18) = 0.1669$	$LN(0.47) = -0.7494$
$LN(1.94) = 0.6616$	$LN(1.18) = 0.1669$	$LN(0.43) = -0.8548$
$LN(1.89) = 0.6369$	$LN(1.09) = 0.0835$	$LN(0.38) = -0.9726$
$LN(1.84) = 0.6115$	$LN(1.09) = 0.0835$	$LN(0.33) = -1.1061$
$LN(1.75) = 0.5589$	$LN(0.95) = -0.0563$	$LN(0.28) = -1.2603$
$LN(1.75) = 0.5589$	$LN(0.95) = -0.0563$	$LN(0.24) = -1.4426$
$LN(1.70) = 0.5315$	$LN(0.95) = -0.0563$	$LN(0.14) = -1.9534$
$LN(1.65) = 0.5033$	$LN(0.85) = -0.1616$	$LN(0.14) = -1.9534$
$LN(1.61) = 0.4743$	$LN(0.85) = -0.1616$	$LN(0.09) = -2.3589$
$LN(1.56) = 0.4445$	$LN(0.76) = -0.2794$	$LN(0.05) = -3.0520$

11.3 Calculating Seamount Distribution

Seamount density per 1,000 km², or v_0 , is represented by the intercept of the characteristic height along the exponential regression fit to the relationship between the independent variable H to the dependent variable $v(H)$. Using the Exponential Trendline function in Microsoft Excel, an exponential regression equation is formulated.

$$v_o = 7.6153e^{-0.0072x}$$

The exponential regression equation is then solved for using the characteristic seamount height.

$$v_o = 7.6153(2.7182818)^{-0.0072(138.7705)}$$

$$v_o = 2.8039 \text{ seamounts per } 1,000 \text{ km}^2$$

Finally, a confidence interval is calculated for the exponential regression fit at the 95% confidence level.

$$\pm \alpha * (\sigma/\sqrt{n})$$

$$\pm 1.96 * (0.6633/\sqrt{48})$$

$$\pm 0.1877$$